This thesis is submitted for the degree of
MSc by Research in Environmental Science

The dispersion and atmospheric concentrations of co-PDC ash clouds

submitted by

Marie Hagenbourger

Supervised by *Dr Thomas J. Jones*

Lancaster Environment Centre

Lancaster University

October, 2025

funded by:

Deutscher Akademischer Austauschdienst
German Academic Exchange Service

The dispersion and atmospheric concentrations of co-PDC ash clouds

Marie Hagenbourger
Lancaster Environment Centre, Lancaster University

This thesis is submitted for the degree of *MSc by Research* in Environmental Science.

October, 2025

Abstract

Pyroclastic density currents (PDCs) are gravity currents that frequently form during explosive volcanic eruptions. These ground-hugging density currents consist of high-temperature mixtures of pyroclasts (e.g., ash, pumice), lithics, and gas. These flows have the potential to generate co-PDC plumes, which detach from the underlying PDC as they buoyantly rise into the atmosphere. These co-PDC plumes, composed of fine-grained ash particles and hot gas, can reach heights of tens of kilometres, potentially dispersing large volumes of ash over continental-scale areas, impacting the environment, and posing a risk to aviation. Owing to their formation mechanism, co-PDCs have unique characteristics, such as a fine particle size (e.g., $< 90\,\mu\mathrm{m}$) and a high-aspect ratio, irregular-shaped, source geometry. Here, I consider how the release of ash into the atmosphere from a co-PDC plume may differ from that of a typical Plinian eruption column. I also assess the implications of any differences for operational modelling of the resulting ash cloud. I use the atmospheric dispersion model, NAME, which is used by the London Volcanic Ash Advisory Centre and perform a sensitivity analysis to determine which co-PDC source parameters are important for modelling the associated ash clouds. I find that variations in the source geometry, i.e., the total area and aspect ratio, show only a minor impact on the modelled ash cloud location and total mass in the atmosphere. However, different plume heights and associated mass eruption rates show a significant impact on the area, location, and concentration of the predicted downwind ash cloud. The newly introduced concentration thresholds for quantitative volcanic ash forecasts (QVA) are also considered within this study. When applying these thresholds, most clouds are very high-concentrated, often above $10\,\mathrm{mg\,m^{-3}}$.

Contents

List of Figures

List of Tables

Acknowledgements

Thank you to my amazing supervisor, Thomas Jones! I always felt welcomed, asking for another time to rediscuss the project, counting on your support and your time and mentorship! I highly value your aim and faith to unlock potential and guide me from a non-volcanologist into someone passionate about volcanology, atmospheric science and research! Also, thank you to my wonderful UK Met Office collaborator and co-supervisor, Frankie Beckett. Both inspired me with ideas, shared knowledge, time and many hours of discussions and meetings and introduced me into the conference world in Geneva. Thank you, Frankie, for welcoming me at the UK Met Office and within your V&C-group, linking me up for supportive and useful discussions within the Met Office and for inviting, joining and supporting me at the 'HotStuff' talk in Bristol. Additionally, without your laptop, the whole presentation would just not have been possible.

I would like to acknowledge Sam Engwell as a British Geological Survey collaborator on this thesis. Providing expert knowledge on co-PDCs and helping with literature insights and explanations shaped this piece of research on the current co-PDC understanding. I want to thank Nicola Stebbing for providing useful Python code for the data analysis and Charlie Bates for NAME support and for spending time and many ice creams with me at IAVCEI. Thanks to Oliver Wild for advising me on weather patterns and atmospheric questions, and Matthew C. Hort for helping with NAME-related grid information, supporting ideas and conversations.

I wish to acknowledge funding support by the 'Stipendien für ein Masterstudium im Ausland' fellowship of the German Academic Exchange Service (DAAD), which made this research and stay in Lancaster reachable and achievable.

A huge thank you goes to the volcanology group in Lancaster for their time, feedback on presentations and writing (thank you, Natalia and Sara), non-research-related conversations, laughter, hikes and sweets supply (especially thanks, Pier, Jodie and Aidan!).

Thank you to my friends and family for supporting me on my journey, showing care, believing in me and supporting me to go abroad and picking up my phone calls. I owe special thanks to Arne, who taught me some Python skills, helped me many times to fix my laptop when IT was unavailable and was able to relate to my thoughts, concerns and issues on conducting research and writing my thesis and first paper(s).

I would like to thank you both examiners, Mike James and Larry Mastin, for their time, thoughtful ideas and questions, and the very nice discussion during the viva.

Declaration

I declare that, other where the contribution of others is specified, the work presented in this thesis is, to the best of my knowledge and belief, original and my own work. It has not been submitted, in whole or in part, for any other degree or professional qualification at this, or any other university.

This thesis counts $18\,894$ words in length. Excluded from the word count are title page, abstract, contents, declarations, citations, appendices and bibliography.

Name: **Marie Hagenbourger**
Date: **20th October, 2025**

Multi-author declaration

Please find the list of publications and their information regarding contributions to each publication. My contribution and those of the other authors to this work have been explicitly indicated below.

Chapter 2

Modelling the transport and dispersion of volcanic co-PDC ash clouds using NAME: an evaluation of source geometry and mass eruption rate
Marie Hagenbourger, Frances M. Beckett, Thomas J. Jones, Samantha L. Engwell
Submitted to and currently under review for *Journal of Geophysical Research: Atmospheres*

The ideas for this work originated from an EPSRC-funded position (February 2024 – September 2024) that I was employed for by Thomas Jones. The initial NAME training and NAME licence setup were not part of this Master's by Research. However, the model runs, adjustments, all the data analysis and writing were conducted after October 2024 and are a part of this Master's by Research project.

MH designed the study with assistance from FMB, TJJ and SLE. SLE also advised on co-PDC-related questions. MH conducted the NAME runs and analysed the data with assistance from TJJ and FMB. MH produced all tables and figures and wrote the initial manuscript that later included revisions and edits by all co-authors.

Chapter 3

The ash concentration of co-PDC clouds
Marie Hagenbourger, Thomas J. Jones, Frances M. Beckett, Samantha L. Engwell
An edited version of this chapter is currently in preparation for submission to *Communications Earth & Environment*.

MH designed the study with assistance from TJJ and FMB. MH conducted the NAME run and data analysis with assistance from TJJ and FMB. SLE advised on co-PDC parameters and aviation-related topics. MH produced all tables and figures and wrote the initial manuscript that later included revisions and edits by all co-authors.

The co-authors of these publications/manuscripts have signed below to confirm this.

Yours sincerely,

Marie Hagenbourger

Co-authors:

Name: Dr. Thomas J. Jones
Signature:

Name: Dr. Frances M. Beckett
Signature:

Name: Dr. Samantha L. Engwell
Signature:

1. Introduction

Explosive volcanic eruptions can generate pyroclastic density currents (PDCs). This commonly occurs by the collapse of an eruption column (R. J. Brown & Andrews, 2015; Burgisser et al., 2024; Dellino et al., 2021; Druitt, 1998; Dufek et al., 2015; Giordano & Cas, 2021; T. J. Jones et al., 2023; Lube et al., 2020) or by the collapse of a lava dome (Bonadonna, Mayberry, et al., 2002; Calder et al., 1997; Charbonnier & Gertisser, 2008; Michol et al., 2008; Sigurdsson & Carey, 1989; Sulpizio et al., 2010; Ui et al., 1999). These ground-hugging gravity currents consist of a multiphase mixture of hot gas and particles, e.g., volcanic ash, fragments, and pumice. Due to air entrainment and a subsequent buoyancy reversal within the upper part of a PDC, a co-PDC can form by buoyant lift-off, also described as a co-ignimbrite or phoenix cloud (Andrews & Manga, 2011, 2012; Bursik & Woods, 1996; Engwell et al., 2016; T. J. Jones et al., 2024; Pistolesi et al., 2025; Rosi et al., 2006; Sigurdsson & Carey, 1989; Sparks et al., 1997; Woods & Wohletz, 1991). Hence, co-PDCs comprise hot gas and fine particles – only the small and light particles from within the PDC that are able to lift-off. The lift-off mixture rises until reaching a level of neutral buoyancy, where the particles spread laterally into the atmosphere.

Co-PDCs have unique physical properties, which are described as eruption source parameters (ESPs). The source geometry, is not a point source as in Plinian eruptions, for example, but rather irregularly shaped and elongated along one axis (Engwell & Eychenne, 2016). Furthermore, co-PDCs can lift off from parts, or from the entire length, of the PDC, and thus the source location can be at different distances from the vent (Andrews & Manga, 2011; Engwell & Eychenne, 2016; Sparks et al., 1986, 1997). The particle size is fine ($< 90\,\mu\mathrm{m}$) (Engwell & Eychenne, 2016; Sigurdsson & Carey, 1989) relative to typical volcanic ash clouds.

Co-PDCs have been studied using various models (Bursik & Woods, 1996; Calder et al., 1997; Engwell et al., 2016; Herzog & Graf, 2010; Neri et al., 2002, 2003; Sparks et al., 1997; Woods & Kienle, 1994; Woods & Wohletz, 1991) but have not yet been studied for operational volcanic ash advisory purposes. However, PDCs frequently form during explosive eruptions, and all PDCs have the potential to support co-PDC lift-off and thus supply ash into the atmosphere. Due to the small ash particle size, co-PDCs remain in the atmosphere for long durations, travel long distances, and disperse over large areas (Pardini et al., 2024; Saxby et al., 2018). They therefore potentially pose a hazard to aircraft not only close to the eruption but also downwind, and this highlights the need for operational studies to be conducted.

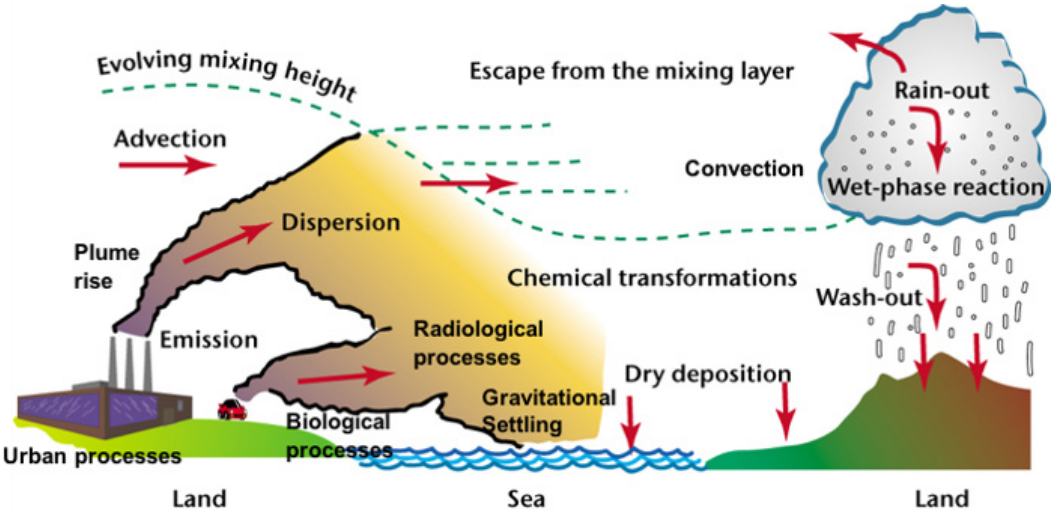

Figure 1.1: The relevant atmospheric processes governing the release, transport, and dispersion of particles simulated in the Numerical Atmospheric-dispersion Modelling Environment (NAME). Taken from UK Met Office NAME Training course, June 2024.

The UK Met Office's Numerical Atmospheric-dispersion Modelling Environment (NAME) was developed after the 1986 Chernobyl nuclear accident (A. Jones et al., 2007). It is used for air quality forecasts, emergency response and event impact assessments (e.g., volcanic eruptions, chemical accidents, wind-spread diseases). The model is initialised with information about the source, referred to as the ESPs, and models the spread of released modelled particles that are subject to the meteorological conditions. Insight into relevant atmospheric processes used within NAME is shown in Figure 1.1. They can be selected or added as specific schemes, e.g., buoyant plumes schemes (Devenish, 2013) and umbrella cloud scheme (Webster et al., 2020) in the Eulerian configuration. With particular importance here, in this thesis, NAME is operationally used by the London Volcanic Ash Advisory Centre (VAAC) to issue advisories for volcanic eruptions due to their impact on aviation. For implementing co-PDCs in NAME, I identified four different types of input variables. Specifically, these include: timing (i.e., date and the duration of the eruption defined by start and end times), particle characteristics (i.e., the description of the particles, size and shape, based on how they are found in natural deposits), source geometry (i.e., shape of the release volume and the associated height), source location (i.e., the position of the release within the meteorological model). The set of NAME model outputs are then generated for a specific time interval, computational domain size, and position. All these possible input parameters of NAME, which can be changed in the input file/source block, are shown in Figure 1.2. If the variable is boxed in Figure 1.2, these are systematically varied in this work; else, they are defined once and held constant. Variations in date and start time encompass different weather conditions. The purpose and formal definition of each parameter will be discussed in the following chapters.

This thesis aims to:

- Define the natural range of each co-PDC parameter for use in NAME

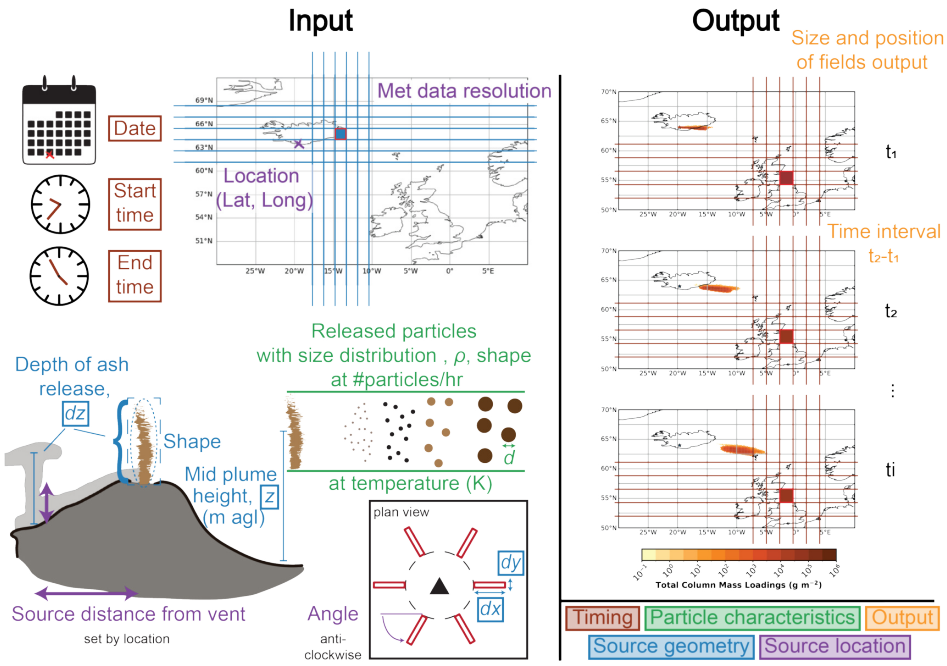

Figure 1.2: Overview of parameters within NAME for volcanic eruption modelling. Here, they are distinguished into four main input types: timing, particle characteristics, source geometry and source location, and the output parameters.

- Explore the sensitivity of NAME model outputs to the different co-PDC parameters
- Apply new insights into operational forecasting by applying ash concentration thresholds to assess the aviation hazard of co-PDC ash clouds

This thesis is written in the publication format and is structured in the following way: It consists of four chapters in total. This introductory chapter is followed by two data chapters prepared as journal manuscripts and finally a discussion and conclusion chapter. Throughout the data chapters, the pronouns 'we/our' are used instead of 'I/my' to recognise the co-authors' contributions.

Chapter 2 represents a manuscript with the title 'Modelling the transport and dispersion of volcanic co-PDC ash clouds using NAME: an evaluation of source geometry and mass eruption rate' as a sensitivity study on co-PDC eruption source parameters evaluated in a model environment on horizontal ash footprints and is currently under review at *Journal of Geophysical Research: Atmospheres*, co-authored by Frances M. Beckett, Thomas J. Jones, and Samantha L. Engwell. Based on PDC and co-PDC events documented in published literature, it provides an overview of the parameter range likely for co-PDC plumes. This work also demonstrates that the source area and the aspect ratio of the release area have a minor impact on the downwind ash transport and dispersion. It confirms the plume height and mass eruption rate as being one of the most important parameters for modelling co-PDC plumes.

Chapter 3 represents a manuscript with the title 'The ash concentration of co-PDC clouds', that is in preparation for *Nature Communications Earth & Environment*, co-authored by Thomas J. Jones,

Frances M. Beckett, and Samantha L. Engwell. This work studies the vertical ash concentration of the downwind-travelling cloud in different flight levels within the atmosphere. With knowledge on ash dispersion from Chapter 2, this chapter expands in the vertical dimension and considers the impacts for aviation with respect to current regulations.

Chapter 4 concludes this work with an integrated overview of the preceding individual chapters and summarises our key findings. I propose future work needed to fully understand the modelled co-PDC processes and observed behaviours, and possible wider applications to volcanology in general.

2. Modelling the transport and dispersion of volcanic co-PDC ash clouds using NAME: an evaluation of source geometry and mass eruption rate

2.1 Introduction

Pyroclastic density currents (PDCs) are ground-hugging gravity currents that can occur during an explosive volcanic eruption through eruption column collapse (R. J. Brown & Andrews, 2015; Dellino et al., 2021; Druitt, 1998; Dufek et al., 2015; Giordano & Cas, 2021; T. J. Jones et al., 2023; Lube et al., 2020) or from the collapse of lava dome or flow fronts (Bonadonna, Mayberry, et al., 2002; Calder et al., 1997; Charbonnier & Gertisser, 2008; Michol et al., 2008; Sigurdsson & Carey, 1989; Sulpizio et al., 2010; Ui et al., 1999). They are a multi-phase mixture composed of hot gas and solid particles (e.g., lithics, pumice, ash) that propagate downslope with flow paths that are largely controlled by topography (Andrews & Manga, 2011, 2012; R. J. Brown & Andrews, 2015; Druitt, 1998; Dufek et al., 2015; T. J. Jones et al., 2023; Lube et al., 2020). All PDCs have the potential to generate co-PDC plumes, also known as co-ignimbrites or phoenix clouds (Andrews & Manga, 2011; Bursik & Woods, 1996; Engwell & Eychenne, 2016; Rosi et al., 2006; Sigurdsson & Carey, 1989; Sparks et al., 1997). These secondary plumes are composed of fine-grained particles and gas, which detach from the underlying PDC current by air intrusion and rise vertically by buoyancy (Andrews & Manga, 2011, 2012; Engwell & Eychenne, 2016; T. J. Jones et al., 2023; Sparks et al., 1997). Within the PDC, particle sedimentation acts to lower the current density, particularly in its uppermost regions, and when below ambient atmospheric density, a plume can form (Andrews & Manga, 2012; Engwell et al., 2016; Woods & Kienle, 1994). These co-PDC plumes rise in the atmosphere until reaching a level of neutral buoyancy and disperse laterally like umbrella clouds, however co-PDCs clouds are typically much smaller (Constantinescu et al., 2021;

Mastin & Van Eaton, 2020; F. Prata et al., 2025; Zidikheri et al., 2017). In some cases, they can become negatively buoyant downwind and descend to the ground (Engwell & Eychenne, 2016), thus increasing the ground area impacted by the co-PDC. In this contribution, we use the term 'plumes' to refer to the near-source behaviour of the buoyant column, whereas the downwind transport and dispersion of ash is referred to as 'ash clouds'.

Co-PDC plumes and clouds have unique characteristics and are different to typical Plinian eruption columns and their associated ash clouds. For example, co-PDCs typically have a narrower particle size distribution and are composed of smaller particles ($< 90\,\mu m$) (Engwell & Eychenne, 2016; Sigurdsson & Carey, 1989). This is because during co-PDC formation and plume lift-off, the coarser (heavier) particles remain in the underlying pyroclastic density current (Andrews & Manga, 2012; Woods & Kienle, 1994). Similarly, their componentry is mostly juvenile-rich (i.e., composed mainly of volcanic ash) as the denser accessory components such as lithics preferentially remain in the main current (Engwell & Eychenne, 2016; Sigurdsson & Carey, 1989). The plumes lift off from a source geometry that is of high aspect ratio (i.e., an irregular, elongated, rectangular ground footprint and not a circular vent). Furthermore, the source area is not necessarily at the eruption vent location as co-PDCs can be generated and lift-off from all parts of the associated PDC, including its entire length (Andrews & Manga, 2011; Engwell & Eychenne, 2016; Sparks et al., 1986, 1997).

Some numerical 1D models have previously been used to model co-PDC plume rise (Calder et al., 1997; Woods & Kienle, 1994; Woods & Wohletz, 1991) and they assume a thermal equilibrium between particles and gas and a well-mixed, homogenous suspension (Engwell et al., 2016; Woods & Wohletz, 1991). Specifically, Calder et al. (1997), Engwell et al. (2016), Sparks et al. (1997), and Woods and Wohletz (1991) adapted steady state column models commonly used for vent-derived plumes to simulate the formation of a co-PDC plume from an underlying pyroclastic density current. Other studies such as Woods and Kienle (1994) applied a thermal model to simulate small plumes rising as a discrete, buoyant thermal. Multidimensional models have also been applied to co-PDC plumes. Neri et al. (2002, 2003) mainly investigated the material properties and the multiphase nature of the flow and Herzog and Graf (2010) used a 3D model to highlight the limits of 1D models for co-PDC plumes. Additionally, Engwell et al. (2016) used work from Bursik (2001) and Bursik and Woods (1996) to couple PDC and plume models to understand co-PDC plume formation requirements and the plume heights they can achieve.

Co-PDCs can be generated during an explosive eruption and can disperse large volumes of ash over great distances (Engwell & Eychenne, 2016), impacting the environment and potentially impacting aviation (Engwell et al., 2016; Folch et al., 2012; Pardini et al., 2024; Webster et al., 2012; Witham et al., 2012). Despite global applicability and potential global impact, relatively little modelling has been performed to consider the implications of source parameters characteristic of co-PDCs on the downwind location, extent and concentrations of ash in the atmosphere. The Numerical Atmospheric-dispersion Modelling Environment (NAME) is used operationally by the

London Volcanic Ash Advisory Centre (VAAC). Here, we perform a set of NAME model runs to systematically evaluate the impact of co-PDC source geometry, the mass eruption rate, and the associated plume height on the modelled transport and dispersion of the volcanic ash cloud. This allows us to determine which co-PDC eruption source parameters are most important for modelling these ash clouds using NAME.

2.2 Methods

Ash dispersion and transportation modelling were performed using the UK Met Office's Numerical Atmospheric-dispersion Modelling Environment, NAME, in its Lagrangian configuration. Specifically, here, version NAME III v8.5 was used (Beckett et al., 2020; A. Jones et al., 2007). NAME simulates the transport and dispersion of particles (e.g., particulate matter, volcanic ash, wind-spread diseases, radionuclides, and pollen) in the atmosphere. In NAME, a large number of modelled particles are released into a model environment where they are advected by three-dimensional wind fields, provided by a Numerical Weather Prediction (NWP) model, and dispersed using random walk techniques which account for subgrid turbulent motion in the atmosphere.

In this study, a fictitious volcanic co-PDC plume and its generated ash cloud were modelled. We assumed that a volcanic eruption produced a PDC and generated an associated co-PDC plume. Our model started at the point of lateral ash injection into the atmosphere and, using NAME, we modelled the transport and dispersion of the ash cloud generated by the co-PDC plume. To understand which eruption source parameters (ESPs) control atmospheric dispersion of co-PDC ash clouds, we performed a systematic series of 63 NAME model runs. The particle characteristics, eruption location, eruption start time, duration, and the field proportions (i.e., horizontal grid resolution of 0.1° in Lat and Long) were all kept constant. The source geometry and, thus indirectly, its area and location, were systematically varied. The specific ESPs used are detailed in the following subsections. In all cases, we assumed time homogeneity, meaning that for each model run, the parameters did not vary as a function of time (i.e., the source area was a constant value within each run). We assumed a constant vertical distribution of particles as well as no overshoot height and therefore reduced complexity, compared to real events observed in nature, e.g. for Mount St. Helens on May 18th 1980 (Mastin, Carey, et al., 2022; Sparks et al., 1986), where the plume height and mass distribution varied during the eruption. In all runs, we also used the wet and dry deposition schemes in NAME to replicate removal of ash from the atmosphere; for further information, see Dacre et al. (2011), Harvey et al. (2018), and Webster et al. (2012).

2.2.1 Eruption Timing, Location and Meteorology Data

In this study, we use pre-processed global configured NWP data from the Met Office Unified Model (UM) (Beckett et al., 2020; A. Brown et al., 2012; Davies et al., 2005; Walters et al., 2019). In

addition to the weather and turbulence, unresolved mesoscale motions, which are not resolved by the NWP model, are also represented (Webster et al., 2018). We used the global configuration of the UM, which used a standard latitude-longitude coordinate system and provided a global dataset with a horizontal resolution with grid lengths of approximately $10\,\mathrm{km}$ at mid-latitudes. The vertical resolution decreases with increased altitude, for example near ground level datasets are available at $\sim 0.3\,\mathrm{km}$ intervals, whereas at a $30\,\mathrm{km}$ altitude this interval reduces to $\sim 1.9\,\mathrm{km}$. However, despite this resolution reduction, the vertical variation of weather also reduces with altitude. These meteorological data include the wind speed and direction, temperature, pressure, clouds, precipitation and the ground topography for each grid cell.

For this project, the volcano Hekla in Iceland was selected as the source location; however, our study is not unique to Hekla as we investigate the ash cloud and NAME model sensitivity, and the focus is not on any specific local topographic effects or unique volcano properties. Hekla is situated at 63.98°N, and 19.67°W (Global Volcanism Program, 2024) in the south of Iceland, has a vent elevation of $1490\,\mathrm{m}$ (Global Volcanism Program, 2024), and is $51\,\mathrm{km}$ away from the Atlantic Ocean, thus no interaction with seawater was considered. The release of modelled ash at a given height in the atmosphere was initialised at 09:00 UTC on the 31$^{\mathrm{st}}$ of January 2022 and particles were emitted for $1\,\mathrm{h}$. This start time/day was chosen as the wind fields were not extreme and, in general, travelled in an SE direction, towards Europe. Figure 2.1 shows the wind fields on 31$^{\mathrm{st}}$ of January 2022 at 09:00 UTC (the start of ash release) and one hour after, at 10:00 UTC (the end of ash release). The wind fields at $0.01\,\mathrm{km}$, above ground level (agl), and at $8.5\,\mathrm{km}$ agl show large differences, as displayed in Figure 2.1. Near the surface ($0.01\,\mathrm{km}$ agl; Figure 2.1a & b), the wind over Iceland was slower than over the ocean. Over Hekla, wind speeds were very low, with a slight orientation towards NE and NW. The wind field at $0.01\,\mathrm{km}$ agl was clearly impacted by the ground topography and the coastline. Whereas at higher elevation ($8.5\,\mathrm{km}$ agl (Figure 2.1c & d) westerly winds were present over Hekla.

2.2.2 Source Geometry and Location

As co-PDCs are derived from ground-hugging PDCs, the source of ash into the atmosphere may not occur from the vent location. Here, the source was always positioned immediately to the east of the volcanic vent in all runs, such that the meteorological conditions at the source location remained constant between runs. The source geometry, in plan/map view, for the co-PDC plumes simulated here has a rectangular shape with a width, *dx*, and length, *dy*, and together these parameters define the source aspect ratio:

$$\alpha = \frac{dx}{dy} \tag{2.1}$$

All PDCs have the potential to produce co-PDC plumes, which can lift off from the entire underlying pyroclastic density current (Engwell & Eychenne, 2016; Sparks et al., 1997). To bracket the range of co-PDC source areas liekly in nature, we measured the source of the largest and smallest

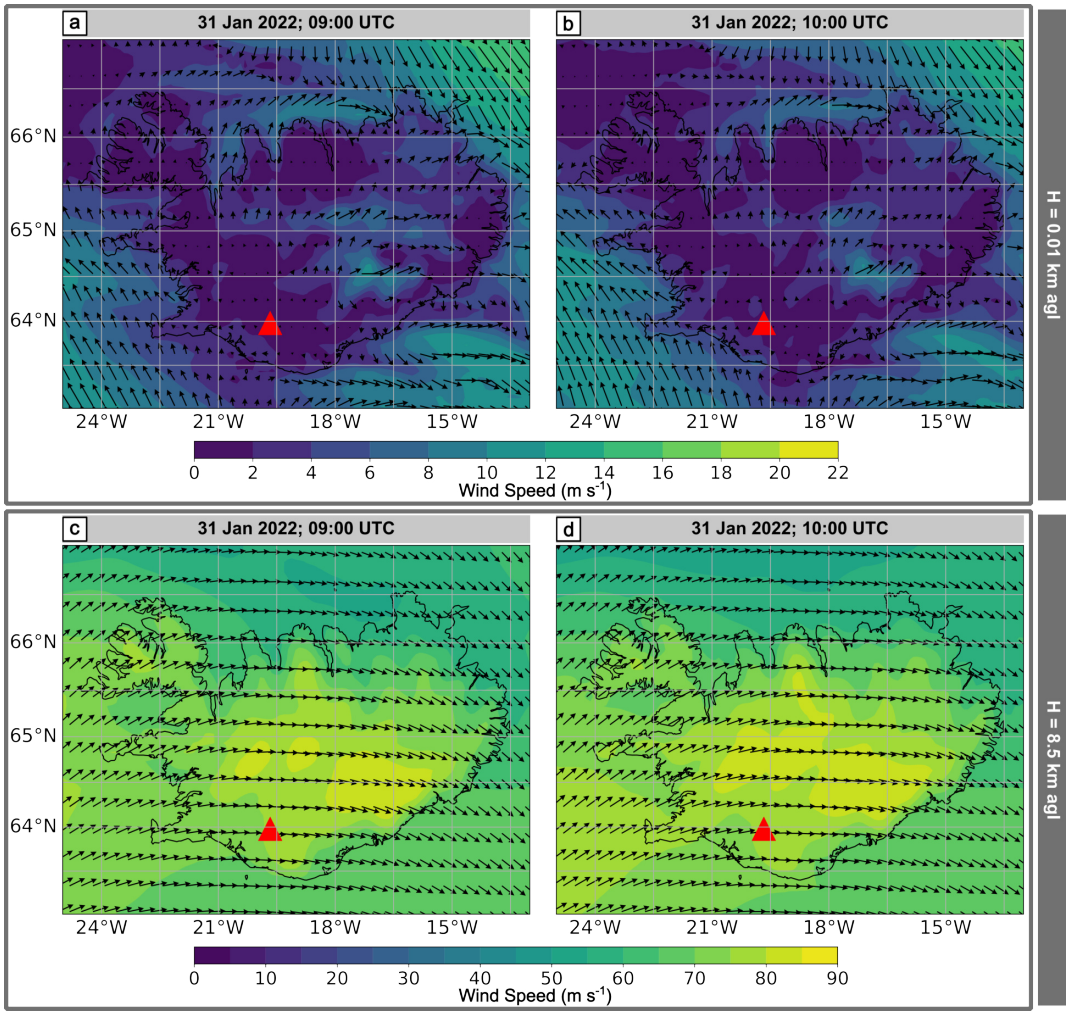

Figure 2.1: Meteorological data for Iceland on 31st of January 2022. The red triangle shows the location of Hekla, where the simulated co-PDC plume is sourced. The top two panels show the wind behaviour at $10\,\mathrm{m}$ agl elevation at times **(a)** 09:00 UTC, start of particle release and **(b)** 10:00 UTC, the end of particle release. The colour bar ranges between 0-$22\,\mathrm{m\,s^{-1}}$. The wind direction and speed were relatively constant over the two hours, although the field is impacted by topography and the coastline. The bottom two panels show the wind field at $8.5\,\mathrm{km}$ agl elevation for **(c)** 09:00 UTC and **(d)** 10:00 UTC. The colour bar ranges from 0-$90\,\mathrm{m\,s^{-1}}$, and the wind field was relatively homogeneous.

well-documented co-PDCs. Specifically, the May 18th, 1980 eruption of Mount St. Helens (MSH) generated a large co-PDC with a lift-off from the entire blast area, A, and the 1991 eruption of Unzen generated a relatively small co-PDC plume again, from the entire PDC ground footprint (Engwell et al., 2016; Holasek & Self, 1995; Sparks et al., 1986, 1997; Watanabe et al., 1999). These areas are shown in Figure 2.2. The area of the blast/deposit and the area of the source geometry are highlighted in dark and light red, respectively. Unzen had a total PDC deposit area of $0.4\,\mathrm{km^2}$ and an aspect ratio of $\alpha = 0.2$. MSH had a blast/PDC deposit area of approximately

$619\,\mathrm{km}^2$ and an aspect ratio of $\alpha = 1.7$. The minimum (from Unzen) and maximum (from MSH) observed aspect ratios were used for our numerical experiment as end-member parameters. The PDC flow/blast direction has been defined as *dy*; *dx* therefore is perpendicular to the PDC flow direction. For each aspect ratio, we varied the area logarithmically between the deposit area of Unzen and MSH. The following describes how width and length are calculated using the area and aspect ratio to initialise the model:

$$dx \cdot dy = A \tag{2.2}$$

With Equation 2.1, *dx*:

$$dx = \sqrt{A \cdot \alpha} \tag{2.3}$$

dy with Equation 2.1 becomes:

$$dy = \sqrt{\frac{A}{\alpha}} \tag{2.4}$$

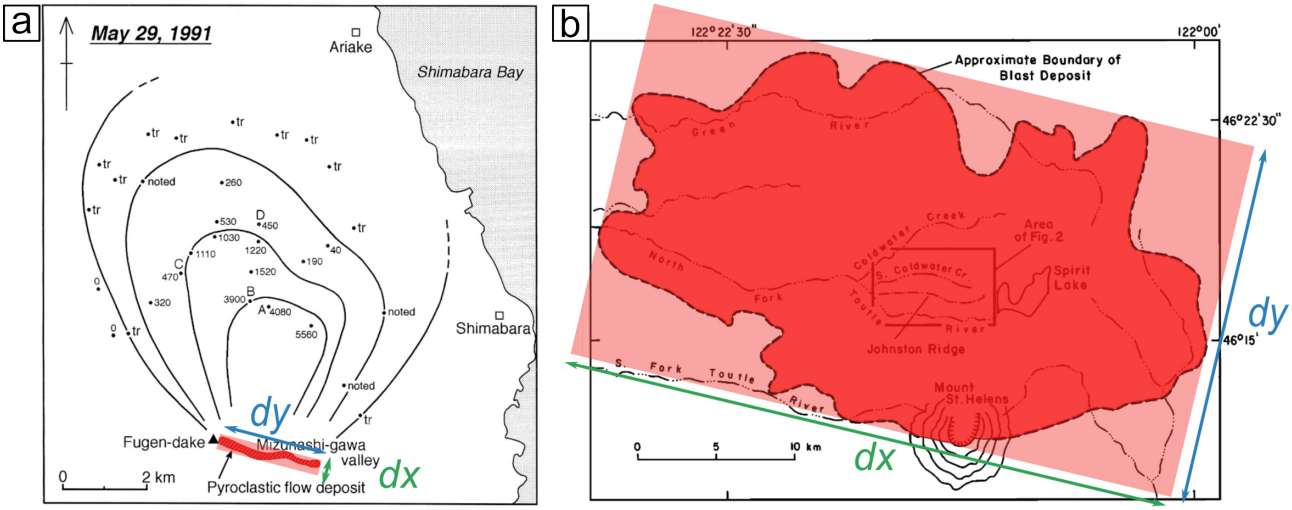

Figure 2.2: PDC deposit area shown in dark red for **(a)** the May 29th, 1991 eruption of Mount Unzen, Japan and **(b)** the May 18th, 1980 eruption of Mount St. Helens, USA. Base maps were taken from Watanabe et al. (1999) with permission from Elsevier and Fisher et al. (1987) with permission from Wiley, respectively, and for **(a)** the associated co-PDC fallout is shown by the isopach map. The numbers refer to a mass of ash in a unit area $\mathrm{g\,m}^{-2}$ where tr = trace of ash-fall deposit. The aspect ratio defining the source geometry, i.e., the area of co-PDC lift off, is highlighted in transparent, light red. The orientation of *dx* and *dy* were defined by the volcano location (*dy* aligns with the PDC flow/blast direction; *dx* therefore is perpendicular to the PDC flow direction).

2.2.3 Eruption conditions

To determine the maximum height of the co-PDC plumes, H_T, datasets from Aubry et al. (2021), Eychenne and Engwell (2022), Mastin et al. (2009), and Pioli et al. (2019) were used and are all

reported in terms of the elevation above ground level (agl). The relationship between the maximum plume height in km, H_T, and the mass eruption rate, MER, in $\mathrm{g\,h^{-1}}$ follows an empirical power law (Aubry et al., 2023; Mastin et al., 2009; Morton et al., 1956; Sparks, 1986; L. Wilson et al., 1978). The mass eruption rate, MER, also termed the source strength, describes the mass flux per total source area and is commonly derived from H_T when atmospheric dispersion models, like NAME, are used operationally (Beckett et al., 2024). This is because the plume height is much easier to determine in real-time (e.g., radar, lidar measurements, or visual observation) compared to the MER (Dürig et al., 2018; Folch et al., 2012; Pioli & Harris, 2019). In this study, we used the following relationship based on Aubry et al. (2023), between H_T and MER:

$$\mathrm{MER} = \sqrt[0.226]{\frac{H_T}{0.345}} \tag{2.5}$$

While the relationship of Aubry et al. (2023) is predominantly defined using information from vent-derived plumes due to a lack of erupted mass information for co-PDCs, the plume height and mass eruption rate from the MSH co-PDC plume fall within the confidence interval of the fit, and imply that, for at least the largest co-PDC events, this relationship is appropriate.

The ash plume spreads laterally at the neutral buoyancy level, where the density of the plume and the surrounding atmosphere are equal (Carey & Sparks, 1986). This constitutes the umbrella region of the plume and is characterised by a thickness, *dz*, which corresponds to the height interval of the ash release within the model (Figure 2.3). The following ratio by Carey and Sparks (1986),

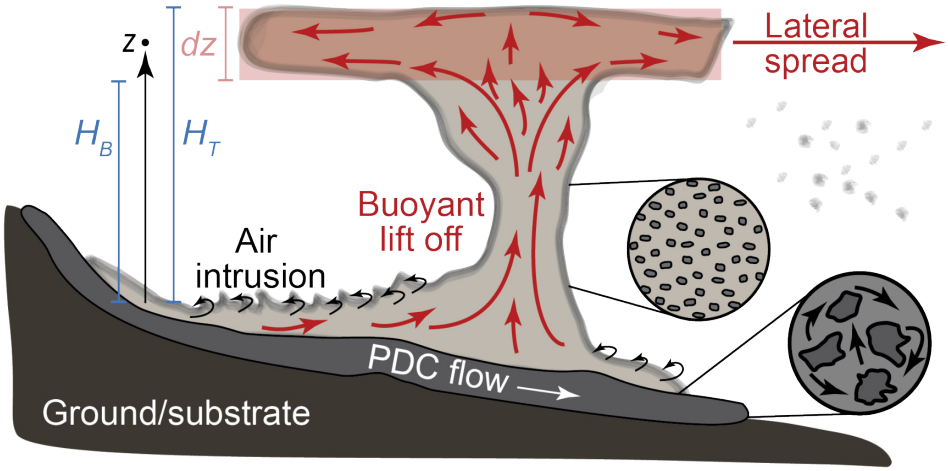

Figure 2.3: Characteristics of co-PDC plumes. Through air entrainment, parts of the ground-hugging pyroclastic density current become buoyant, and a hot gas-ash mixture lifts off to form a co-PDC plume. The plume reaches a top height, H_T, and spreads laterally at the level of neutral buoyancy, where the particles are dispersed over a vertical thickness, *dz*, (between H_T and H_B) with a mid-point elevation, *z*.

Morton et al. (1956), and Sparks (1986) describes the relationship between the thickness of the

umbrella region and the total column height:

$$dz = H_T - H_B = x \cdot H_T \tag{2.6}$$

H_B is the base of the spreading cloud, and x can take values in the range 0.25 to 3. Here, we use $x = 0.3$ due to the relationship $H_T = \frac{H_B}{0.7}$ (Bonadonna & Phillips, 2003). This relationship holds true for small co-PDc plumes and for all under the assumption of no umbrella overshoot.

For our model set up in NAME, we also define the mid-point, z, within the height interval of released ash. The relationships between H_T, H_B, dz, and z are shown visually in Figure 2.3 and are mathematically expressed as:

$$z = H_T - \frac{1}{2} \cdot dz \tag{2.7}$$

With substituting Equation 2.6 into Equation 2.7 we obtain the final expression for z:

$$z = 0.85 \cdot H_T \tag{2.8}$$

A full quantitative summary of the ranges of these parameters used in this study is presented in Table 2.1.

Table 2.1: Co-PDC source parameters defined for historical PDC and co-PDC eruptions. The minimum data (referring to the 1991 eruption of Unzen) for A, α and dx are taken from Watanabe et al. (1999), whereas the maximum data (referring to the May 18th, 1980 eruption of Mount St Helens (MSH)) for A, α and dy are taken from Fisher et al. (1987). We used Unzen and MSH as end-members to describe potential co-PDC plume parameters and behaviour. H_T is taken from data sets from Aubry et al. (2021), Eychenne and Engwell (2022), Mastin et al. (2009), and Pioli et al. (2019) and dz from Bonadonna and Phillips (2003) and Carey and Sparks (1986).

Parameter	Symbol	Unit	Min	Max
Area	A	km^2	0.4	619
Aspect ratio	α	-	0.2	1.7
Width of source in plan view	dx	km	0.3	32.4
Length of source in plan view	dy	km	0.5	55.6
Maximal plume height	H_T	km	1	30
Thickness of ash release	dz	km	0.3	9.0

2.2.4 Particle Characteristics

Ash particles that comprise co-PDCs have been found to have densities between 2200-$2600\,\mathrm{kg\,m^{-3}}$ (Bonadonna & Phillips, 2003; Watanabe et al., 1999). Given this narrow range and that Beckett et al. (2015) showed that differences in particle densities over this range have no significant impact on NAME output, we used $2500\,\mathrm{kg\,m^{-3}}$ for all our experimental runs.

The total grain size distribution (TGSD) of a co-PDC plume (modified from Marti et al. (2016)) was used for the particle size distribution (PSD) in NAME and thus described the diameter, *d*, of the particles. The range of particle diameters was split into nine bins with 1.5 φ intervals between 11.25 φ and -0.75 φ, where φ (phi) is defined as $\varphi = -\log_2(d(\text{mm}))$. The calculated distribution used in this study is shown in Table 2.2 and all particles were treated as spheres. The cumulative mass distribution is shown in Figure 2.4.

Table 2.2: Total grain size distribution (TGSD) modified from Marti et al. (2016). The particle diameters, *d*, were grouped into equally spaced bins with steps of 1.5 φ.

d (φ-scale)	*d* (μm)	Cumulative volume
11.25	0.41	0
9.75	1.16	0.0051
8.25	3.28	0.0415
6.75	9.29	0.1799
5.25	26.28	0.4882
3.75	74.33	0.8027
2.25	210.22	0.9433
0.75	594.60	0.9864
-0.75	1681.79	1

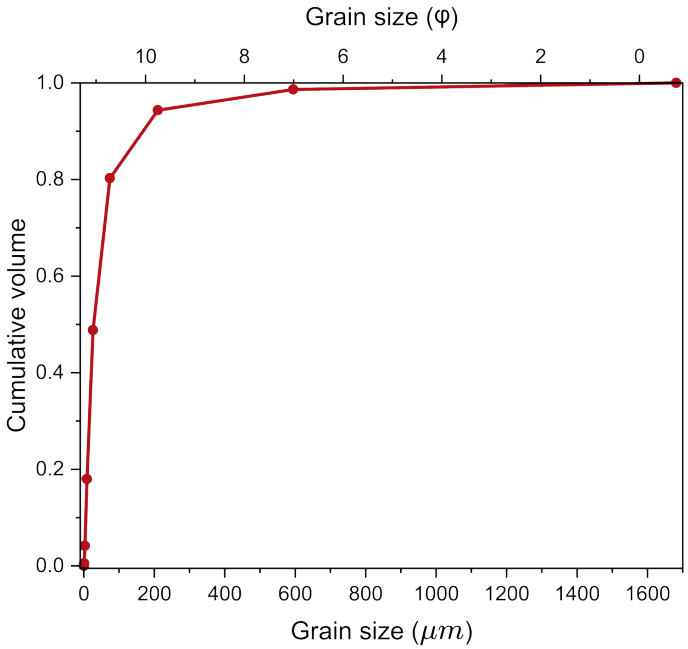

Figure 2.4: The cumulative volume distribution for the applied (and modified) TGSD from Marti et al. (2016).

2.2.5 Numerical Experiments

We performed two numerical experiments. In the first numerical experiment, we used a constant source strength and plume height but used three different source aspect ratios changing the source area, thus the width and length of the source geometry. In our assumption, the area and shape of the ground footprint were the same used at the level of neutral buoyancy for particle release. We neglect any plume widening during the rise. This allowed us to independently investigate the impact of the source geometric properties on dispersion. In the second numerical experiment, we appropriately coupled the plume height, height interval of ash release, and source strength for each run and modelled a range of source geometries and areas. This represents a more realistic set of eruption conditions and allows us to test the influence of MER/H_T on the simulated location and concentrations of ash in the downwind cloud.

2.2.5.1 Numerical Experiment 1: Source Aspect Ratio and Area

This experimental set analysed the impact of the aspect ratio and total source area on the plume shape and position. The minimum and maximum aspect ratios were determined from the literature as 0.2 and 1.7, respectively and a mid-point value was simply calculated (0.95) to provide a third aspect ratio (cf. Table 2.1; Figure 2.2). For each of these aspect ratios (0.2, 0.95, and 1.7), ten different source areas between $0.4\,\mathrm{km}^2$ and $619\,\mathrm{km}^2$ (Table 2.1) and the logarithmic mid-point were used. The full model set up conditions that comprise the numerical experiment 1 are displayed in Table 2.3. All other eruption source parameters were kept constant: H_T was set to $10\,\mathrm{km}$ (agl) and thus yielded a *dz* of $3\,\mathrm{km}$ and *z*, the mid plume height, was $8.5\,\mathrm{km}$. The source strength was set to $1.06 \times 10^{13}\,\mathrm{g\,h^{-1}}$.

2.2.5.2 Numerical Experiment 2: Coupled H_T and MER for different *A* and α

This numerical experiment better represents the natural case, by the appropriate coupling of the plume height H_T, the vertical thickness of ash release *dz*, and the MER. Specifically, five different total plume heights were chosen following Table 2.1, covering the full range of heights expected for natural co-PDC plumes.

For each plume height, the coupled source strength (MER) was calculated using Equation 2.5 and the thickness of ash release by Equation 2.6. All other parameters, such as the particle size distribution, the eruption start time (thus meteorological conditions), and the emission duration, were kept constant and are the same as in experiment 1. These different cases have all been modelled by using two different aspect ratios and the min and max source geometry areas with both wet and dry deposition included. Table 2.4 provides the full model set-up conditions of numerical experiment 2, indicating the plume height *dz*, MER, α, *A*, *dx*, *dy*, and the run number for each model run.

Table 2.3: Source parameters of numerical experiment 1. Three different aspect ratios were each used for eleven different source geometry areas. The width and length of the geometry were determined by Equation 2.3 and Equation 2.4. Runs (1) to (11) used an aspect ratio of 0.2, runs (12) to (22) used an aspect ratio of 1.7, and runs (23) to (33) used the mid aspect ratio of 0.95. The source perimeter $P = 2 \cdot dx + 2 \cdot dy$ is indicated for comparison.

α = **0.2**	**(1)**	**(2)**	**(3)**	**(4)**	**(5)**	**(6)**	**(7)**	**(8)**	**(9)**	**(10)**	**(11)**
A (km^2)	0.4	1	2	5	10	16	24	50	121	274	619
dx (km)	0.3	0.4	0.6	0.9	1.4	1.8	2.2	3.6	4.9	7.4	11.1
dy (km)	1.4	2.1	3.2	4.8	7.2	8.9	10.9	15.9	24.6	37.0	55.6
P (km)	3.4	5.0	7.6	11.6	17.2	21.4	26.2	38.2	59.0	88.8	133.4
α = **1.7**	**(12)**	**(13)**	**(14)**	**(15)**	**(16)**	**(17)**	**(18)**	**(19)**	**(20)**	**(21)**	**(22)**
A (km^2)	0.4	1	2	5	10	16	24	50	121	274	619
dx (km)	0.8	1.2	1.9	2.8	4.2	5.2	6.3	9.3	14.3	21.6	32.4
dy (km)	0.5	0.7	1.1	1.6	2.5	3.1	3.7	5.4	8.4	12.7	19.1
P (km)	2.6	3.8	6.0	8.8	13.6	16.6	20.0	29.4	45.4	68.6	103.0
α = **0.95**	**(23)**	**(24)**	**(25)**	**(26)**	**(27)**	**(28)**	**(29)**	**(30)**	**(31)**	**(32)**	**(33)**
A (km^2)	0.4	1	2	5	10	16	24	50	121	274	619
dx (km)	0.6	0.9	1.4	2.1	3.2	3.9	4.7	6.9	10.7	16.1	24.2
dy (km)	0.6	1.0	1.5	2.2	3.3	4.1	5.0	7.3	11.3	17.0	25.5
P (km)	2.4	3.8	5.8	8.6	13.0	16.0	19.4	28.4	44.0	66.2	99.4

Table 2.4: Source parameters for numerical experiment 2. Different total plume heights defined the thickness of ash release and source strength, which were tested for different source geometries (aspect ratios and areas). The label for each model run is given in brackets and highlighted in grey.

H_t (km)	***z*** (km)	***dz*** (km)	**MER**	α	**Source geometry**			
1	0.85	0.3	$1.41 \times 10^2\,\mathrm{kg\,s^{-1}}$ = $5.07 \times 10^8\,\mathrm{g\,h^{-1}}$	0.2	**Run**	**(1)**	**(2)**	**(3)**
					A (km^2)	0.4	16	619
					dx (km)	0.3	1.8	11.1
					dy (km)	1.4	8.9	55.6
					P (km)	3.4	12.5	133.4
				1.7	**Run**	**(4)**	**(5)**	**(6)**
					A (km^2)	0.4	16	619
					dx (km)	0.8	5.2	32.4
					dy (km)	0.5	3.1	19.1
					P (km)	2.6	16.6	103.0
					Run	**(7)**	**(8)**	**(9)**

Continued on next page

5	4.25	1.5	$1.12 \times 10^5\,\mathrm{kg\,s^{-1}}$ = $4.03 \times 10^{11}\,\mathrm{g\,h^{-1}}$	0.2	***A*** (km^2)	0.4	16	619
					dx (km)	0.3	1.8	11.1
					dy (km)	1.4	8.9	55.6
					P (km)	3.4	12.5	133.4
				1.7	***A*** (km^2)	0.4	16	619
					dx (km)	0.8	5.2	32.4
					dy (km)	0.5	3.1	19.1
					P (km)	2.6	16.6	103.0

Table 2.4 – continued from previous page

H_t (km)	*z* (km)	*dz* (km)	MER	α	Source geometry			
					A (km^2)	0.4	16	619
					dx (km)	0.3	1.8	11.1
					dy (km)	1.4	8.9	55.6
					P (km)	3.4	12.5	133.4
					Run	**(10)**	**(11)**	**(12)**
					A (km^2)	0.4	16	619
				1.7	***dx*** (km)	0.8	5.2	32.4
					dy (km)	0.5	3.1	19.1
					P (km)	2.6	16.6	103.0

Continued on next page

Table 2.4 – continued from previous page

H_t (km)	*z* (km)	*dz* (km)	MER	α	Source geometry			
10	8.5	3.0	$1.99 \times 10^6\,\mathrm{kg\,s^{-1}}$ = $7.15 \times 10^{12}\,\mathrm{g\,h^{-1}}$	0.2	**Run**	**(13)**	**(14)**	**(15)**
					A (km^2)	0.4	16	619
					dx (km)	0.3	1.8	11.1
					dy (km)	1.4	8.9	55.6
					P (km)	3.4	12.5	133.4
				1.7	**Run**	**(16)**	**(17)**	**(18)**
					A (km^2)	0.4	16	619
					dx (km)	0.8	5.2	32.4
					dy (km)	0.5	3.1	19.1
					P (km)	2.6	16.6	103.0
20	17.0	6.0	$3.53 \times 10^7\,\mathrm{kg\,s^{-1}}$ = $1.27 \times 10^{14}\,\mathrm{g\,h^{-1}}$	0.2	**Run**	**(19)**	**(20)**	**(21)**
					A (km^2)	0.4	16	619
					dx (km)	0.3	1.8	11.1
					dy (km)	1.4	8.9	55.6
					P (km)	3.4	12.5	133.4
				1.7	**Run**	**(22)**	**(23)**	**(24)**
					A (km^2)	0.4	16	619
					dx (km)	0.8	5.2	32.4
					dy (km)	0.5	3.1	19.1
					P (km)	2.6	16.6	103.0
27	22.95	8.1	$1.22 \times 10^8\,\mathrm{kg\,s^{-1}}$ = $4.41 \times 10^{14}\,\mathrm{g\,h^{-1}}$	0.2	**Run**	**(25)**	**(26)**	**(27)**
					A (km^2)	0.4	16	619
					dx (km)	0.3	1.8	11.1
					dy (km)	1.4	8.9	55.6
					P (km)	3.4	12.5	133.4
				1.7	**Run**	**(28)**	**(29)**	**(30)**
					A (km^2)	0.4	16	619
					dx (km)	0.8	5.2	32.4
					dy (km)	0.5	3.1	19.1
					P (km)	2.6	16.6	103.0

2.3 Results

In this section, we will show the results from our systematic NAME model runs (as outlined in Table 2.3 & Table 2.4) and consider the individual impact of different source parameters on the dispersion of the co-PDC ash cloud. To do this, and to provide a common comparison across all runs,

we use the horizontal position and extent of the whole ash cloud and the total column mass loading of the ash particles. Where the total column mass loading is the sum of all ash particles vertically above the ground at a given location and thus has units of $\mathrm{g\,m^{-2}}$. These data are extracted every hour after the emission/eruption started (t_0) up until 24 hours later ($24\,\mathrm{h}$ since t_0).

2.3.1 Impact of source area, *A*

First, let us consider the impact of the source area, *A*, for a constant source aspect ratio, α. Figure 2.5 provides an overview of the size and orientation of all source geometries used in this study. They are shown in their true locations with respect to Hekla volcano (black triangle) and to Iceland. For context, Iceland has a total land area of approximately $104\,000\,\mathrm{km^2}$ and the minimum and maximum co-PDC plume source area were $0.4\,\mathrm{km^2}$ and $619\,\mathrm{km^2}$, respectively.

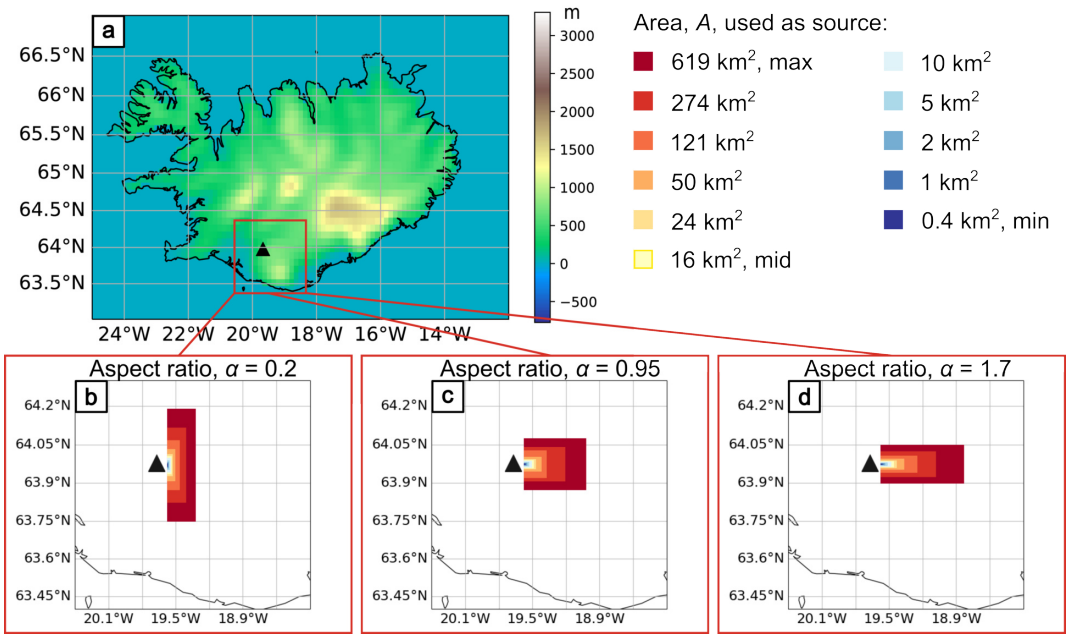

Figure 2.5: Orientation and size of the source for the different aspect ratios and areas used in our model runs. **(a)** A map of Iceland, showing the ground elevation using the global $10\,\mathrm{km}$ resolution topography data used with the NAME simulations. The colour bar shows the ground elevation in meters above sea level. The lower panels show the range of source areas for aspect ratios, **(b)** $\alpha_{min} = 0.2$, **(c)** $\alpha_{mid} = 0.95$, and **(d)** $\alpha_{max} = 1.7$ used in this study.

To compare the ash cloud generated by different source geometry areas, we plot the dispersal areas from a $0.4\,\mathrm{km^2}$ (min) and $619\,\mathrm{km^2}$ (max) source area, both with aspect ratio, $\alpha_{min} = 0.2$. These results are shown in Figure 2.6. The simulated ash clouds grow with time, following the wind field towards the east and show similar dispersal shapes. The initial latitudinal extent of the

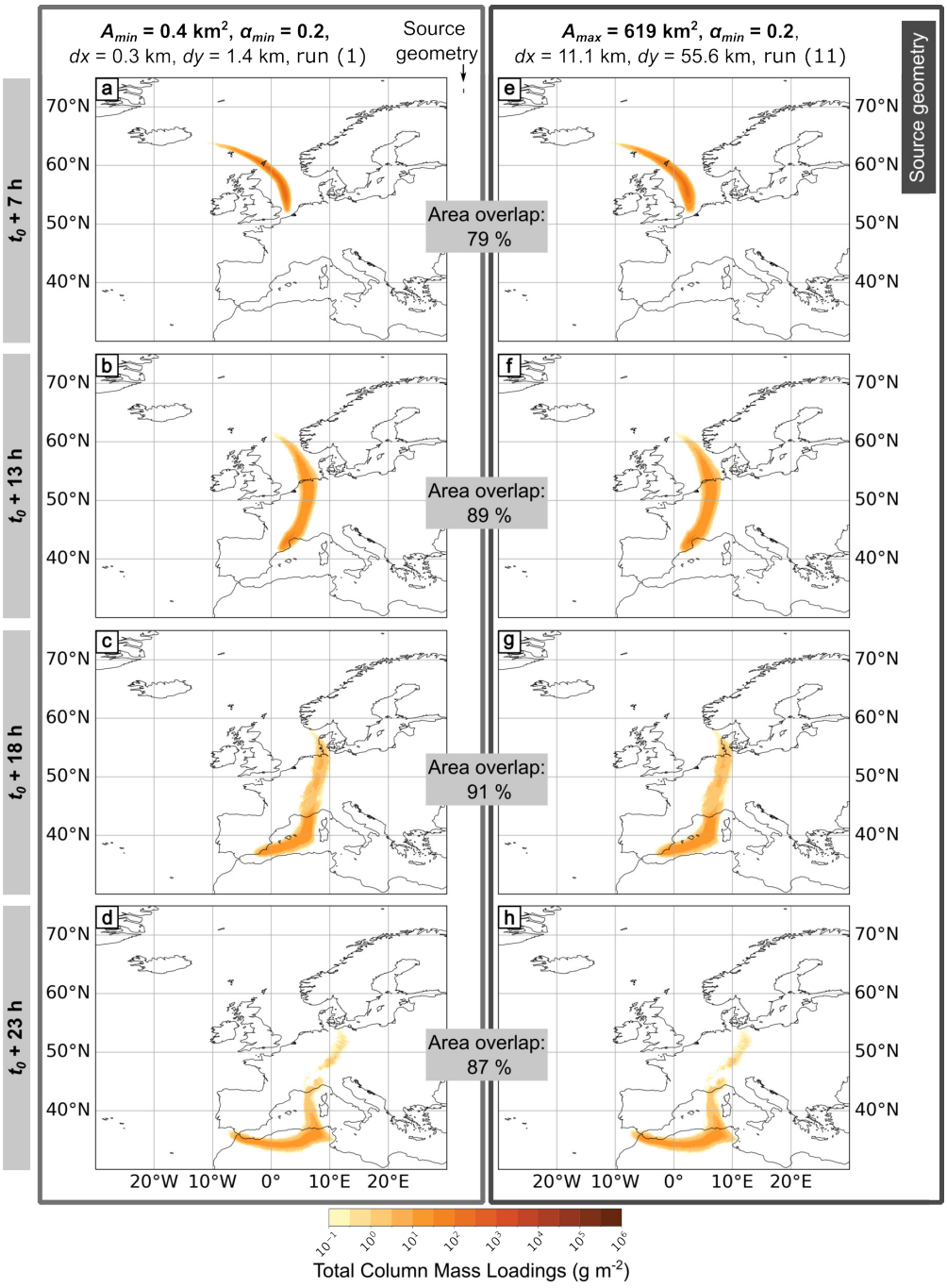

Figure 2.6: NAME outputs for numerical experiment 1, all using $\alpha_{min} = 0.2$, a $1\,\mathrm{h}$ particle release, $z = 8.5\,\mathrm{km}$, $dz = 3\,\mathrm{km}$ and MER $= 1.06 \times 10^{13}\,\mathrm{g\,h^{-1}}$. The panels on the left are for the minimum source area, and the panels on the right are for the maximum. The area and orientation of the two source geometries are compared in relation to each other next to the parameter list at the top of the figure. For each area, four outputs are presented at different times after the eruption start t_0: **(a & e)** $7\,\mathrm{h}$, **(b & f)** $13\,\mathrm{h}$, **(c & g)** $18\,\mathrm{h}$, and **(d & h)** $23\,\mathrm{h}$. Total column mass loadings are averaged over the previous hour, and we applied a threshold of $0.2\,\mathrm{g\,m^{-2}}$.

ash clouds close to the source location shows the most deviation; however, as the age of the cloud increases and it becomes more dispersed, the differences between the simulations initialised with minimum and maximum source area are insignificant.

Quantitatively, the difference in cloud position was compared between these two end-member cases using the Figure of Merit in Space, FMS (Rolph et al., 2014; Warner et al., 2004):

$$\text{FMS} = \frac{A_1 \cap A_2}{A_1 \cup A_2} \cdot 100 \tag{2.9}$$

where A_1 is the cloud area within one model output and A_2 the cloud area in another model output. The intersection is compared with the union of these areas. The areas A_n are the forecasted cloud areas having mass loading $\geq 0.2\,\mathrm{g\,m^{-2}}$ for both model outputs that are compared. The areas and their location are then compared and the percentual overlap, i.e., FMS, is its result. High values for FMS correspond to high agreement between the models. These results are shown in Figure 2.7a. The threshold of $0.2\,\mathrm{g\,m^{-2}}$ was chosen as it aligns to the threshold which, typically, satellite instruments can detect and retrieve volcanic ash (Saint et al., 2024) and the lowest concentration threshold on VAAC forecasts, if we assume the ash cloud has a $1\,\mathrm{km}$ thickness (Beckett et al., 2020).

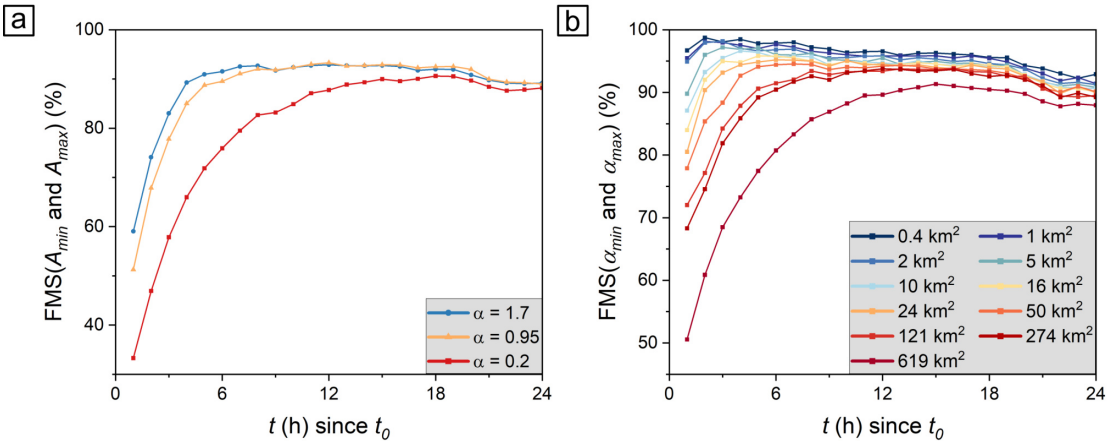

Figure 2.7: The Figure of Merit in space (FMS) within numerical experiment 1 determined by Equation 2.9. **(a)** FMS between the plumes generated using minimum (A_{min}) and maximum (A_{max}) source area. The different coloured data points correspond to different aspect ratios. In general, there is the least area overlap for $\alpha_{min} = 0.2$ and for all aspect ratios, the overlap increases with time after t_0 until it reaches a plateau at $\sim$ 90% overlap and slightly decreases after $\sim$ 20 h. **(b)** The ash cloud overlap between the minimum (α_{min}) and maximum (α_{max}) aspect ratio. The smaller the source area, the higher the agreement in area overlap. The overlap increases, reaches a plateau (at 90-95%) and decays slowly with time. The minimal overlap of $A_{max} = 619\,\mathrm{km^2}$ is 88% at $24\,\mathrm{h}$ since t_0. The lines between data points are not model fits and are just used to guide the eye.

For all aspect ratios, the overlap between the ash clouds generated by model runs using the minimum (A_{min}) and maximum (A_{max}) source area increases with time after t_0 until a plateau

is reached. The near-source variations are more pronounced as there is less total cloud area to compare with. The plateau occurs at $\sim$ 90% overlap for all aspect ratios but is achieved faster for the larger aspect ratios. Additionally, in all cases, there is a slight decrease in the percentage overlap after $\sim 20\,\mathrm{h}$. We also find that there is the least overlap for $\alpha_{min} = 0.2$ and for a set time after particle emission, larger aspect ratios show more overlap between the ash clouds sourced from A_{min} and A_{max}. However, it must be stressed that this is not strictly related to the value of the aspect ratio but to the applied weather conditions. This can be visualised in Figure 2.5 as the larger areas with $\alpha_{min} = 0.2$ show a larger longitudinal extension. The extension in source geometry is perpendicular to the wind direction and thus more variability in the particle trajectories is produced (especially in early hours since t_0). If the source geometry is elongated with its long axis in the dominant wind direction (the larger of *dx* or *dy* is parallel to the wind direction), there is a lower impact on differences in particle trajectories.

The definition of the aspect ratio (Equation 2.1) as the ratio between *dx* and *dy* is a choice made by the authors to highlight the relationship between the width and the length of the source area. This enable aspect ratios to range between almost zero to infinity. Other definitions for the aspect ratio, e.g. by deviation from equant source area taking the relationship of minimum to maximum dimension, are possible as well. The differences in dispersal can also be evaluated in terms of total column mass loadings. For all cases, higher total column mass loadings are found closer to the source location and at times closer to the eruption start. Between the model runs with different source areas, small changes in total column mass loadings towards the tip of the ash cloud are noticeable. However, these are only identified within the first $\sim 7\,\mathrm{h}$, and at later times differences become indistinguishable. In general, even when changing the source area by three orders of magnitude, only small differences in downwind cloud shape and column mass loading are observed. This is true for the full range of aspect ratios tested and the supporting plots for $\alpha_{mid} = 0.95$ and $\alpha_{max} = 1.7$ are shown in Figure A.1 and Figure A.2.

2.3.2 Impact of the aspect ratio of the source, α

To evaluate the impact of changing the aspect ratio of the source, α, we present the results from model runs for α_{min} and α_{max} at a common source area. Simulated total column mass loadings are shown in Figure 2.8 for $A_{max} = 619\,\mathrm{km}^2$. There are only very small differences in the shape of the modelled cloud. After $7\,\mathrm{h}$ since t_0, the tip of the ash cloud appears thinner for $\alpha_{max} = 1.7$ (Figure 2.8e), compared to $\alpha_{min} = 0.2$ (Figure 2.8a). The percentage overlap in the cloud area ranges from 83% to 90%. We consider these differences to be small given the order of magnitude change in source aspect ratio (0.2 vs. 1.7). Similar results are shown when comparing α_{min} and α_{max} for $A_{min} = 0.4\,\mathrm{km}^2$ and the related plots are shown in Figure A.3. Here, the percentage overlap in the cloud areas is greater, and ranges from 98% to 92% from $7\,\mathrm{h}$ to $23\,\mathrm{h}$ since t_0, thus slightly decreasing with time during this period. Figure 2.7b compares the overlap in ash cloud area between the minimum (α_{min}) and maximum (α_{max}) aspect ratio. In general, the greater overlaps

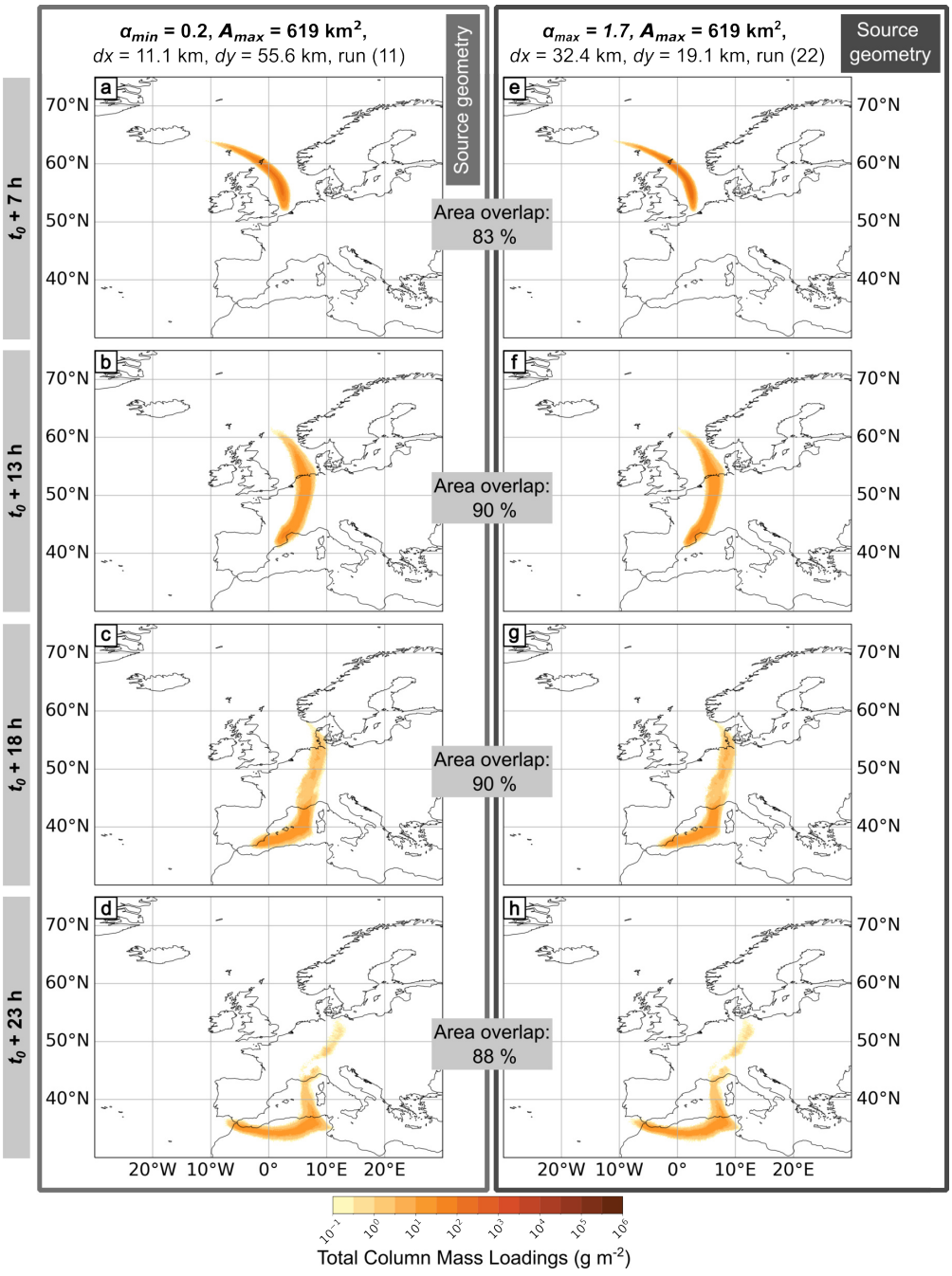

Figure 2.8: NAME model outputs for numerical experiment 1, all using $A_{max} = 619\,\mathrm{km}^2$, a $1\,\mathrm{h}$ particle release, $z = 8.5\,\mathrm{km}$, $dz = 3\,\mathrm{km}$ and $1.06 \times 10^{13}\,\mathrm{g\,h^{-1}}$. The left figure panels **(a-d)** show results from the minimum aspect ratio $\alpha_{min} = 0.2$, and the right panels **(e-h)** show the maximum aspect ratio $\alpha_{max} = 1.7$. The area and orientation of the two source geometries are compared in relation to each other next to the parameter list at the top of the figure. For each aspect ratio, four outputs at different times after eruption start t_0 are shown: **(a & e)** $7\,\mathrm{h}$, **(b & f)** $13\,\mathrm{h}$, **(c & g)** $18\,\mathrm{h}$, and **(d & h)** $23\,\mathrm{h}$. Total column mass loadings are averaged over the previous hour, and we applied a threshold of $0.2\,\mathrm{g\,m^{-2}}$.

correspond to the model runs with smaller source areas. Small source areas ($A < 5\,\mathrm{km}^2$) have large overlap ($> 95\%$) until $4\,\mathrm{h}$ after t_0 and slowly decreases with increased time after. However, at $24\,\mathrm{h}$ since t_0 the overlap is still $> 90\%$. For the other source areas, $A \geq 5\,\mathrm{km}^2$, the overlap increases until (at least) $8\,\mathrm{h}$, plateaus around 90% and then slightly decreases. The largest source area tested, $A_{max} = 619\,\mathrm{km}^2$, has the lowest overlap overall and is 51% at $1\,\mathrm{h}$ since t_0 and 88% at $24\,\mathrm{h}$ since t_0 (Figure 2.7b).

2.3.3 Evaluation of geometric source properties (A and α) on co-PDC ash dispersion

We now synthesise the results of the previous sections, comparing the impact of source area and aspect ratio, respectively. To supplement the visual comparisons between the NAME model outputs (cf. Figure 2.6 and Figure 2.8), we introduce the use of the relative standard deviation, %RSD:

$$\%\mathrm{RSD} = \frac{\sigma}{\bar{x}} \cdot 100 \tag{2.10}$$

where σ is the standard deviation of the data set under study (e.g., cloud area at each hour after eruption start for all cloud areas) and $\bar{x}$ is the average of the data set (i.e., the ash cloud area generated using experiment 1 per given modelled time).

Due to the $\sim 10\,\mathrm{km}$ horizontal resolution of the meteorological data used with our NAME simulations, source areas approximately $A \geq 10\,\mathrm{km}^2$ can have, in at least one dimension, a source geometry that is larger than the grid resolution and therefore crosses multiple meteorological grid cells. However, despite this, the total ash mass in the atmosphere (Figure 2.9) is remarkably similar for all runs in experiment 1 (Table 2.3), and no neighbouring wind variation causes different sedimentation. This is illustrated in Figure 2.9, where each model run from experiment 1 is shown, but almost all overlap. The total mass in the atmosphere starts at a maximum after $1\,\mathrm{h}$ (the total time of particle emission) and then decays as sedimentation occurs and no more particles are released into the atmosphere. Across all model outputs of experiment 1, the maximal %RSD is 0.4%, thus we can say, the total mass in the atmosphere is not affected by changing source aspect ratio or areas.

Overall, like the total mass in the atmosphere, the total cloud area, A_c, shows minor variation across all the source areas and aspect ratios investigated (Figure 2.10). The only exception is at times close to the start of particle emission, t_0 and thus at plume locations close to the source. Comparing all experiment 1 runs (grey dotted line in Figure 2.10a &b), close to the start time ($1\,\mathrm{h}$ since t_0), the relative standard deviation is 33%. However, these high %RSD values rapidly reduce to 9.5% after $4\,\mathrm{h}$ since t_0 and reach a low plateau of $\sim 2\%$ after $13\,\mathrm{h}$. The total cloud area increases and shows little spread between the different applied aspect ratios (Figure 2.10a). Although all lines (1) to (33) are represented, they almost all overlap and are on top of each other. By further analysing the cloud area, A_c, for a set plume height (here, $H_T = 10\,\mathrm{km}$), the influence

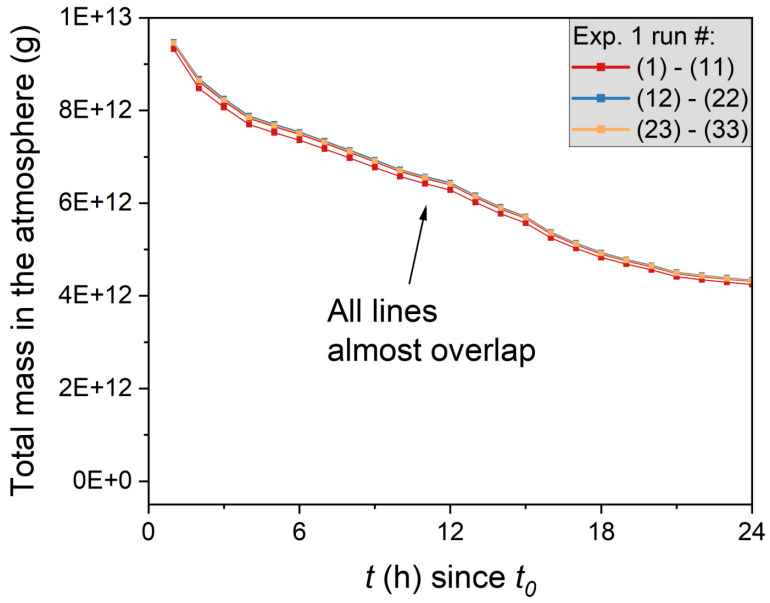

Figure 2.9: Total mass in atmosphere for all model runs in experiment 1. There are only very minor differences between model runs with different source areas and aspect ratios. The total mass in the atmosphere starts at a maximum after $1\,\mathrm{h}$ (the total time of particle emission) and then decays as sedimentation occurs and no more particles are released into the atmosphere. The lines between data points are not model fits and are just used to guide the eye.

of aspect ratio (Figure 2.10b) and area of the source geometry (Figure 2.10c) can be quantitatively investigated. Firstly, comparing different aspect ratios $\alpha_{min} = 0.2$ has a maximum %RSD of 41% and reduces to $<$ 10% after $6\,\mathrm{h}$, whereas $\alpha_{mid} = 0.95$ shows a maximum %RSD of 24% and becomes insignificant ($\leq$ 9%) after $3\,\mathrm{h}$, and $\alpha_{max} = 1.7$ shows a maximum %RSD of 19% and becomes insignificant ($\leq$ 6.5%) after $3\,\mathrm{h}$.

Furthermore, comparing the different source areas (each averaged over all three aspect ratios) used in experiment 1 (Figure 2.10c), we find that the larger the source area, the higher the %RSD. The %RSD decays with time for all source areas. $A_{max} = 619\,\mathrm{km}^2$ shows the largest %RSD of 33% at $1\,\mathrm{h}$ after article release, whereas $A = 1\,\mathrm{km}^2$ is only 1.8% of %RSD. Additionally, for a given time t, the %RSD is lower for smaller plume source areas. Only $A_{min} = 0.4\,\mathrm{km}^2$ and $A = 1\,\mathrm{km}^2$ do not exactly follow this observation until reaching $5\,\mathrm{h}$ since t_0, however, the %RSD is always $\leq$ 2%. For all source areas at $6\,\mathrm{h}$ since particle release, the %RSD is $<$ 10%.

For typical vent derived plumes (Mastin & Van Eaton, 2020) have shown that considering the associated umbrella cloud growth is crucial for the accurate model of the ash cloud area and downwind extent. They also show, as in this study that the difference between different cloud areas decreases with time after eruption. However, umbrella cloud areas typically range between

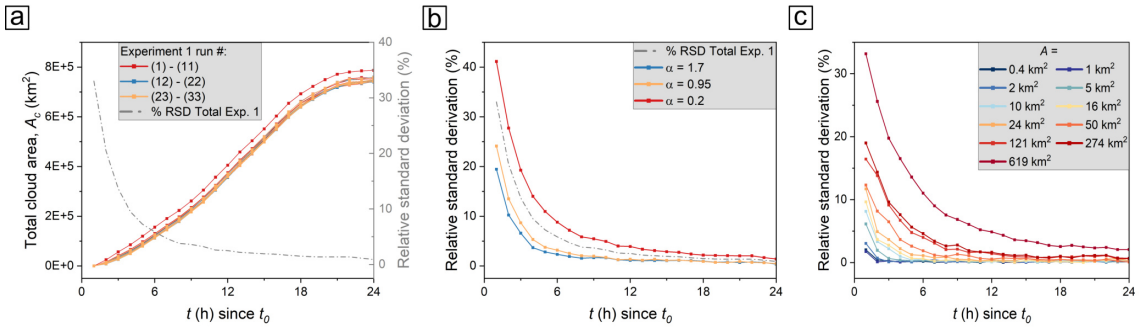

Figure 2.10: Total cloud area, A_c, for numerical experiment 1 results. **(a)** Experiment 1 has a small deviation within area and aspect ratio. The %RSD is indicated as a grey dotted line. It shows a higher impact by the source area for less than 4 hours of eruption time. **(b)** Experiment 1 separated per aspect ratio, taking all source areas into account. $\alpha_{min} = 0.2$ has a larger %RSD, as the longitudinal distance becomes more important with the specific applied weather conditions than for $\alpha_{mid} = 0.95$ or $\alpha_{max} = 1.7$. There is no linear relationship between %RSD and α. **(c)** Experiment 1 per area *A*, where one line represents three runs each ($\alpha_{min} = 0.2$, $\alpha_{mid} = 0.95$ and $\alpha_{max} = 1.7$). The larger the area, the larger the %RSD. In all panels, the lines between data points are not model fits and are just used to guide the eye.

$53.2\,\mathrm{km}^2$ and $1\,600\,000\,\mathrm{km}^2$ (Constantinescu et al., 2021; Mastin & Van Eaton, 2020; F. Prata et al., 2025; Zidikheri et al., 2017) and thus are larger than typical co-PDC clouds (e.g., $0.4\,\mathrm{km}^2$ to $619\,\mathrm{km}^2$). This further supports our observations that small co-PDC cloud dispersal (across the range of meteorological conditions applied here) is not impacted by the source area.

2.3.4 The impact of co-PDC plume H_T and MER

The modelled ash cloud shows completely different transport and dispersion patterns when changing H_T, and thus MER and *dz*. To illustrate this, in Figure 2.11 we show NAME simulations initialised using a range of plume heights (H_T) for $A_{max} = 619\,\mathrm{km}^2$ with $\alpha_{min} = 0.2$ at $12\,\mathrm{h}$ (left side of figure) and $23\,\mathrm{h}$ since t_0 (right side of figure). In general, modelled total column mass loadings increase with H_T and the larger H_T and MER are, the larger the ash cloud becomes. For $H_T = 1\,\mathrm{km}$ (Figure 2.11a & f), the total column mass loading threshold of $0.2\,\mathrm{g\,m}^{-2}$ is not reached. The cloud generated by $H_T = 5\,\mathrm{km}$ has mass loadings $\geq 0.2\,\mathrm{g\,m}^{-2}$ at $12\,\mathrm{h}$ (Figure 2.11b) and $23\,\mathrm{h}$ since t_0 (Figure 2.11g) but beyond $23\,\mathrm{h}$ mass loadings are relatively low. The ash clouds generated by $H_T = 20\,\mathrm{km}$ (Figure 2.11d) and $H_T = 27\,\mathrm{km}$ (Figure 2.11e) form a relatively compact area at $12\,\mathrm{h}$ after particle release, however they become more elongated and stretched over wider areas for $23\,\mathrm{h}$ (Figure 2.11i & j). For consistency, a set of model runs using $A_{max} = 619\,\mathrm{km}^2$ with $\alpha_{max} = 1.7$ and $A_{min} = 0.4\,\mathrm{km}^2$ with $\alpha_{min} = 0.2$ and $\alpha_{max} = 1.7$ are shown in supplementary Figure A.4 to Figure A.6. These bracket the extremes in natural parameter space and still follow the general relationships described here. As shown in Figure 2.12, all ash cloud areas increase with

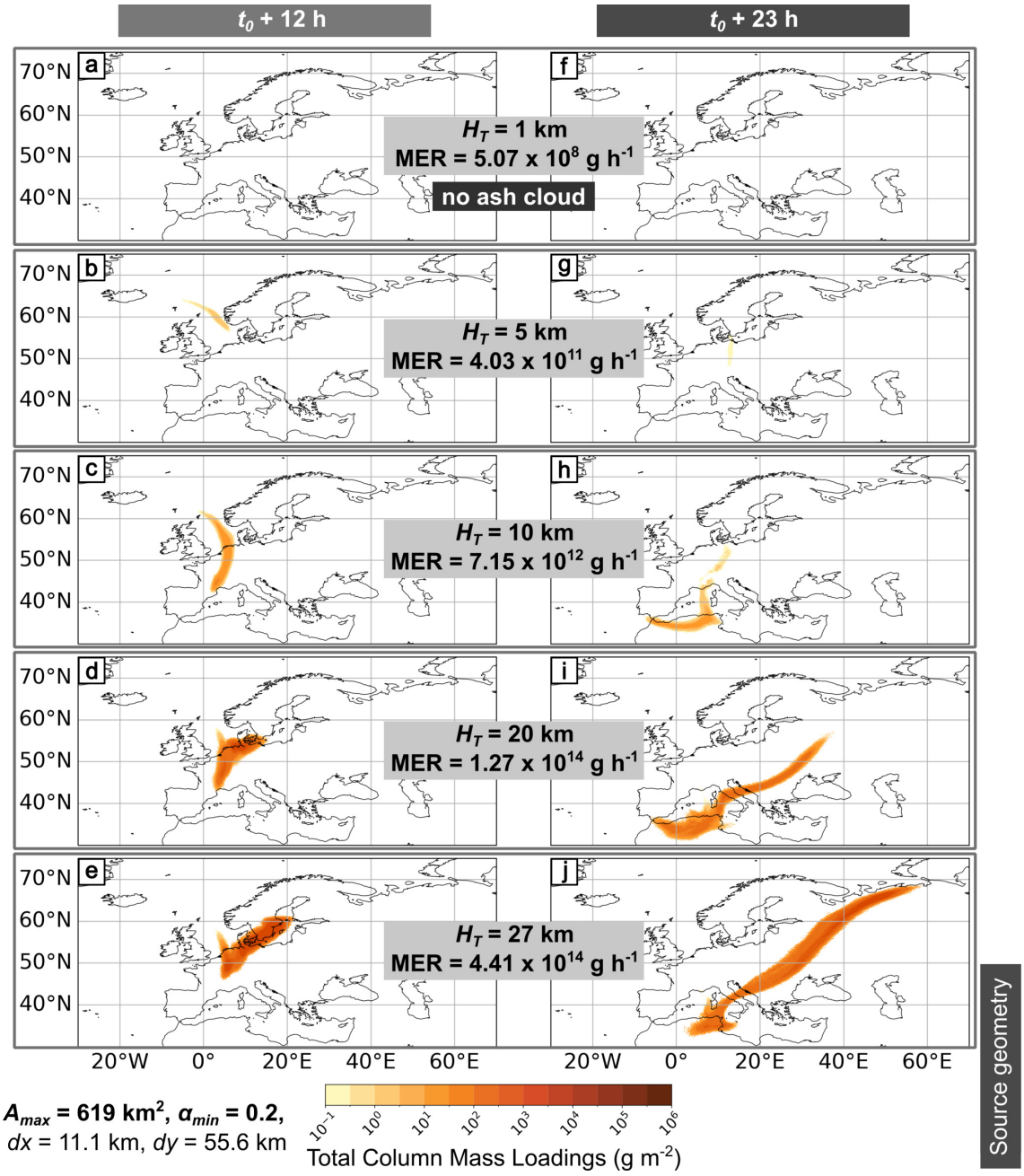

Figure 2.11: NAME model outputs for numerical experiment 2, all using a $1\,\mathrm{h}$ particle release with different H_T, MER, and *dz*. The figure panels on the left **(a-d)** are for $12\,\mathrm{h}$ after eruption start t_0, and the panels on the right **(e-h)** show $23\,\mathrm{h}$ after particle release. The outputs here are for $A_{max} = 619\,\mathrm{km}^2$ with $\alpha_{min} = 0.2$. With increasing H_T and *t* (h), the plume size grows. Total column mass loadings are averaged over the previous hour, and we applied a threshold of $0.2\,\mathrm{g\,m^{-2}}$. The subplots **(a & f)** show no ash cloud (i.e., mass loading $< 0.2\,\mathrm{g\,m^{-2}}$).

time after the beginning of particle emission (t_0) and larger initial plume heights (H_T), thus larger mass eruption rates, correspond to larger cloud areas.

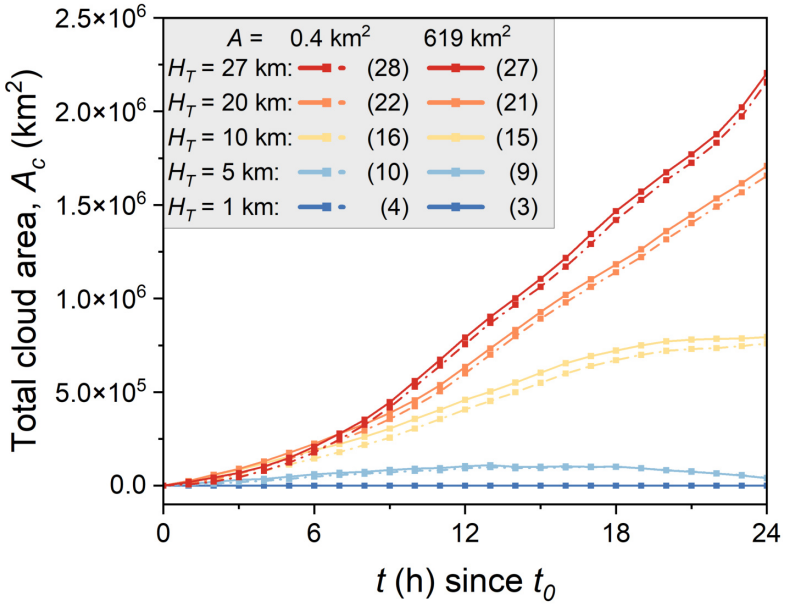

Figure 2.12: The total cloud area as a function of time for model runs within numerical experiment 2. The five different colours correspond to the different plume heights. Each with $A_{min} = 0.4\,\mathrm{km}^2$ for $\alpha_{max} = 1.7$ and $A_{max} = 619\,\mathrm{km}^2$ for $\alpha_{min} = 0.2$ as a dotted and solid line, respectively. The total plume area, A_c, increases for all plume heights with time within the first $13\,\mathrm{h}$. $H_T = 1\,\mathrm{km}$ and $H_T = 5\,\mathrm{km}$ decay afterwards, while the others continue to increase. The numbers in brackets correspond to the model run number. The lines between data points are not model fits and are just used to guide the eye.

Figure 2.13 shows the total modelled mass in the atmosphere with time. As expected, with increasing plume height (and thus MER), the total mass in the atmosphere (and the total column mass loadings in Figure 2.11) also increases. The total mass starts at a maximum (for each plume height) after $1\,\mathrm{h}$, which is the end of the emission time. Large plume heights ($H_T = 10\,\mathrm{km}$, $H_T = 20\,\mathrm{km}$ and $H_T = 27\,\mathrm{km}$) are almost constant, slightly decreasing, while $H_T = 1\,\mathrm{km}$ and $H_T = 5\,\mathrm{km}$ show a larger reduction/decay with time. $H_T = 1\,\mathrm{km}$ decreases its total mass to 0.004% of the initial total mass at $24\,\mathrm{h}$ since t_0. $H_T = 27\,\mathrm{km}$ is 68% of the initial total mass after $24\,\mathrm{h}$.

2.4 Outlook and future work

NAME models long-range transport and dispersion of ash clouds, and the complex behaviour of near-source eruption processes (i.e., rising eruption column) is not fully captured. In this study, we have represented the release of ash into the atmosphere with a set of eruption source parameters.

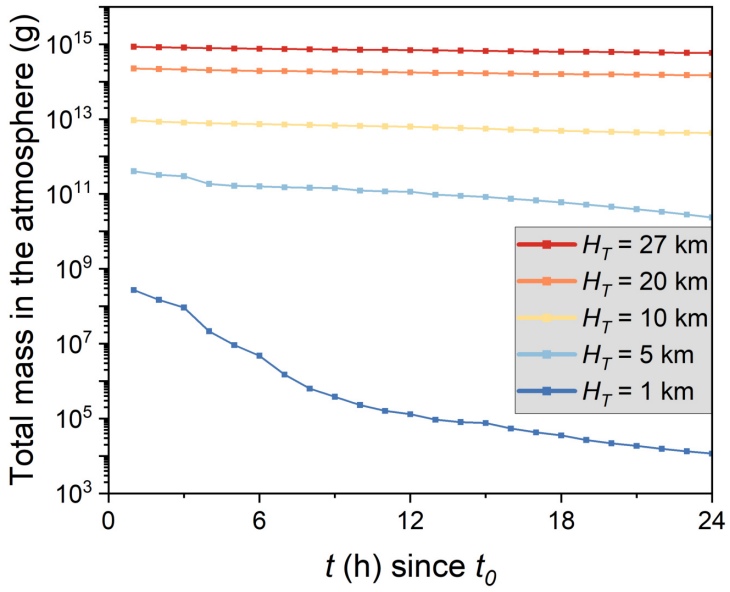

Figure 2.13: Total mass in atmosphere per plume height, H_T, in numerical experiment 2. For visual clarity, only $A_{max} = 619\,\mathrm{km}^2$, $\alpha_{min} = 0.2$ is shown here, but the other runs show a similar relationship. For all plume heights, the total mass in the atmosphere is greatest at $1\,\mathrm{h}$ since t_0 (end of particle emission) and decays afterwards. The smaller H_T, the greater the decay. The lines between data points are not model fits and are just used to guide the eye.

However, additional schemes can be coupled to NAME to represent vent proximal behaviour, including those for buoyant plumes and umbrella clouds (Beckett et al., 2015; Devenish, 2013; Webster et al., 2012, 2020). At the expense of increased computational time, these schemes could be applied to investigate the dynamics of co-PDCs and, when coupled to NAME, their impact on the long-range transport of the resulting ash cloud.

We have assumed a particle/ash emission duration of $1\,\mathrm{h}$. This aligns with the resolution of the averaging period used for the modelled total column mass loadings. It is expected that co-PDC plumes will have a range of ash emission times corresponding to eruption parameters such as the MER and source area; however, no quantitative relationships currently exist. The emission time also becomes important if the emitted volume/mass of particles needs to be quantified to a higher accuracy. To test the sensitivity of our model outputs to the particle emission/release time, we re-ran all our model configurations with a $24\,\mathrm{h}$ particle release, the results of which can be seen in the supplementary information (Figure A.7 to Figure A.15). The key results outlined in this contribution show no difference when using this longer emission time ($24\,\mathrm{h}$ vs $1\,\mathrm{h}$). Only the total cloud area and total column mass loadings vary in their absolute magnitude.

Our model runs used an emission start time of 31$^{\mathrm{st}}$ of January 2022, 09:00 UTC, at which

time there were westerly winds, representative of the prevailing conditions in this area. Our results suggest that long-range transport and dispersion model simulations of ash clouds are insensitive to varying emission source areas and aspect ratios, within the range of end-members identified for co-PDC plumes. We would only expect there to be sensitivity if the meteorological conditions varied significantly across the area of the source, and for most meteorological scenarios, we would not expect large step changes in conditions across areas typical of co-PDCs. There could be exceptions though, for example, the moment when there is a passage of a weather front. The sensitivity is also dependent on the resolution of the NWP and its ability to represent any variation. Here we have used NWP data from the Global configuration of the UM, which has a horizontal resolution of $\sim 10\,\mathrm{km}$, which has been shown to be optimal for representing long-range transport of ash clouds (see Beckett et al. (2020)). Typically, approximately five grid lengths are required to represent variation in meteorological parameters (Abdalla et al., 2013; Lean & Clark, 2003). In our study, the maximum co-PDC source area we considered corresponds to 5 (*dy*) by 3 (*dx*) grid lengths for $\alpha_{min} = 0.2$ and 2 (*dy*) by 7 (*dx*) grid lengths for $\alpha_{max} = 1.7$. Therefore, for the scenarios modelled here, it is only the A_{max}, $\alpha_{max} = 1.7$ output that might be impacted by specific metrological variations in the source area. However, as NWP resolutions increase and grid lengths shorten the impact of metrological variations within the source area, this will need to be re-evaluated. Additionally, further investigations are required to determine the impact of different seasons and climatic changes.

Here, we used a single TGSD documented for the Campanian co-ignimbrite eruption (Marti et al., 2016). Due to their formation, through self-segregating buoyant lift-off, co-PDCs have a narrow and uniform TGSD relative to vent-derived ash plumes/clouds. It has also been shown that the grain-size distribution of co-PDCs does not vary substantially with distance (Engwell & Eychenne, 2016; Eychenne et al., 2015). This imposes aggregation as being present within the column and as they fell (Bonadonna, Mayberry, et al., 2002; Eychenne et al., 2012; Watanabe et al., 1999). However, given that it is known that particle size distribution has significant impact on the dispersion and transport of ash particles in the atmosphere (Beckett et al., 2015), future studies may investigate the impact of the TGSD on co-PDC ash cloud dispersal.

The applied relationship between H_T and MER has been well investigated for point sources; however, it is not clear how well this applies for elongated source geometries. Unknown, so far, is how the source area and MER are impacted by entrainment of ambient air, changing the particle concentration across the plume for these elongated source geometries. We assume entrainment to be lower along the edges of a linear plume than along the edges of a circular plume. It remains to be investigated whether large areas, i.e., $A_{max} = 619\,\mathrm{km}^2$, are still likely to reach a plume height of $H_T = 30\,\mathrm{km}$ with the same MER predicted by the power law relationship derived from vent-derived plume information (Aubry et al., 2023) and whether the assumption of uniform MER over the whole source area is suitable. Although the MSH's co-PDC plume falls within the confidence interval of the MER relationship used here, smaller co-PDC plumes might be better described by a different plume scheme, e.g., a thermal buoyant plume, with an instantaneous mass release, meaning that

the MER-H_T relationship would be different (Biass et al., 2016; Bonadonna, Macedonio, & Sparks, 2002; Druitt et al., 2002; Woods & Kienle, 1994).

2.5 Conclusion

We studied the transport and dispersion of a volcanic ash cloud generated from a co-PDC plume to assess the sensitivity to the eruption source parameters used to initialise model simulations. Co-PDC ash plumes/clouds, generated from PDCs, have unique source properties, in particular their particle size distribution and source geometry are different to typical eruption plumes. Our sensitivity study showed that changes in the source area and the aspect ratio of the source have only a minor impact on the resultant cloud location and its total column mass loadings. Our findings in early hours since t_0 and close to the particle/ash release describe the impact as the greatest if the long axis of the source geometry is perpendicular to the wind direction. However, the plume height and corresponding mass eruption rate yield significant differences in the ash dispersion results and are thus key parameters for appropriately modelling transport and dispersion of co-PDC ash clouds.

3. The ash concentration of co-PDC clouds

3.1 Introduction

Ground-hugging gravity currents, termed pyroclastic density currents (PDCs), can be formed by the collapse of an eruption column (R. J. Brown & Andrews, 2015; Burgisser et al., 2024; Dellino et al., 2021; Druitt, 1998; Dufek et al., 2015; Giordano & Cas, 2021; T. J. Jones et al., 2023; Lube et al., 2020) or from collapse of lava domes or flow fronts (Bonadonna, Mayberry, et al., 2002; Calder et al., 1997; Charbonnier & Gertisser, 2008; Michol et al., 2008; Sigurdsson & Carey, 1989; Sulpizio et al., 2010; Ui et al., 1999). The mixtures are multiphase and comprise both hot gas and solid particles, e.g., volcanic ash, lithic fragments. Accompanying plumes, commonly termed co-PDCs, but also known as phoenix clouds or co-ignimbrites (Andrews & Manga, 2011; Bursik & Woods, 1996; Engwell & Eychenne, 2016; T. J. Jones et al., 2024; Pistolesi et al., 2025; Rosi et al., 2006; Sigurdsson & Carey, 1989; Sparks et al., 1997), can form from these PDCs by air entrainment and buoyant lift-off of the upper portions of the flow (Andrews & Manga, 2011, 2012; Engwell & Eychenne, 2016; Engwell et al., 2016; Sparks et al., 1997; Woods & Wohletz, 1991). Therefore, co-PDCs are composed of hot gas and fine particles (the heavier particles remain in the denser ground-hugging current). The co-PDC plumes rise until they reach a level of neutral buoyancy in the atmosphere and then disperse laterally. Given these formation conditions, co-PDCs have some unique eruption source parameters (ESPs), for example, co-PDCs have been found to have a smaller particle size ($< 90\,\mu\mathrm{m}$) (Engwell & Eychenne, 2016; Sigurdsson & Carey, 1989) and have a high-aspect ratio source geometry (i.e., irregular shaped, not circular).

Volcanic ash can have a significant impact on infrastructure, human health, livestock, soil fertility and crops (T. M. Wilson et al., 2015). It also represents a significant hazard to aviation (Alexander, 2013; Casadevall, 1993; Casadevall et al., 1999; Folch et al., 2012; Guffanti et al., 2011; Lechner et al., 2018; Miller & Casadevall, 1999; Pardini et al., 2024; F. Prata & Rose, 2015; Webster et al., 2012; Witham et al., 2012), with a key example being the 2010 Eyjafjallajökull eruption, which dispersed ash over Europe, leading to a $\sim$ US$ 2 billion loss for the aviation industry (F. Prata & Rose, 2015). Small volcanic particles can reach high altitudes, travel long distances,

and disperse over wide areas (Pardini et al., 2024; Saxby et al., 2018). Therefore, aircraft are not only exposed to risk from volcanic ash close to the eruptive source, but many 100's kilometres downwind. High ash concentrations can lead to aircraft damage, as ash entering the engines may be heated to above their glass transition temperatures (Kueppers et al., 2014), and create engine disturbance by clogging air bleed holes or sticking to surfaces (Casadevall, 1993; Casadevall et al., 1999; Christmann et al., 2017; F. Prata & Rose, 2015). This can lead to malfunction of electronic components (e.g., speed indicators, pressure sensors, engine power, and cause interference with communication and navigation systems), or pressure losses (Christmann et al., 2017). Ash also has abrasive effects, especially on the leading edges, fan blades, or on the windshields, and this damage may only be visible after long-term exposure (Bernard & Rose, 1990; Casadevall, 1993; Casadevall et al., 1999; Chen & Zhao, 2015; Christmann et al., 2017; F. Prata & Rose, 2015).

Volcanic Ash Advisory Centres (VAAC) are responsible for providing ash hazard information to civil aviation. For the aviation industry to mitigate against the ash hazard and retain flight safety, they need to know the location of the ash cloud in the atmosphere and its ash concentration. VAACs currently communicate this hazard through the issuance of volcanic ash advisories (Engwell et al., 2021), but starting from November 2025, VAACs will begin to issue Quantitative Volcanic Ash (QVA) information. QVA forecasts contain ranges and thresholds of ash concentration. 'Low' concentrations are defined as ash concentrations within 0.2-$2\,\mathrm{mg\,m^{-3}}$. 'Medium' concentration is 2-$5\,\mathrm{mg\,m^{-3}}$ and 'high' ash concentration groups into 5-$10\,\mathrm{mg\,m^{-3}}$, while ash concentrations of $10\,\mathrm{mg\,m^{-3}}$ or higher are classified as 'very high' (ICAO Meteorology panel, 2023). The minimum satellite detection threshold of ash particles is approximately $0.2\,\mathrm{g\,m^{-2}}$ total column mass loading, depending on different retrieval schemes, and a lower limit of approximately 0.1-$0.2\,\mathrm{mg\,m^{-3}}$ has been set for concentration (ICAO, 2012; ICAO Meteorology panel, 2023; A. J. Prata & Prata, 2012; F. Prata & Rose, 2015). This nicely links to the lower bound of the QVA threshold range, when distributing this total column mass loading over an ash cloud of $1\,\mathrm{km}$ thickness (Clarkson et al., 2016; A. J. Prata & Prata, 2012).

Clarkson et al. (2016) and F. Prata and Rose (2015) stress and highlight, referring to the 'Safe to Fly' chart developed by Rolls-Royce in 2010, the relationship between ash concentration and exposure time to the safety of operation and long-term damage. The chart can only be considered as a guideline, as different turbine engine types, conditions, and ash types might impact the boundaries and regions of the chart. A review by Clarkson et al. (2016) suggests ash concentrations below $0.1\,\mathrm{mg\,m^{-3}}$ to be safe to engines.

Commercial flights follow a set of well-defined flight phases: taxi, take-off, en-route (climb, cruise, and descent), approach, and landing (Goblet et al., 2015). These aircraft typically fly at a cruising altitude just below the tropopause (F. Prata & Rose, 2015) between 8.8-$12.5\,\mathrm{km}$ (Fichter et al., 2005). The International Civil Aviation Organisation (ICAO) has standard regulations on flight levels (abbreviated as FL) to provide adequate vertical separation between aircraft and sufficient terrain clearance to prevent any collisions (ICAO, 1956). FLs are parallel surface levels of constant

atmospheric pressure, with reference to a pressure datum, FL 0, which is $1013.2\,\mathrm{hPa}$ (1013.2 millibars) and equivalent to mean sea level. The reference atmospheric pressure of $1013.2\,\mathrm{hPa}$ is defined by the 'ICAO Standard Atmosphere' (ICAO, 1956, 1993) and the International Standard Atmosphere (ISA), which is an atmospheric model describing how air density, temperature, and pressure change with altitude. The relationship between flight level, atmospheric pressure, and weather is shown schematically in Figure 3.1. Meteorological conditions impact the altitude (above

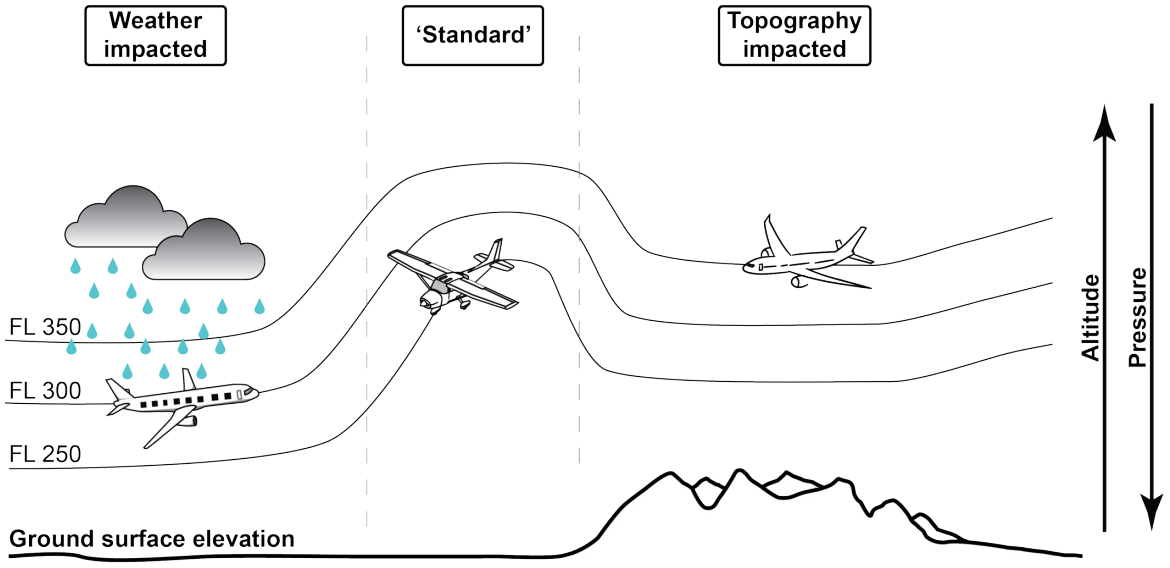

Figure 3.1: Flight levels (FL) retain vertical separation despite atmospheric pressure variations due to different weather conditions and large changes in ground topography. The 'standard' region shown in the middle of the figure is shown as a reference. Despite the cruise flight level being fixed (e.g., FL 300), the aircraft changes its actual altitude (i.e., km above sea level) during flight.

sea level) of the flight levels, for example, precipitation, often caused by a depression, lowers the atmospheric pressure and therefore the altitude of the corresponding FL. Similarly, the atmospheric pressure can be impacted by changes in the topography. A plane's altimeter specifies the current flight altitude, and the altimeter scale corresponds to a particular barometric pressure at a certain location and time (ICAO, 1956). During take-off, landing, and below a certain transition altitude (a specific altitude above a minimum distance from the ground or aerodrome (ICAO, 1956)), commonly at $457\,\mathrm{m}$ ($1500\,\mathrm{ft}$), planes set their altimeter to the current air pressure of the airport or the applied location (QNH altimeter). However, at higher altitudes (above the specific transition altitude and/or when in cruise flight), a standard reference set of 'flight levels' is used, and flying heights are measured based on pressure. This ensures that every plane uses the same reference for altitude determination for consistency. Planes do not fly at a constant altitude above the ground but rather follow an assigned flight level. For this reason, volcanic ash concentrations in the atmosphere are commonly reported per FL, and forecast model outputs for each are generated.

The UK Met Office's Numerical Atmospheric-dispersion Modelling Environment, NAME, models particle transport and dispersion in the atmosphere by releasing a large number of model particles into a model environment. Simulations are then driven using pre-processed global atmospheric conditions from the Met Office's Unified Model (UM) (Beckett et al., 2020; Davies et al., 2005), a type of Numerical Weather Prediction model (NWP). NAME is also used by the London Volcanic Ash Advisory Centre (VAAC) as its operational model for volcanic ash forecasts. This contribution uses NAME, and we output NAME results by FL for altimeter as FL is the scale also requested by QVA for aviation. Figure 3.2 shows the vertical resolution of the wind vector (ρ) and temperature (θ) data of the meteorological UM compared to the FL ranges for a standard atmosphere. The vertical resolution of both the wind and temperature data reduces with height, respectively. For altitudes corresponding to where commercial planes fly (at standard atmospheric pressure: FL290 to FL410 approximately (Fichter et al., 2005)) and the maximum FL requested by QVA (at standard atmospheric pressure: FL600), at least two ρ and θ datasets are available for each FL (at standard pressure). Whereas at altitudes $>\approx 25\,\mathrm{km}$ asl these meteorological datasets (ρ and θ) have a vertical spacing greater than one FL, and as such, meteorological data availability is limited.

A few studies have modelled co-PDC rise and dispersion (Chapter 2, Bursik and Woods (1996), Calder et al. (1997), Engwell et al. (2016), Herzog and Graf (2010), Neri et al. (2002, 2003), Sparks et al. (1997), Woods and Kienle (1994), and Woods and Wohletz (1991)). Chapter 2 used NAME to study the unique eruption source parameters (ESPs) associated with co-PDCs and the sensitivity of co-PDC plume transport and dispersion models to these ESPs, in terms of their horizontal cloud footprint, where here the term 'cloud' is used to refer to downwind ash transport and dispersion, while 'plume' describes solely the near-source behaviour. The cloud spread, ash cloud area, and the simulated total column mass loadings were analysed (in $\mathrm{g\,m^{-2}}$). The impact of the ESPs, specifically varying plume heights and coupled mass eruption rates, has been determined (Chapter 2). However, little is known about the vertical concentration of ash in dispersing co-PDC cloud (in $\mathrm{mg\,m^{-3}}$) - which is the important measurement for aviation. While numerous publications discuss the vertical distribution of ash in vent-derived plumes (e.g. Andrews (2014), Andrews and Manga (2011, 2012), Dioguardi et al. (2020), and Oberhuber et al. (1998)), no such studies specifically focus on co-PDC plumes. Furthermore, given the unique ESPs of co-PDCs, limited direct insight can be gained from our knowledge of vent-derived plumes. Here, we aim to bridge this gap by performing a series of NAME model runs for co-PDC ash dispersion and transport and analysing the resultant atmospheric ash concentrations in the vertical (i.e., at different FLs). This allows us to discuss whether the concentration of a co-PDC ash cloud could potentially have a meaningful impact on aviation.

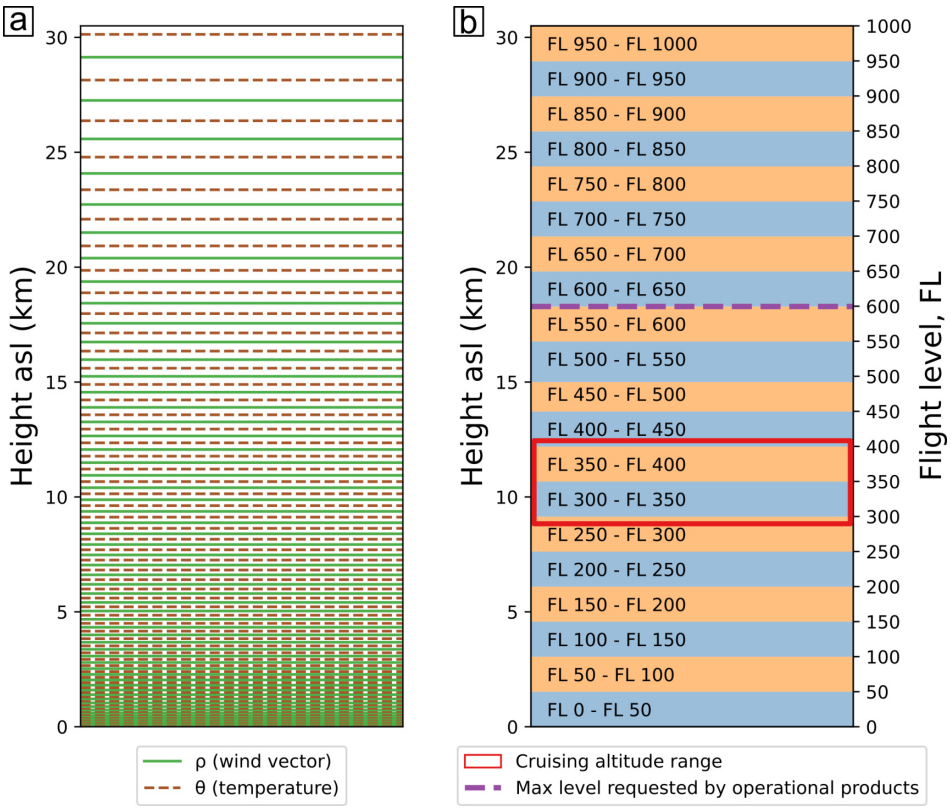

Figure 3.2: The vertical resolution of the Met Office Unified Model(MetUM) compared with flight level, FL. **(a)** 'ρ' and 'θ' levels contain the wind vector data and the temperature data, respectively. The vertical resolution of both data sets decreases with increasing height above sea level (asl). **(b)** NAME outputs FL in steps of 50. Despite FL being pressure-based, the standard atmosphere pressure curve is used for comparison ($1013.2\,\mathrm{hPa} \equiv$ FL0, which has a linear relationship). The purple dashed line indicates the maximum FL (FL600) requested by aviation for QVA analysis.

3.2 Methods

3.2.1 Modelling and NAME setup

NAME can be used to predict atmospheric transport, dispersion, and deposition of gases and particles (A. Jones et al., 2007). It uses the advection-diffusion equation and gives the concentration of particles as an output. Here, NAME, specifically version NAME III v8.5 (Beckett et al., 2020; A. Jones et al., 2007), was used in the Lagrangian configuration to model the ash transport and dispersion of a volcanic ash cloud derived from a co-PDC plume. For all NAME runs, we applied the wet and dry deposition schemes within NAME (Dacre et al., 2011; Harvey et al., 2018; Webster et al., 2012; Webster & Thomson, 2011) and assumed time homogeneity of the ESPs, where all the input parameters did not vary with time. This is an idealisation for modelling purposes, although we are aware that PDCs and co-PDCs are not constant in time (e.g., MSH 1980 (Mastin, Carey,

et al., 2022; Sparks et al., 1986) and Calbuco 2015 (Van Eaton et al., 2016)).

We used the pressure-as-height coordinate system to relate the height, z_{ICAO}, to the ICAO standard atmosphere pressure. Adapted from NAME (A. Jones et al., 2007) this is expressed as:

$$z_{ICAO} = \begin{cases} \dfrac{T_{msl}}{\gamma_{0-11}} \left(1 - \left(\dfrac{p}{p_{msl}} \right)^{\frac{R\gamma_{0-11}}{g}} \right) & \text{for} \quad p \geq p_{11} \\ z_{11} + \dfrac{RT_{11}}{g} \ln \left(\dfrac{p_{11}}{p} \right) & \text{for} \quad p_{11} > p > p_{20} \\ z_{20} + \dfrac{T_{20}}{\gamma_{20+}} \left(1 - \left(\dfrac{p}{p_{20}} \right)^{\frac{R\gamma_{20+}}{g}} \right) & \text{for} \quad p \leq p_{20} \end{cases} \tag{3.1}$$

with

$$p_{11} = p_{msl} \left(1 - \frac{\gamma_{0-11}}{T_{msl}} z_{11} \right)^{\frac{g}{R\gamma}} \tag{3.2}$$

$$p_{20} = p_{11} \exp \left(-\frac{g}{RT_{11}} (z_{20} - z_{11}) \right) \tag{3.3}$$

where R is the specific gas constant for dry air, $R = 287.05\,\mathrm{J\,kg^{-1}\,K^{-1}}$; T_{msl} is the temperature at mean sea level, $T_{msl} = 288.15\,\mathrm{K}$; T_{11} is the temperature at $11\,\mathrm{km}$ asl, $T_{11} = 216.65\,\mathrm{K}$; T_{20} is the temperature at $20\,\mathrm{km}$ asl, $T_{20} = 216.65\,\mathrm{K}$; γ_{0-11} is the lapse rate from 0-11 km asl, $\gamma_{0-11} = 0.0065\,\mathrm{K\,m^{-1}}$ and γ_{20+} is the lapse rate at altitudes greater than $20\,\mathrm{km}$ asl, $\gamma_{20+} = -0.001\,\mathrm{K\,m^{-1}}$. As in the ICAO standard atmosphere, the lapse rate is assumed to be constant between specified altitudes (Meteorological Office, 1991). p_{msl} is the standard pressure at mean sea level, $p_{msl} = 101\,325\,\mathrm{Pa}$; z_{11} stands for the altitude of $11\,\mathrm{km}$ above mean seal level, when using the hydrostatic assumption; p_{11} corresponds to the pressure at z_{11}.

A meteorological data archive is used, where the meteorological data are interpolated (when using the Lagrangian approach) in time and space (Webster et al., 2012). For the eruption setup, we used a pre-processed, configured NWP dataset from the Global configuration of the Met Office Unified Model (MetUM) (Beckett et al., 2020; A. Brown et al., 2012; Davies et al., 2005; Walters et al., 2019). The meteorology definition applied here was the Met Office's *UMG_Mk10PT*, which spans the dates between June 1st, 2007 and May 2nd, 2022 and has the highest from the available NAME MetUM global horizontal resolution with grid lengths of approximately $10\,\mathrm{km}$ at mid-latitudes. The vertical resolution varies with height and decreases towards higher elevation, see Figure 3.2a). The vertical ash concentration in NAME was output over vertical depths of 5000 feet (approximately $1500\,\mathrm{m}$), which corresponds to a depth of 50 FL (determined with standard atmospheric pressure). The relationship between FL and altitude in metres is thus determined, as illustrated in Figure 3.2.

Weather patterns group characteristic recurring circulation types, i.e. similar weather occurrences over a defined region. The prevalent weather pattern over the specific region can vary daily. Neal

et al. (2016) defined a set of eight weather patterns for the North Atlantic and European (NAE) region, including the UK area (30°W – 20°E and 35° – 70°N), which are used for seasonal and long-range forecasts and for identifying key changes in wind flow (Neal et al., 2016). These eight weather patterns, illustrated in Figure 3.3, show the location of positive Mean Sea Level Pressure (MSLP) and negative MSLP over the UK. Weather patterns are numbered in order of the annual historical occurrence between 1850 and 2003. The lower numbers indicate that the weather pattern occurs more frequently, i.e., over the whole year, weather pattern 1 occurs more often than weather pattern 8. For full descriptions of each weather pattern and percentage of occurrence, the reader is referred to Neal et al. (2016).

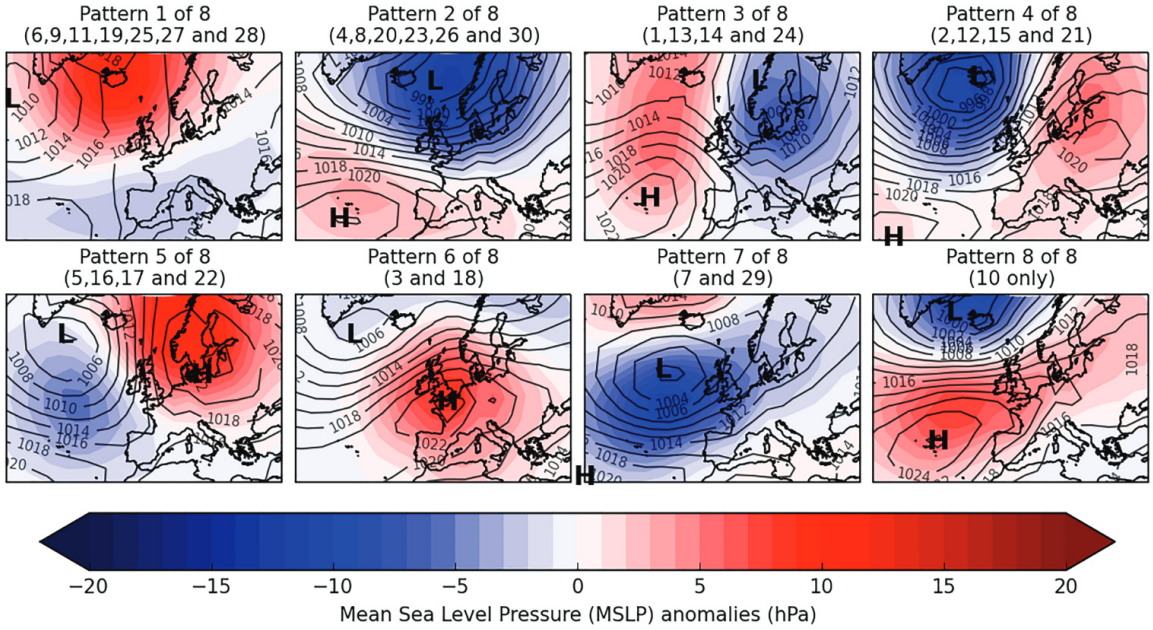

Figure 3.3: An overview of the eight weather patterns. A set of 30 sub-patterns used for medium-range and variation examination is grouped into their specific weather pattern. These sets are indicated in brackets at the top of each subplot. The Mean Sea Level Pressure (MSLP) is given as coloured contours in 2 hPa intervals, and the Mean Sea Level Pressure anomalies are represented by the colour bar. Figure taken from Neal et al. (2016).

We use this set of weather patterns, one to eight, to consider the impact of meteorology on our results. We do not perform a climatology study, but use these weather patterns to better underpin and confirm that our findings are not exclusively based on one sampled day, i.e., one particular weather pattern. Out of each weather pattern within *UMG_Mk10PT*, three days from different seasons are manually selected and used for model runs. In total, we performed model runs across 24 days (Figure 3.4 and Table B.1), and the distribution of these days is presented in Figure 3.4.

Each of these 24 days has been run for particle emission start times of 06:00 UTC, 14:00 UTC and 22:00 UTC for a duration of $36\,\mathrm{h}$ (288 runs in total). Additionally, for 31$^{\mathrm{st}}$ January 2022, we also ran at a fourth time of 09:00 UTC in order to compare with the previous co-PDC study in

Chapter 2. The different start times were chosen by considering the diurnal cycle, which refers to a daily cycle of environmental conditions (i.e., weather changes and temperature fluctuation), and the atmospheric boundary layer (i.e., the layer between the planetary surface and free atmosphere), which depends on the temperature of the ground. The lowest temperature occurs close to sunrise, between 6-7 am, while the maximum occurs at 2-3 pm (Dai, 2023; Dang et al., 2019). The difference between the extremes is about $\sim 8\,\mathrm{h}$, this justifies our $8\,\mathrm{h}$ spacing in run start times.

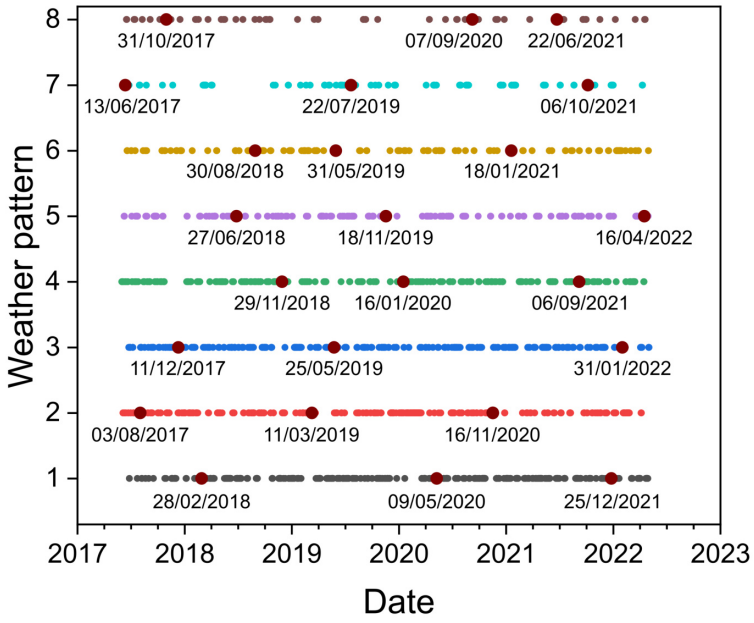

Figure 3.4: Visualisation of the selected days for our NAME runs. The dataset range of *UMG_Mk10PT* is indicated per weather pattern and is shown by small symbols in different colours. Datasets highlighted in dark red circles are used in this study with their dates given in the format day/month/year.

3.2.2 Eruption conditions

This study used a $10\,\mathrm{min}$-particle release or emission time, t_r, which corresponds to observations of some large co-PDC plumes (Sparks et al., 1986). The model was initialised at the level of neutral buoyancy, z, where particles were released into the atmosphere over a defined thickness, *dz*. This thickness of the release around z is given by the ratio of the total column height, H_T, defined as (Bonadonna & Phillips, 2003; Carey & Sparks, 1986; Morton et al., 1956; Sparks, 1986):

$$dz = 0.3 \cdot H_T \tag{3.4}$$

Here, we approximate *dz* as ranging from $0.7 \cdot H_T$ to H_T while neglecting any overshoot top. The May 18th 1980 eruption of Mount St. Helens, USA, (MSH in the following) is the largest observed and well-documented co-PDC in literature. Therefore, in this work, we use parameter values (i.e., *A*, α, *dx*, *dy*, t_r; refer to Table 3.1) related to this eruption. As it represents one of the largest co-PDC plumes, any reported ash concentrations and cloud footprints represent a reasonable upper limit. Exceeding these parameters, although possible, is rarely observed in nature and such events might be governed by different physical processes. Chapter 2 showed that the particle release height significantly affects the horizontal ash cloud transport, whereas the effects of source area and source aspect ratio are negligible. Following this study, we now consider the vertical downwind concentrations of volcanic ash from a co-PDC release and its sensitivity to plume height and MER. NAME was therefore run with constant source input parameters, as defined in Table 3.1. The particles were assumed to be spherical with the total grain size distribution (TGSD) as in Chapter 2 modified from Marti et al. (2016). The Campanian Ignimbrite TGSD is relatively fine compared to vent-derived deposits. We applied the entire TGSD and no distal fine ash fraction as the entire distribution is relatively fine (i.e., 86% $< 105\,\mu\mathrm{m}$). Hekla volcano in Iceland (63.98°N, 19.67°W (Global Volcanism Program, 2024)) was used as the source location; however, the source location is not unique for our study, as we are not studying local topographic influences or volcano properties. Rather, we selected Hekla for its distance of $51\,\mathrm{km}$ to the Atlantic Ocean, so that the entire source area of the co-PDC remained on land, as a co-PDC has a relatively large source area away from the vent (as opposed to modelling a vent-derived plume). The computational grid in NAME has a horizontal grid resolution of 0.1° in Lat and Long, and throughout the model domain, the vertical grid resolution decreases with vertical height, see Figure 3.2.

Table 3.1: Co-PDC source parameters used in this study. *A*, α, *dx*, *dy*, *P* and t_r refer to the May 18th 1980 eruption of MSH (Chapter 2). See Chapter 2 for references to H_T and *dz*. t_r has been taken from Sparks et al. (1986).

Parameter	Symbol	Unit	Value(s)
Release Area	A	km^2	619
Aspect ratio	α		1.7
Width of source in plan view	dx	km	32.4
Length of source in plan view	dy	km	19.1
Source perimeter	P	km	103.0
Maximum plume height	H_T	km	15, 20, 25 & 27
Thickness of ash release	dz	km	4.5, 6.0, 7.5 & 8.1
Particle release time	t_r	min	10
Particle density	ρ	$\mathrm{kg\,m^{-3}}$	2500

The total height of co-PDC plumes, H_T, has been observed in nature in the range of 1-30 km (Chapter 2). Traditionally, H_T is coupled to the mass eruption rate, MER, by an empirical power law (Aubry et al., 2023; Mastin et al., 2009; Morton et al., 1956; Sparks, 1986; L. Wilson et al.,

1978). Here, we use the MER-H_T-relationship from Aubry et al. (2023):

$$\text{MER} = \sqrt[0.226]{\frac{H_T}{0.345}} \tag{3.5}$$

The MSH plume height and mass eruption rate fall within the confidence interval of this relationship in Equation 3.5. It is therefore assumed to be applicable here, for our modelled co-PDC plumes, and used in the absence of any other specific physical relationship for co-PDCs. Data for very small co-PDC observations are not included in this relationship. As MSH represents the largest observed co-PDC plume described in literature, we limit our modelled range of plume heights to $15\,\mathrm{km}$, $20\,\mathrm{km}$, $25\,\mathrm{km}$, and $27\,\mathrm{km}$.

The aspect ratio of the particle release area/source is set as a constant parameter describing the relationship of the source area's width by length (dx/dy) to be 1.7 (see Table 3.1 and Chapter 2).

3.2.3 Numerical Experiment

The volcanic ash cloud was simulated for $36\,\mathrm{h}$ with data output every $1\,\mathrm{h}$. The particles were released at the start of the simulation for $t_r = 10\,\mathrm{min}$. Table 3.2 defines all parameters and their variation for our set of model runs, or 'numerical experiment'. This set of runs analysed the impact of the release height of co-PDC particles, i.e., $H_T = 15\,\mathrm{km}$, $H_T = 20\,\mathrm{km}$, $H_T = 25\,\mathrm{km}$ and $H_T = 27\,\mathrm{km}$; labelled with **(a)**, **(b)**, **(c)** and **(d)** in Table 3.2, respectively, and release time, i.e., 06:00 UTC, 14:00 UTC and 22:00 UTC, labelled as **(06)**, **(14)** and **(22)**, respectively, on the ash cloud location, size, and shape per FL. The release heights define dz and MER, determined by using Equation 3.4 and Equation 3.5, respectively. We used a particle density of $2500\,\mathrm{kg\,m^{-3}}$ and assumed no particle aggregation. Particle aggregation (often for particle diameters $< 63\,\mu\mathrm{m}$ (R. J. Brown et al., 2012)) describes the adhesive clustering of individual particles due to moisture or electrostatic forces (R. J. Brown et al., 2012; Engwell & Eychenne, 2016; Watanabe et al., 1999). Aggregates show an increased sedimentation rate and velocity, lower density and larger size distributions than the individual constituent particles (R. J. Brown et al., 2012; Durant & Brown, 2016). Given the fine TGSD and the presence of aggregates in preserved deposits, it is likely that particle aggregation is present in co-PDC columns (Bonadonna, Mayberry, et al., 2002; Engwell & Eychenne, 2016; Eychenne et al., 2012; Watanabe et al., 1999). Throughout all variations within the numerical experiment, all models were classified by the erupted volume as VEI 2 (Newhall & Self, 1982). Although our plume height is high, the released volume due to the short release time, t_r, is small and therefore the VEI remains small. All other eruption source parameters used in this study were kept constant, as defined in Table 3.1. The numerical experiment was then repeated for different weather patterns and dates, see Figure 3.4.

The model run with a plume height of $27\,\mathrm{km}$, corresponding to MER = $2.39 \times 10^8\,\mathrm{kg\,s^{-1}}$ (Aubry et al., 2023), and an eruption duration (corresponding to t_r) of $10\,\mathrm{min}$ for a total mass release of $1.43 \times 10^{11}\,\mathrm{kg}$ is consistent with published literature on MSH (i.e., total mass = $3.25 \times 10^{11}\,\mathrm{kg}$;

Table 3.2: Source parameters used in the numerical experiment. Four release heights were each used for three release times. The range of covered flight levels of the release region is indicated and rounded to the nearest ten. The cells highlighted in grey indicate the labels, in brackets, for the model runs.

Tot. plume height, H_T (km agl)	dz (km)	FL range of release region	MER ($\mathrm{kg\,s^{-1}}$)	Calculated released mass into atmosphere (kg)	Calculated released volume ($\mathrm{m^3}$)		Release time (UTC)		
							06:00	14:00	22:00
15	4.5	270 - 420	1.77×10^7	1.06×10^{10}	4.26×10^6	**(a)**	**(06)**	**(14)**	**(22)**
20	6.0	360 - 560	6.34×10^7	3.80×10^{10}	1.52×10^7	**(b)**			
25	7.5	450 - 670	1.70×10^8	1.02×10^{11}	4.08×10^7	**(c)**			
27	8.1	490 - 750	2.39×10^8	1.43×10^{11}	5.74×10^7	**(d)**			

Sparks et al. (1986)). This supports our selection of source parameters for our numerical experiment with a historically observed event.

3.3 Results

Here we show our results from the NAME model runs, defined in Table 3.2. We focus on the impacts on the dispersed downwind cloud in terms of its location, area, concentration (with reference to QVA), and vertical mass distribution. All these results are reported across a range of weather patterns, plume heights, and mass eruption rates (MERs).

Figure 3.5 provides an illustrative example of how concentrations at specific vertical intervals (i.e., at specific FLs) relate to commonly reported total column mass loadings. Where the total column mass loadings, shown in Figure 3.5a, are the total integrated mass down the whole vertical column, and have units $\mathrm{g\,m^{-2}}$. Figure 3.5b - l have units $\mathrm{mg\,m^{-3}}$ and represent the ash concentration within different altitude layers (i.e., at different flight levels). The maximum extent of the ash cloud with total column mass loadings $\geq 0.2\,\mathrm{g\,m^{-2}}$, constraining the total horizontal footprint, is given in each subplot as a light grey-shaded area. The regions of ash located within each FL vary in size, shape, location and ash concentration (Figure 3.5b - l). At the highest FLs, in this example, the cloud area is relatively small, whereas for the middle FLs (i.e., FL300 - FL500), the cloud is larger and typically more elongated in shape. The shape, area and concentration also depend on the time since particle release.

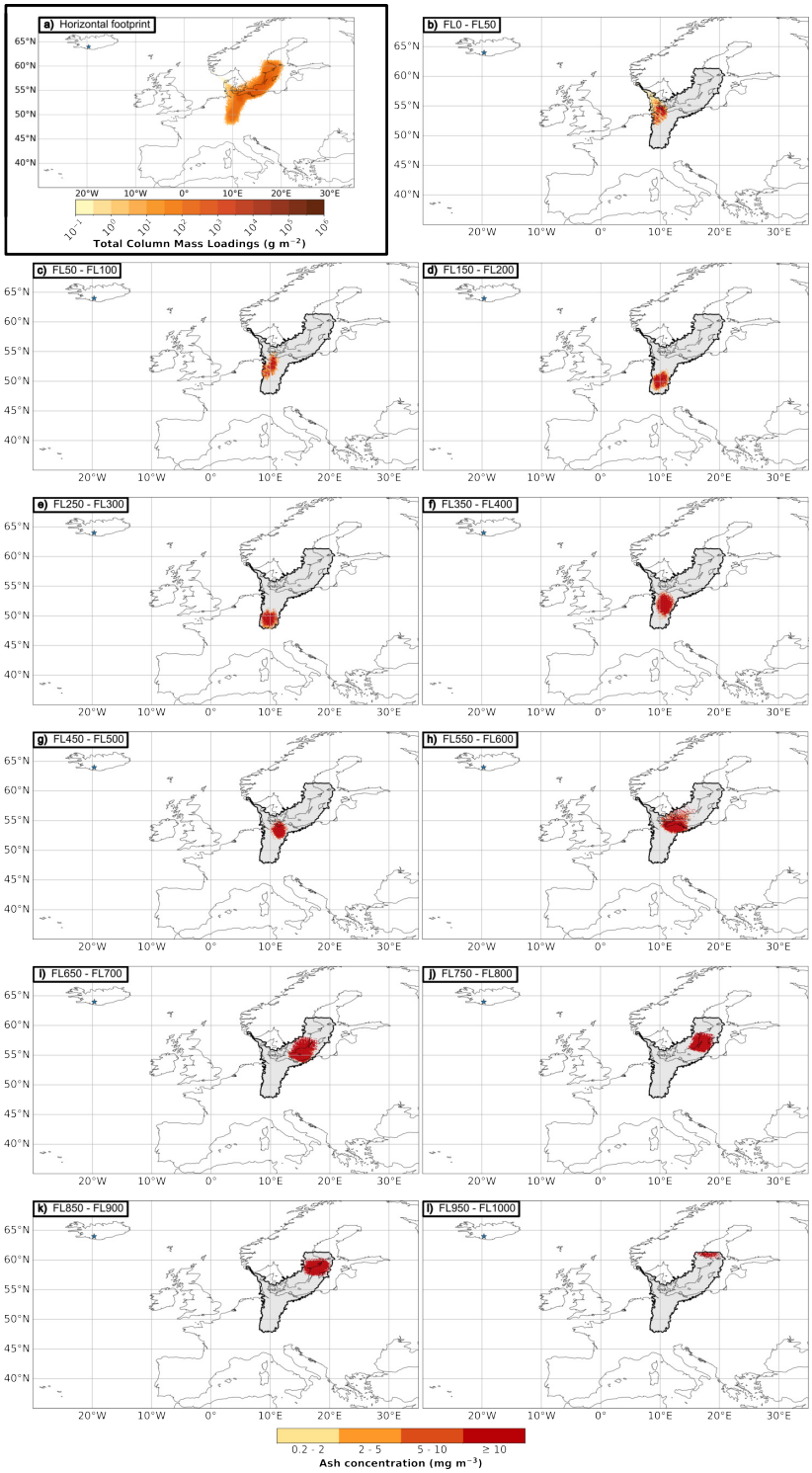

Figure 3.5: Illustration of the relationship between **(a)** the horizontal footprint of total column mass loadings ($\mathrm{g\,m^{-2}}$) and **(b-l)** the vertical output shown at selected flight levels (in $\mathrm{mg\,m^{-3}}$) at $12\,\mathrm{h}$ after the particle release. Particles were released at $H_T = 27\,\mathrm{km}$ on 31$^{\mathrm{st}}$ Jan 2022 at 14:00 UTC. In all panels, a blue star indicates the release location. Note the difference in the range and the units of the colour bars between the total column **(a)** and vertical outputs **(b - l)**. The black outline in **(b - l)** represents the boundary of total column mass loadings $\geq 0.2\,\mathrm{g\,m^{-2}}$.

3.3.1 Ash cloud location

We evaluate if the ash cloud location systemically varies between each weather pattern, see Figure 3.6. To do this, we focus on a common time after eruption start (t_0), a common vertical FL range and a common H_T. Here, we only display map figures for $12\,\mathrm{h}$ after particle release, at FL550 - FL600 for $H_T = 27\,\mathrm{km}$ to keep the number of figures to the minimum needed to support our results and interpretations. Our full dataset can be found in the supplementary information (Figure B.1 displays FL300 - FL350 and Figure B.2 displays FL900 - FL950). We have chosen to display $H_T = 27\,\mathrm{km}$ because the most (vertical) diversity was shown; however, the trends described in this section remain true for all the different flight levels.

Across all of the eight weather patterns that are typical for our modelled geographical region (Neal et al., 2016), we found that the ash clouds presented in Figure 3.6 (all at $12\,\mathrm{h}$ since particle release at FL550 - FL600) were remarkably discrete and isolated; they feature a highly concentrated region, with very minor lower concentration margins. Throughout the whole range of weather patterns at FL550 - FL600, QVA classification declares the ash concentration as 'very high', as seen by the dark red coloured ash clouds (ash concentration $\geq 10\,\mathrm{mg\,m^{-3}}$). Also, the cloud trajectories were mainly towards Europe for all runs and weather patterns. However, even within the same weather pattern at the same period of time after the particle release, the specific location of the ash cloud is highly variable, and both the cloud shape and size often show large variability. We will now describe these differences and similarities within each weather pattern.

The three dispersion outputs corresponding to weather pattern 1 (Figure 3.6a) are all located in different positions - there is no spatial overlap between the outputs. Two of the ash clouds are located relatively close to Iceland, while the other ash is elongated and stretched close to the north coasts of Scotland and Norway. For weather pattern 2 (Figure 3.6b), one cloud is highly elongated while the other two are more compact and remain closer to the source. Outputs for weather pattern 3 (Figure 3.6c) are widely spread in terms of location; however, they exhibit a similar plume shape. In general, all of the outputs for weather pattern 4 (Figure 3.6d) are elongated; however, like the outputs from weather pattern 3, they are widely spread in terms of location while considering the same point in time. Ash concentrations from weather patterns 5 and 6 (Figure 3.6e & f) both show two ash clouds located directly over the Icelandic land mass, while the third is located in the Arctic Ocean and the Atlantic Ocean, respectively. For weather patterns 7 and 8 (Figure 3.6g & h), the outputs illustrate that the ash clouds have not travelled far from the source within $12\,\mathrm{h}$.

Figure 3.7 compares the ash concentration (in $\mathrm{mg\,m^{-3}}$) for a specific flight level (here, FL300 - FL350, where commercial planes fly) within the same weather pattern (here, weather pattern number 3) for different release heights, H_T. The three different modelled days (11$^{\text{th}}$ December 2017, 25$^{\text{th}}$ May 2019 and 31$^{\text{st}}$ of January 2022) are plotted within each subfigure and are indicated by a black arrow and the corresponding dates. For a given day, the ash cloud locations are similar for all release heights ($H_T = 15\,\mathrm{km}$, $20\,\mathrm{km}$, $25\,\mathrm{km}$ and $27\,\mathrm{km}$), simply highlighting how the ash cloud dispersal is highly sensitive to the specific meteorological conditions. However, the cloud extent,

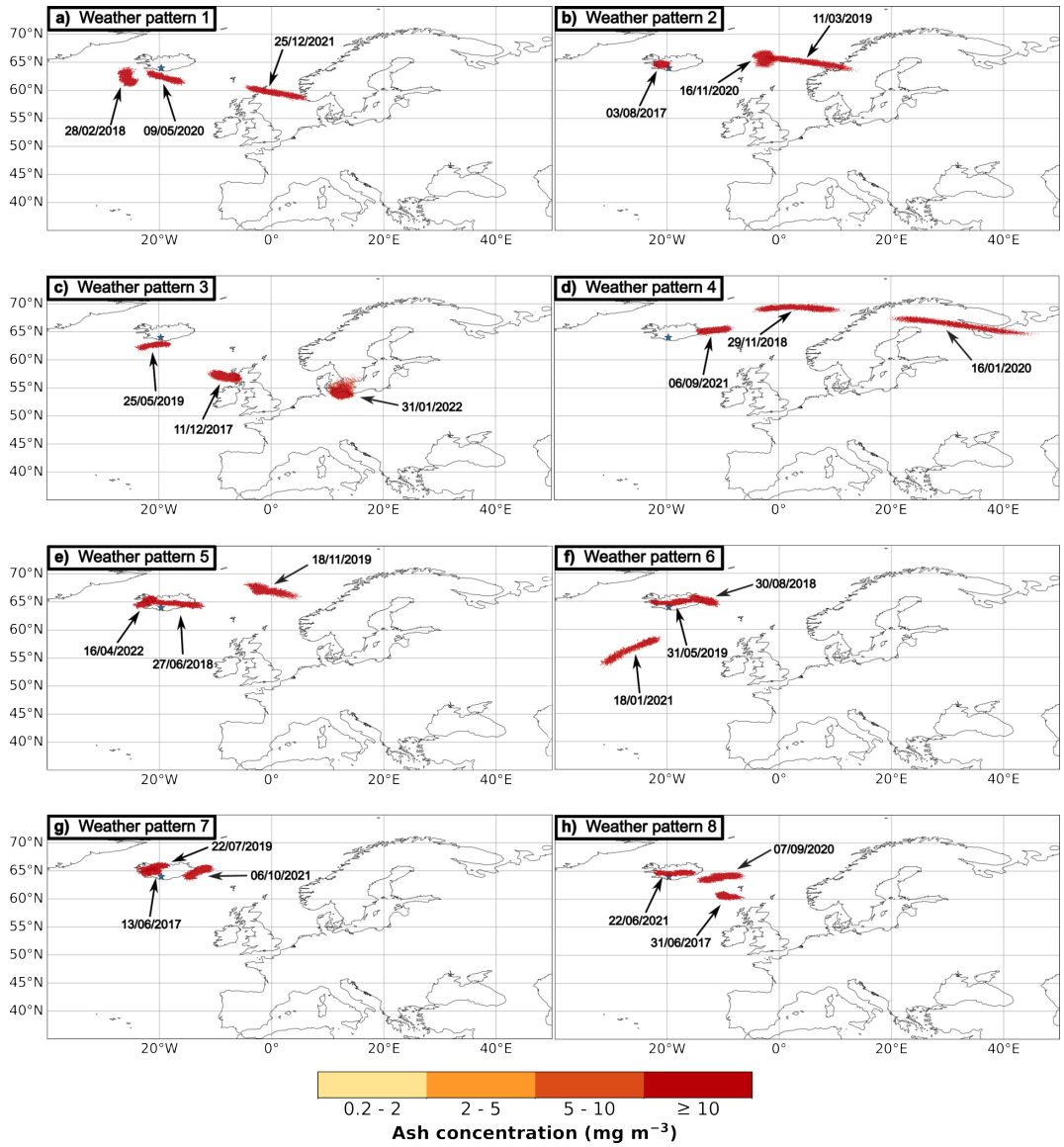

Figure 3.6: Ash cloud location displayed for the eight weather patterns at $12\,\mathrm{h}$ after particle released at $H_T = 27\,\mathrm{km}$ at 14:00 UTC. The range of FL550 - FL600 is displayed. Each subfigure contains three NAME model outputs, and thus displays three different ash clouds generated for each weather pattern. These are indicated by the black arrows, and the dates correspond to the associated eruption/release start. Some of the ash clouds within a weather pattern slightly overlap in this figure. In all panels, a blue star indicates the release location. The data are given as ash concentration in $\mathrm{mg\,m^{-3}}$.

ash concentration, and shape differ. Ash released at $H_T = 25\,\mathrm{km}$ and $H_T = 27\,\mathrm{km}$ (Figure 3.7c & d) show similar behaviour in terms of their location, size, concentration, and shape. $H_T = 15\,\mathrm{km}$ (Figure 3.7a) contains mainly low to medium ash concentrations (yellow and orange colours), whereas very high ash concentrations are present in both $H_T = 25\,\mathrm{km}$ and $H_T = 27\,\mathrm{km}$ (Figure 3.7c & d) (dark red, $\geq 10\,\mathrm{mg\,m^{-3}}$). The location of the ash cloud at the higher FLs (e.g., FL550

- FL600 and FL900 - FL950) does not change significantly when H_T is varied (Figure B.3 and Figure B.4, respectively). However, the ash cloud location within lower FLs is more sensitive to H_T (Figure 3.7).

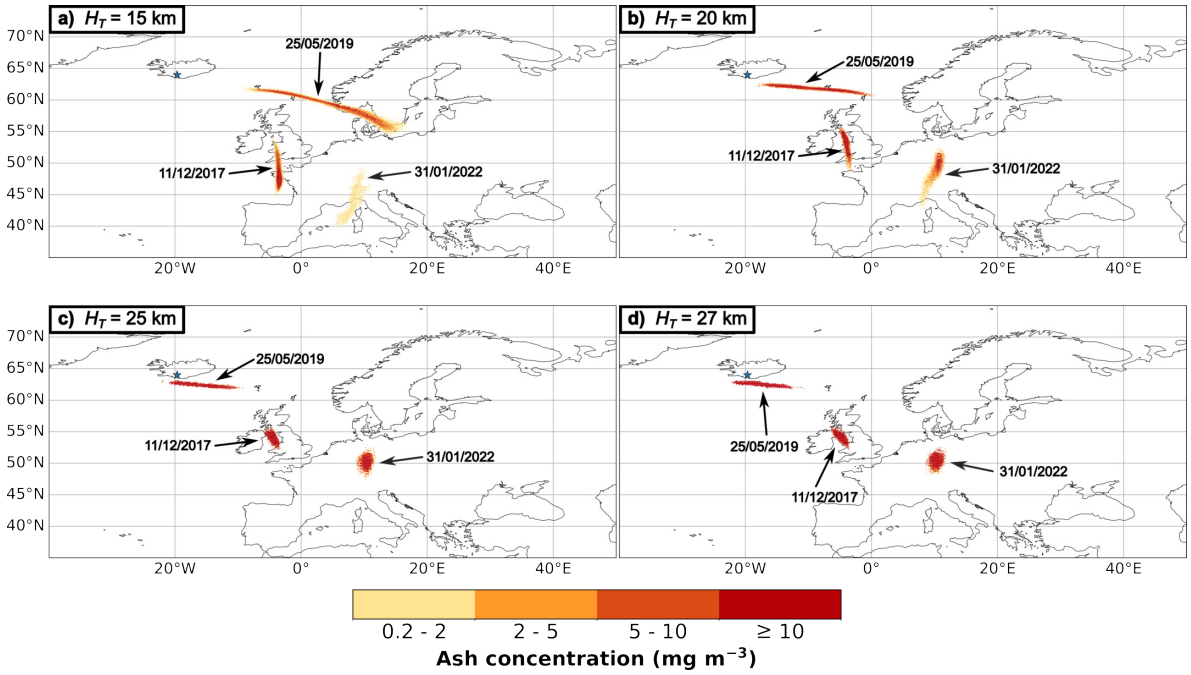

Figure 3.7: Ash cloud locations for particle release heights of **(a)** $H_T = 15\,\mathrm{km}$, **(b)** $H_T = 20\,\mathrm{km}$, **(c)** $H_T = 25\,\mathrm{km}$, and **(d)** $H_T = 27\,\mathrm{km}$ for the weather pattern number 3 at $12\,\mathrm{h}$ since start time. The particles were released on 31$^{\mathrm{st}}$ Jan 2022 at 14:00 UTC. Each subfigure shows three different model run outputs at FL300 - FL350 for different dates. In all panels, a blue star indicates the release location. The data are given as ash concentration in $\mathrm{mg\,m^{-3}}$.

3.3.2 Total ash cloud area per FL per time

The total area of the downwind ash cloud is reported as a function of time for each release height, H_T, see Figure 3.8. We chose the same date (31$^{\mathrm{st}}$ January 2022, 14:00 UTC) as was used to illustrate the ash cloud behaviour, i.e., Figure 3.5. For all values of H_T, divergence in total ash cloud area is observed with time. The areal extent of the cloud spreads noticeably from the time of release and shows little particle deposition, i.e., no large reductions in cloud area within the first $36\,\mathrm{h}$. Release height $H_T = 15\,\mathrm{km}$ (Figure 3.8a) generates an ash cloud reaching FLs up to approximately FL600; $H_T = 20\,\mathrm{km}$ generates a cloud up to FL800 (green coloured lines), while $H_T = 27\,\mathrm{km}$ covers the whole range investigated here, up to FL1000. $H_T = 25\,\mathrm{km}$ reaches up to FL950. Figure 3.8c and Figure 3.8d, corresponding to $H_T = 25\,\mathrm{km}$ and $H_T = 27\,\mathrm{km}$, respectively, show similar cloud area distributions across the different flight levels. Across all release heights, the range of FL250 - FL500, corresponding to the orange and yellow lines, is among the largest cloud areas for all time steps analysed. Although the absolute magnitude of these areas is generally

relatively small ($\sim 300\,000\,\mathrm{km}^2$), the altitude range they occupy corresponds to flight levels used for commercial aircraft (FL300 - FL400).

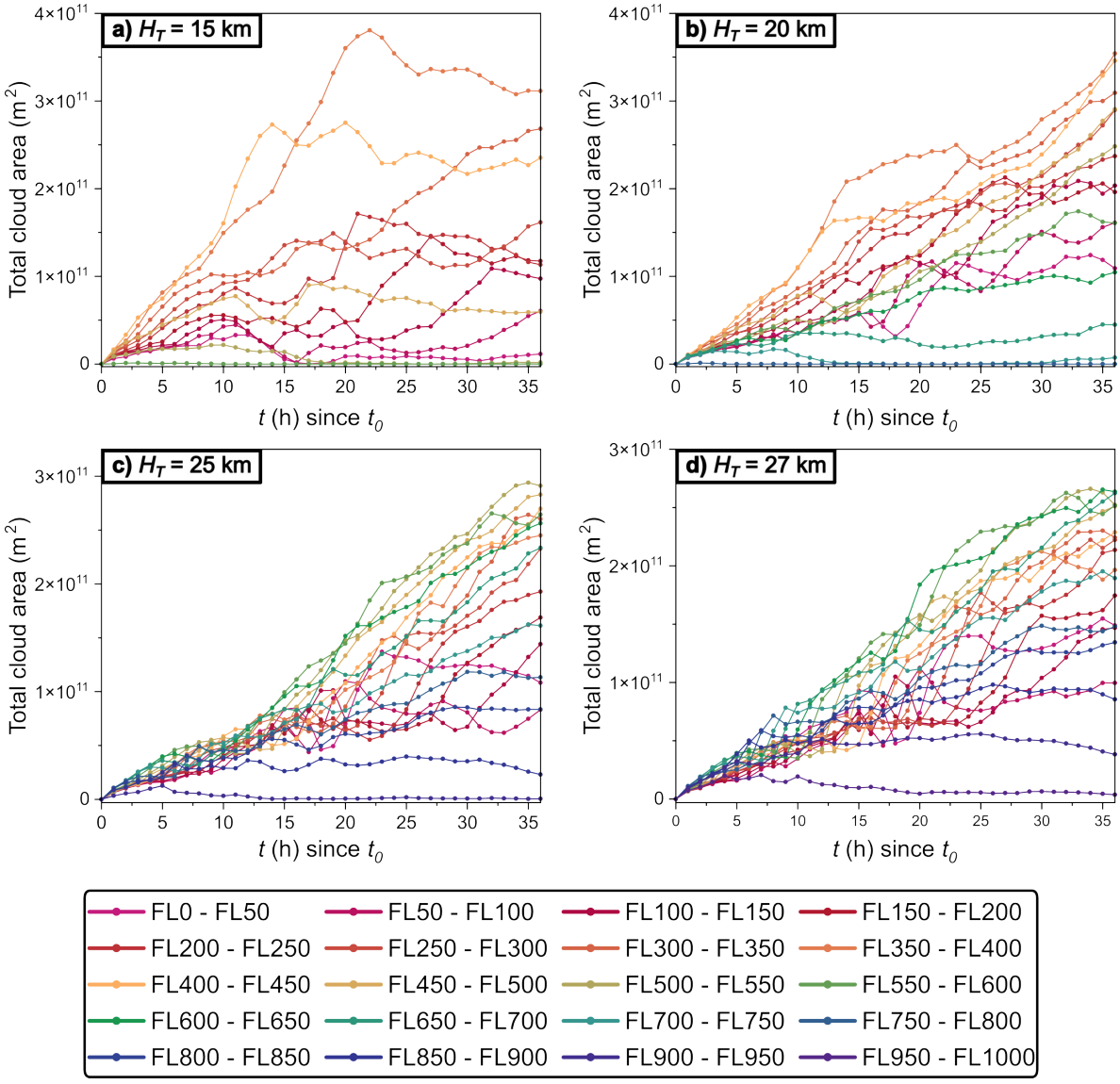

Figure 3.8: Total ash cloud area at each 50 FL as a function of time for particle release heights of **(a)** $H_T = 15\,\mathrm{km}$, **(b)** $H_T = 20\,\mathrm{km}$, **(c)** $H_T = 25\,\mathrm{km}$, and **(d)** $H_T = 27\,\mathrm{km}$. The displayed data originates from the same weather pattern (number three), day (31$^{\mathrm{st}}$ January 2022), and start time (14:00 UTC). The lines between data points are not model fits and are just used to guide the eye.

3.3.3 Vertical location of the maximum mass

It is also important for aviation to consider where the dispersed ash resides in terms of mass. Here, this is done by reporting the vertical location (i.e., flight level/height (asl)) where (i) the maximum

amount of ash is located and (ii) the highest FL that the ash reaches. The minimum height of the ash cloud is simply taken as ground level, as ash settles from the cloud. In Figure 3.9, this is shown as a function of time, for all four H_Ts investigated and for all start times across all weather patterns. The green line indicates the average maximum FL achieved by particles. For all start times across all weather patterns, the maximum achieved FL is always situated above the release region (orange box in Figure 3.9) by approximately 50 to 150 FLs, while small variations in time are likely to originate from vertical atmospheric turbulences. The light grey line indicates the average location of the maximum amount of mass, which decreases with time but remains, at least for the first $36\,\mathrm{h}$, in the original release region. The 95% confidence interval (black dotted lines) of these data set shows that there is very little variation in these results for different days and start times.

We note that the computational domain of NAME in the vertical direction in our experiments is restricted to $30\,\mathrm{km}$ (approximately corresponding to FL1000). The maximum FL achieved in Figure 3.9d reaches the top of the computational domain and it is therefore possible that some particles may be able to reach higher altitudes and thus our representation of the maximum FL achieved for $H_T = 27\,\mathrm{km}$ might be an underestimate.

3.4 Discussion

3.4.1 The influence of weather pattern and release height

Our NAME simulations show how co-PDC clouds are transported and dispersed across a wide range of weather patterns, and how ash concentrations vary in space and time. Our results and findings are a consequence of the unique ESPs for co-PDCs, and here, we discuss our results in the context of the aviation hazard. During operational response to real events, known generalisations can be useful. For example, it is beneficial to know which parameters impact the results the most, and therefore must be described accurately, for an optimal forecast, which must be generated quickly. Our model runs utilised the eight different weather patterns valid for the UK and surrounding Europe (Neal et al., 2016). We found that the shape, size, or location characteristics of ash clouds cannot be related to a specific weather pattern. Even if the weather pattern is known, we also cannot predict the vertical cloud location (i.e., at a specific flight level). For a given weather pattern, the distance travelled by the ash cloud (up to $12\,\mathrm{h}$) can also vary significantly. The only generalisation that can be made is that weather patterns 5 to 8 (Figure 3.6e-h) show less dispersed ash clouds, and remain closer to the source location over Iceland, relative to weather patterns 1 to 4 (Figure 3.6a-d). This means that, based on our current knowledge, robust statements and generalisations about how the location, area or shape of an ash cloud from a co-PDC varies as a function of the weather pattern cannot be made. A model simulation using the specific weather data for the time of the event is needed to obtain the specific characteristics of the ash shape, size, or location for a given day. Future work should compare our findings with the whole set of 30 weather patterns defined by Neal

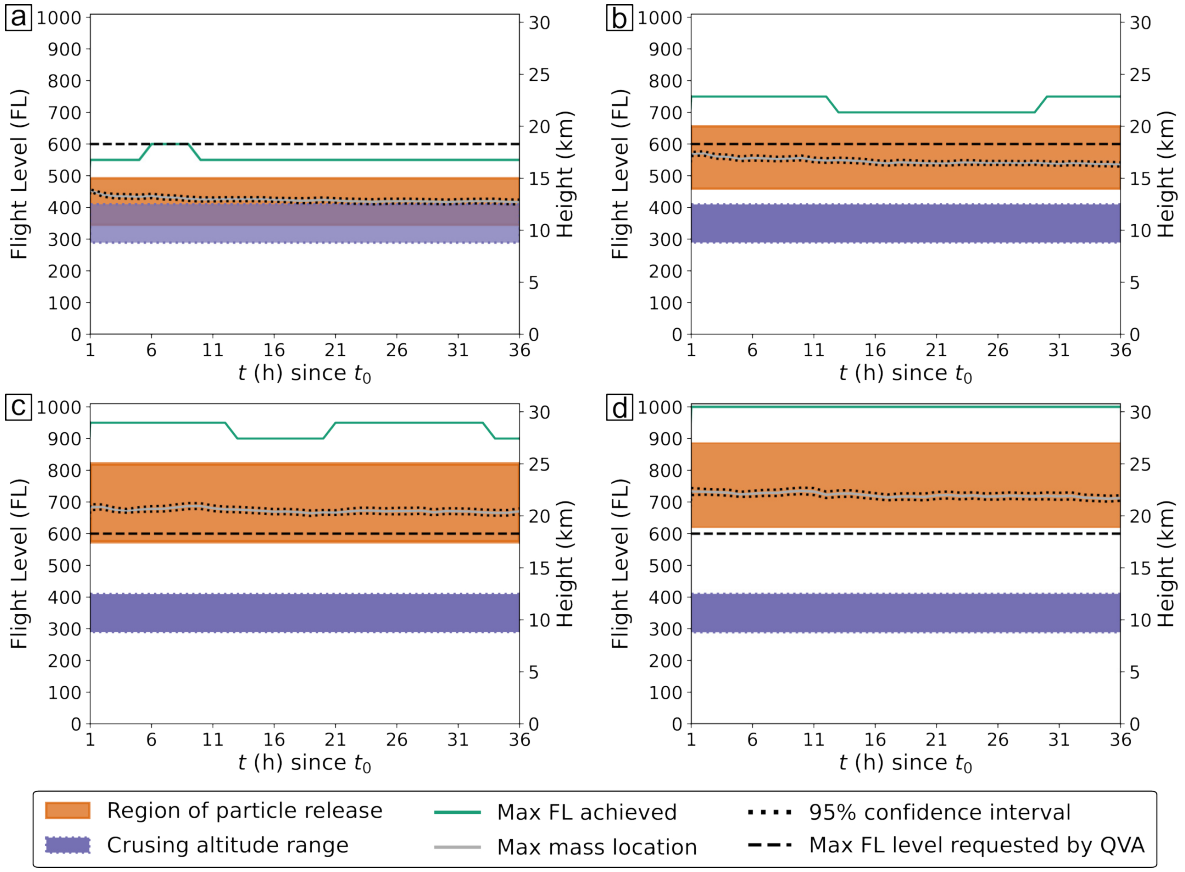

Figure 3.9: Maximum mass of particles in the atmosphere as a function of time for particle release heights of **(a)** $H_T = 15\,\mathrm{km}$, **(b)** $H_T = 20\,\mathrm{km}$, **(c)** $H_T = 25\,\mathrm{km}$, and **(d)** $H_T = 27\,\mathrm{km}$. The orange boxes correspond to the release region, the purple box refers to the range of commercial cruising altitudes, $\sim$ FL290 to FL410 (Fichter et al., 2005). The light grey line indicates the average FL location of the maximum mass, and the black dotted line represents the 95% confidence interval, including all weather patterns, days, and release times. The black dashed line represents the maximum requested FL to be reported in QVA information.

et al. (2016). Any generalisations linking dispersion characteristics to weather patterns could be more likely with a larger data set of weather patterns, as done by Harrison et al. (2022). They identify mean flow speeds in the mid-upper troposphere per weather pattern out of the set of 30. We assume that the less far-travelled ash clouds in weather patterns 5 to 8 (Figure 3.6e-h) originate from the grouping method, as they only contain a few of the 30 weather patterns, while weather patterns 1 to 4 (Figure 3.6a-d) contain 21 out of 30 weather patterns in total, see Figure 3.3.

A clear relationship between the ash cloud dispersion and release height is observed in Figure 3.7. Chapter 2 previously confirmed that the plume/release height is an extremely important eruption source parameter for modelling the ash from co-PDCs, just like vent-derived eruptions (Devenish et al., 2012; Harvey et al., 2018). Here, we have shown that changes in the ash concentration also depend on the release height (H_T), where only low release heights show low ash concentrations

(Figure 3.7a & b). As previously detailed, we modelled the co-PDC plumes as an ash release at a specific height range and not from the vent up to the plume top (as is done by the UK Met Office operationally for Plinian plumes). This impacts our observations as the particles are not released into the entire atmosphere but rather only into the stratosphere. The short release time ($10\,\mathrm{min}$) is also of importance, as all the ash particles travel with similar wind shear and thus might remain in a similar location, with concentration changes largely due to different MERs.

In contrast, similarities between $H_T = 25\,\mathrm{km}$ and $H_T = 27\,\mathrm{km}$ outputs were found. We observe very similar cloud behaviour in terms of location, shape, size, extent, and concentration (i.e., Figure 3.7). Similarities between $H_T = 25\,\mathrm{km}$ and $H_T = 27\,\mathrm{km}$ are also observed in terms of the total cloud area distribution (i.e., Figure 3.8c & d). This is due to the high altitude in the stratosphere, where the particles are released. At these altitudes, less turbulence acts on the ash particles.

Our results highlight the importance of knowing H_T and any changes that occur during an ongoing eruption. For example, variation in a (vent-derived) plume height of $6\,\mathrm{km}$ by a $1\,\mathrm{km}$ uncertainty can impact the estimated cloud-covered minimum and maximum area by a factor of 3 (Dioguardi et al., 2020). Given the dispersion model output varies greatly with release height and thus MER for both co-PDC plumes and vent-derived plumes (as also shown by Chapter 2; Aubry et al. (2023), Beckett et al. (2020), Dioguardi et al. (2020), Dürig et al. (2018), and Mastin, Pavolonis, et al. (2022)), it would be beneficial to the forecasts and operational setups to know the exact release height from co-PDC plumes during a real-time event to initialise the dispersion modelling. This includes reconciling data and observations from different measurement methods such as visual ground-based observations (potentially non-trained scientists), pictures or video footage, different remote sensing techniques (ground-based radar, lidar, (visible) cameras, and satellites or aircraft observations) and potentially coupling them with numerical models (Alexander, 2013; Carey & Bursik, 2015; Corradini et al., 2016; Durant et al., 2010; Dürig et al., 2018; Engwell et al., 2021; Mastin, Pavolonis, et al., 2022; Pardini et al., 2024; A. J. Prata, 2009; F. Prata & Rose, 2015; Rose et al., 2000; Scollo et al., 2014; Simionato et al., 2024; Wiegner et al., 2012). Furthermore, these observations can be hindered by meteorological cloud coverage, adverse weather, differentiation between ash and ice or water, and night-time light limitations (Engwell & Eychenne, 2016; Hadley et al., 2004; Pardini et al., 2024; F. Prata & Rose, 2015; Simpson et al., 2002). Finally, although the relationship between H_T and MER (Equation 3.5) has been shown to hold for large co-PDC events, the limits of this H_T-MER relationship remain to be tested for the full range of co-PDC plume heights.

3.4.2 Impacts for aviation

The newly introduced QVA concentration thresholds help evaluate risk of volcanic ash encounters for the aviation industry. We have shown that the cloud extent with ash concentrations $\geq 0.2\,\mathrm{mg\,m^{-3}}$ increases with time (for at least the first $36\,\mathrm{h}$). For short times after particle release, we observe

small to non-existent cloud margins with lower ash concentrations (e.g., Figure 3.5, Figure 3.6, and Figure 3.7). Across all our model runs, the maximum ash concentration achieved was $28\,840\,\mathrm{mg\,m^{-3}}$ (modelled for 3rd August 2017 at $1\,\mathrm{h}$ after particle release, $H_T = 27\,\mathrm{km}$ at FL650 - FL700). However, these and similar high ash concentrations are observed throughout the whole dataset (often $\geq 10\,\mathrm{mg\,m^{-3}}$) and are thus a common feature of the co-PDC clouds modelled.

Witham et al. (2012) modelled the maximum ash concentration range generated from the 26th February 2000 eruption of Hekla, Iceland, along the flight path of a NASA DC-8 research aircraft that encountered ash on the 28th February 2000 and suffered engine damage (Grindle & Burcham, 2003; Witham et al., 2012). The Hekla eruption column up to $12\,\mathrm{km}$ (Lacasse et al., 2004; Witham et al., 2012) reached a maximum ash concentration of $4\text{-}5\,\mathrm{mg\,m^{-3}}$ on the flight path. Similarly, Witham et al. (2012) modelled the ash concentrations during the 24th June 1982 eruption of Galunggung, Indonesia. An ash encounter with a British Airways Boeing 747 aircraft led to failure of all four engines (F. Prata & Rose, 2015; Witham et al., 2012) and the modelled concentrations reached a maximum of $\sim 45\text{-}320\,\mathrm{mg\,m^{-3}}$ for plume heights of $12\text{-}16\,\mathrm{km}$, with large uncertainties depending on the eruption height (Witham et al., 2012). More broadly, the maximum ash concentration modelled by Witham et al. (2012) for five different volcanic ash aircraft encounters is $200\,\mathrm{mg\,m^{-3}}$. For each simulation, Witham et al. (2012) used a power law relationship between the plume height and MER, which compares well with the H_T-MER relationship by Mastin et al. (2009). Furthermore, Dioguardi et al. (2020) analysed the ash concentration of the 2010 Eyjafjallajökull eruption on 6th May and found in FL000 - FL200 forecasted peak ash concentrations of $13.833\,\mathrm{mg\,m^{-3}}$. This is consistent with the $13.870\,\mathrm{mg\,m^{-3}}$ peak ash concentration found on 7th May by Beckett et al. (2020) in FL000 - FL200 and FL200 - FL350 across different model parameter settings. For the determination of MER, Beckett et al. (2020) and Dioguardi et al. (2020) used the H_T-MER relationship defined by Mastin et al. (2009) and applied a 5% distal fine ash fraction scaling, which accounts for physical processes such as aggregation and fall-out of large, heavy particles close to the source.

For our co-PDC clouds we found the maximum ash concentration to be $28\,840\,\mathrm{mg\,m^{-3}}$ at FL650 - FL700 for $H_T = 27\,\mathrm{km}$, which corresponds to an input value for MER of $2.4 \times 10^8\,\mathrm{kg\,s^{-1}}$, and at FL300 - FL400 (corresponding to commercial airspace use) ash concentrations are $\geq 11\,\mathrm{mg\,m^{-3}}$. This is in line with previous NAME studies of ash-aircraft encounters from vent-derived plumes. The extremely high maximum ash concentrations (e.g., $\sim 28\,840\,\mathrm{mg\,m^{-3}}$) relative to those previously reported for vent-derived plumes can be explained well by our different modelling approach, which reflects, at least in part, the different co-PDC source conditions. Firstly, we only released the particles in the top 30% of the plume (refer to Equation 3.4) to reflect dispersion at a level of neutral buoyancy. Secondly, we used a fine TGSD appropriate for co-PDCs and have not applied a distal fine ash fraction scaling, meaning that the entire mass is applied to the downwind dispersion. Thirdly, we used a larger range in plume heights and thus MERs compared to these previous studies on vent-derived plumes.

At $12\,\mathrm{h}$ after particle release, ash clouds above approximately FL350 contain almost solely high and very high ash concentrations as defined by QVA (Figure 3.7, Figure B.3, and Figure B.4) and thus pose a tangible aviation risk.

3.4.3 Elevation of maximum mass and atmospheric impact

We now consider the mass distribution within the ash cloud (Figure 3.9). After a short ($10\,\mathrm{min}$) particle release duration, we then track the ash mass within the ash cloud as it moves downwind. Within the first $36\,\mathrm{h}$, across all weather patterns, dates, and start times, we observe two consistent behaviours. (i) The maximum FL achieved remains 50 to 150 flight levels above the release region within the first $36\,\mathrm{h}$. (ii) The elevation of maximum mass sits within the release region. The fine co-PDC grain size (Engwell & Eychenne, 2016; Sigurdsson & Carey, 1989) contributes to this observation, as these particles have long atmospheric residence times and can travel far distances (Engwell & Eychenne, 2016; Pardini et al., 2024; Saxby et al., 2018). Particle sedimentation is still present, but the settling velocity is low compared to the vertical component of air velocity (McLean et al., 2024). These findings are useful for future operational setups at volcanic ash advisory centres (VAACs) that consider the ash concentration from a co-PDC. The maximum mass is only expected to align with FLs used for commercial airspace when release heights are smaller than $H_T = 20\,\mathrm{km}$. However, as previously shown, the ash concentration remains high (relative to QVA) across most FLs (for release at $\geq H_T = 20\,\mathrm{km}$).

Throughout this study, increase in height, i.e., particles being released travelling into higher elevations (e.g., Figure 3.5, Figure 3.8 and Figure 3.9 after particle release in a specific elevation) has been observed. This is due to vertical movements and circulations, e.g., wind shear and turbulent mixing, within the meteorological data. However, the specific NAME representation of these vertical turbulences, especially free tropopause turbulences, may impact the results. The NAME models in this study use a constant, uniform value for the diffusion process of turbulences above the boundary layer (i.e., in the free tropopause). A study by Dacre et al. (2015) showed that the vertical particle distribution can be over- or underestimated by NAME and can be improved by parametrisation of volcanic ash layer thickness. Furthermore, a NAME add on scheme, better representing the free tropopause turbulence by space–time-variation has been analysed (Mirza et al., 2024) and could be considered in future work to study this upward movement in more detail.

The atmospheric boundary layer (i.e., the lowest layer of the atmosphere, interacting directly with the surface), represented by different start times, does not appear to impact our results, as our particles are released at high elevation above the boundary layer and show consistent results across all release times, irrespective of time of day. The different eruption start times provide both different weather conditions and boundary layer levels (Dai, 2023; Dang et al., 2019), but no extreme differences or patterns in the resulting ash cloud are observed. The focus on vertical atmospheric layers, e.g., flight levels, means that convective and vertical mixing needs to be considered, and the way these are modelled within NAME might have a minor impact on the vertical location, the

particles achieve. Future work could continue to test these results by examining different release locations outside of Iceland and by further varying the meteorological impact. For example, previous observations at different latitudes found that the volcanic plume height attained is impacted by humidity and wind shear (Carey & Bursik, 2015; Tupper et al., 2009).

3.4.4 Implications for other dispersion events

In this study, we used the total grain size distribution (TGSD) documented for the Campanian co-ignimbrite eruption (Marti et al., 2016). This TGSD with a mode $= 37\,\mu\mathrm{m}$ (Marti et al., 2016) is likely to be representative of other co-PDC plumes (Engwell & Eychenne, 2016), as they all form by a common self-selecting process wherein segregated particles buoyantly lift off. However, this remains to be verified. Furthermore, this work could be expanded and compared to other events that (re)suspend particulate matter in a similar way. This could include resuspended ash events (Del Bello et al., 2021; Ernst et al., 1996; Etyemezian et al., 2019; Leadbetter et al., 2012; Liu et al., 2014; Pardini et al., 2024; Sparks et al., 1997; Thorsteinsson et al., 2012), as they show a similar grain size characteristics to co-PDCs (Del Bello et al., 2021; Liu et al., 2014). Liu et al. (2014) show the modes of remobilised ash to be 32-$63\,\mu\mathrm{m}$. Additionally, sub-Saharan dust (Đorđević et al., 2004; Middleton & Goudie, 2001; Vukmirović et al., 2004) has a similar grain size with a mode 1-$30\,\mu\mathrm{m}$ (Middleton & Goudie, 2001).

3.5 Conclusion

We studied the vertical ash concentration, transport, and dispersion of co-PDC ash clouds from the ground surface (i.e., FL 0) up to FL1000 ($\sim 30\,\mathrm{km}$ altitude) using eruption source parameters (ESPs) that are appropriate for (large) co-PDCs. We focused on large co-PDCs to provide an upper limit on the likely natural range. We showed that the ash cloud location, shape, or size at each 50 flight levels cannot be directly related to a specific weather pattern, and thus these cloud characteristics cannot be rigorously pre-determined by knowing the weather pattern. We also observed 'very high' ash concentrations ($\geq 10\,\mathrm{mg\,m^{-3}}$; as classified by the QVA) for all release/plume heights above $H_T = 20\,\mathrm{km}$, and ash clouds that are compact in shape with little to no reduction in concentration towards the cloud margins. For all release heights ($H_T = 15\,\mathrm{km}$, $20\,\mathrm{km}$, $25\,\mathrm{km}$ & $27\,\mathrm{km}$), variations in the ash concentration at each FL interval were observed. However, little variation in the associated cloud location is observed between the different FLs for a given plume height at $12\,\mathrm{h}$ since particle release. $H_T = 25\,\mathrm{km}$ and $H_T = 27\,\mathrm{km}$ describe similar ash cloud location and shape. The total cloud area exceeding $0.2\,\mathrm{mg\,m^{-3}}$ at each 50 flight level interval increases with time (within the first $36\,\mathrm{h}$) and hence increases the hazard to aviation. Again, within the first 36h, the elevation of the maximum mass always resides within the release region, and the maximum flight level achieved by the ash is 50 to 150 flight levels above the release region.

Although the ash clouds generated from co-PDCs have a small total area (typically $< 300\,000\,\mathrm{km}^2$), they show very high ash concentrations (max. $28\,840\,\mathrm{mg\,m}^{-3}$) and thus, in the event of an eruption producing a co-PDC plume, would pose a significant threat to aviation.

4. Synthesis & Conclusions

4.1 Key contribution to knowledge

Co-PDCs can form by buoyant lift-off from any underlying pyroclastic density current and disperse fine particles and hot gas over large areas into the atmosphere. Due to its generation process, co-PDCs possess unique eruption source parameters (ESPs), such as an elongated source geometry and fine particles, compared to typical vent-derived plumes. I studied the application of some of these co-PDC ESPs in the UK Met Office's Numerical Atmospheric-dispersion Modelling Environment, NAME. Specifically, the studied ESPs here included the source area, A, aspect ratio, α, plume height, H_T, and release duration, t_r. The ash dispersion outputs were then analysed both in terms of their total column mass loadings and their vertical position and concentration. A summary of the main findings is given in the following:

- This study provides an overview of the range of ESPs of co-PDC (Table 2.1) and insight into how these can be implemented in NAME. Co-PDCs have an elongated source shape with high aspect ratio and a large area (up to $600\,\mathrm{km}^2$). The plume heights can fall within a similar range as vent-derived plumes from 1-$30\,\mathrm{km}$ with dominant particle release at a specific level of neutral buoyancy.

- The analysis shows that the plume height and MER are among the most important and impactful parameters for co-PDCs (as is the case for vent-derived plumes). Source geometry and source area show less impact on the ash cloud location, shape, and size. This analysis was done with the driving motivation for operational systems to reduce complexity and to set up future work where the need for a more accurate determination of parameters can be addressed.

- The newly introduced QVA thresholds for ash concentration are applied. Ash clouds released above $15\,\mathrm{km}$ agl often reside in very high ash concentrations, often substantially $\geq 10\,\mathrm{mg\,m^{-3}}$. In the first $12\,\mathrm{h}$, the margin of the clouds is sharp, rather non-existent (commonly for $H_T \geq 20\,\mathrm{km}$) and the cloud interior remains high in concentration.

- The cloud area increases within each FL for the first $36\,\mathrm{h}$.

- Neglecting particle aggregation, the elevation of the maximum mass is relatively stable within the first $36\,\mathrm{h}$ after particle release and stays within the release height region. The maximum flight level (FL) reached is 50 to 150 FLs above the release region, again within the first $36\,\mathrm{h}$.
- The findings confirm the importance of accurate determination of the plume height, H_T, in (near-)real-time to correctly estimate the impact of co-PDC plumes for VAAC and aviation, and stress that even with past efforts and research made, this is a crucial topic that needs to be further developed.

4.2 Future work

While Co-PDC lift-offs are of irregular elongated shape, for the NAME model runs in this work, they have been approximated by a rectangle. Future work could study and compare findings from sources of other shapes. Given that my findings show that changes in source area have little impact on the ash cloud location and area, it would be interesting to determine whether our results can also be applied to other particle transport events with non-point source geometries, e.g., resuspension (Del Bello et al., 2021; Ernst et al., 1996; Etyemezian et al., 2019; Leadbetter et al., 2012; Liu et al., 2014; Pardini et al., 2024; Sparks et al., 1997; Thorsteinsson et al., 2012), sub-Saharan dust (Đorđević et al., 2004; Middleton & Goudie, 2001; Vukmirović et al., 2004) or small vent-derived plumes. Additionally, verifying the H_T-MER power law relationship for small co-PDC plumes with respect to the Aubry et al. (2023) relationship and for other plume models (Biass et al., 2016; Bonadonna, Macedonio, & Sparks, 2002; Druitt et al., 2002; Woods & Kienle, 1994) would be of great use.

Chapter 2 would benefit from studying different weather patterns in the numerical experiments to also include weather variability, variation in wind speed and direction, and consider the impact of meteorology in general. Future work for both data chapters (Chapters 2 and 3) could consider using the set of 30 weather patterns (Neal et al., 2016). Even though the set of 30 weather patterns still remains a selection of all possible weather phenomena, the larger number of pattern classifications groups the dynamic weather behaviours closer together, and as such better represents the natural variability.

This entire study assumed a constant and uniformly distributed vertical mass around the region of neutral buoyancy. However, PDCs can inject ash into a wider range of altitudes, from the ground to the plume top height. This could impact the particle release thickness and elevation, and therefore impact the downwind cloud transport and dispersion. This might be considered by varying the release height, vertical mass distribution at source, and MER in future work.

This study neglected particle aggregation processes to fully study ash dispersion and transport without additional impacting factors. However, our findings should be compared and verified with NAME simulations considering particle aggregation as this would increase the particle fallout, due to larger particles and sedimentation rate, and therefore reduce the cloud area and ash concentration.

For example, we would expect the elevation of maximum mass descending faster with time and potentially leaving the release region within the first $36\,\mathrm{h}$.

Although I have provided insights into ash cloud dispersion for co-PDCs, I always used Iceland as the eruption location as a unique geographic locations with the particle release, mainly, into the stratosphere. Future work could be done to determine whether my conclusions are still true for different eruption locations or are limited to the latitudinal extent of the release region ($\sim$ 64 °N).

In Chapter 3, the QVA thresholds were applied when comparing the ash cloud location and used to draw conclusions about the area subject to aviation hazards. In order to provide further understanding of the distribution of the ash concentration across the vertical cloud extent, the QVA thresholds should also be applied to the cloud area per flight level, especially in altitudes commonly used for civil aviation ($\sim$ FL290 to FL410 (Fichter et al., 2005)).

Current limitations have to be stressed as they restrict the possible expansion of this research project. Large data sets and the handling of these became more challenging, especially with the application to various weather patterns and the repetition for different dates in chapter 3. The amount of successful NAME model runs (Chapter 2: 63 and Chapter 3: 292 runs) required a large amount of computational time on the supercomputer for NAME runs, but also for post-processing the data and their visualisation. Data storage provides an additional limitation.

In my opinion, the biggest constraint to future work is the limitations of data/output visualisation. The need to visualise an entire 4D data set (time, height, latitude, longitude) for each model run hinders a full overview of each component and potentially also means that some relationships can be overlooked. This needs to be faced in the future. Here, I limited myself by displaying model outputs for only a selected number of representative runs and ask the reader to project this for different weather patterns and different times after release time. These difficulties would further increase when using 30 weather patterns (not 8) and require new visualisation techniques, and may benefit from progress in other research areas (e.g, computer sciences, atmospheric sciences) and evolution in data handling.

A. Modelling the transport and dispersion of volcanic co-PDC ash clouds using NAME: an evaluation of source geometry and mass eruption rate

All additional figures used for this chapter are shown in the following. Figure A.1 – Figure A.6 provide the NAME output overview for the other aspect ratios and areas not presented in the main document. Figure A.7 – Figure A.15 repeated all the parameter settings with a modelled particle release time over the whole modelled time (i.e., $24\,\mathrm{h}$).

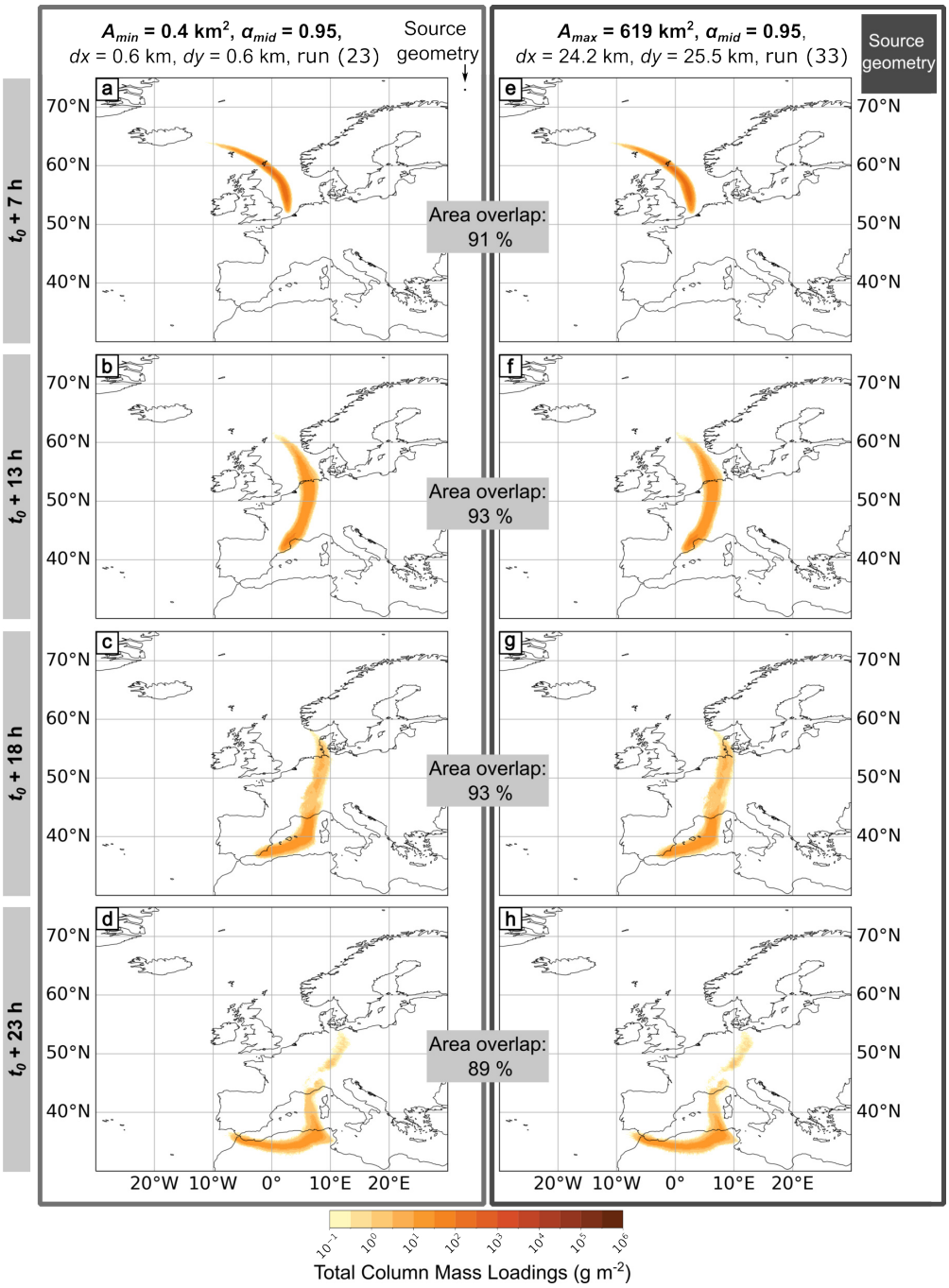

Figure A.1: NAME outputs for numerical experiment 1, all using $\alpha_{mid} = 0.95$, a $1\,\mathrm{h}$ particle release, $z = 8.5\,\mathrm{km}$, $dz = 3\,\mathrm{km}$ and MER $= 1.06 \times 10^{13}\,\mathrm{g\,h^{-1}}$. The panels on the left are for the minimum source area, and the panels on the right are for the maximum. The area and orientation of the two source geometries are compared in relation to each other next to the parameter list at the top of the figure. For each area, four outputs are presented at different times after the eruption start t_0: **(a & e)** $7\,\mathrm{h}$, **(b & f)** $13\,\mathrm{h}$, **(c & g)** $18\,\mathrm{h}$, and **(d & h)** $23\,\mathrm{h}$. Total column mass loadings are averaged over the previous hour, and we applied a threshold of $0.2\,\mathrm{g\,m^{-2}}$.

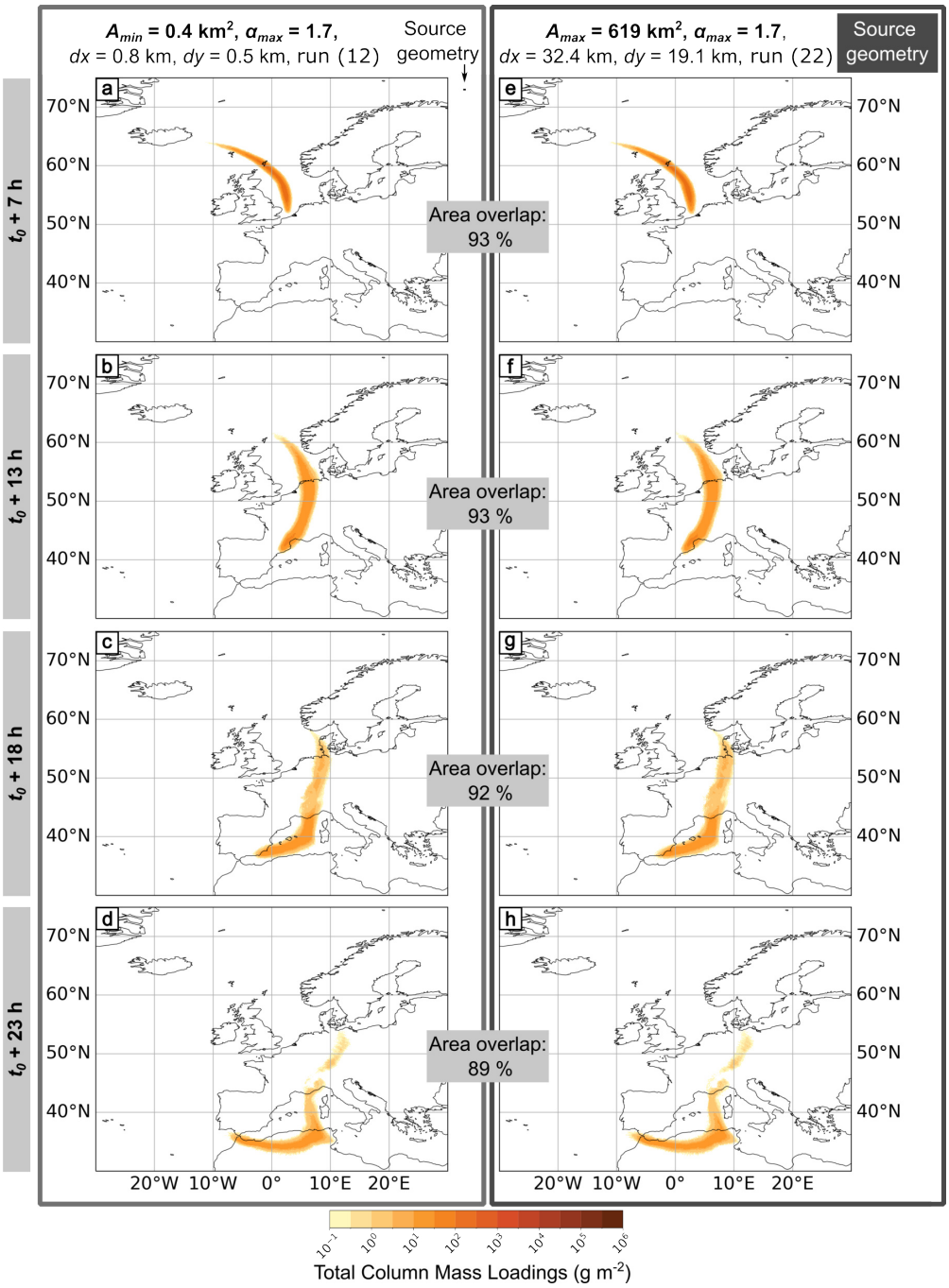

Figure A.2: NAME outputs for numerical experiment 1, all using $\alpha_{max} = 1.7$, a $1\,\mathrm{h}$ particle release, $z = 8.5\,\mathrm{km}$, $dz = 3\,\mathrm{km}$ and MER $= 1.06 \times 10^{13}\,\mathrm{g\,h^{-1}}$. The panels on the left are for the minimum source area, and the panels on the right are for the maximum. The area and orientation of the two source geometries are compared in relation to each other next to the parameter list at the top of the figure. For each area, four outputs are presented at different times after the eruption start t_0: **(a & e)** $7\,\mathrm{h}$, **(b & f)** $13\,\mathrm{h}$, **(c & g)** $18\,\mathrm{h}$, and **(d & h)** $23\,\mathrm{h}$. Total column mass loadings are averaged over the previous hour, and we applied a threshold of $0.2\,\mathrm{g\,m^{-2}}$.

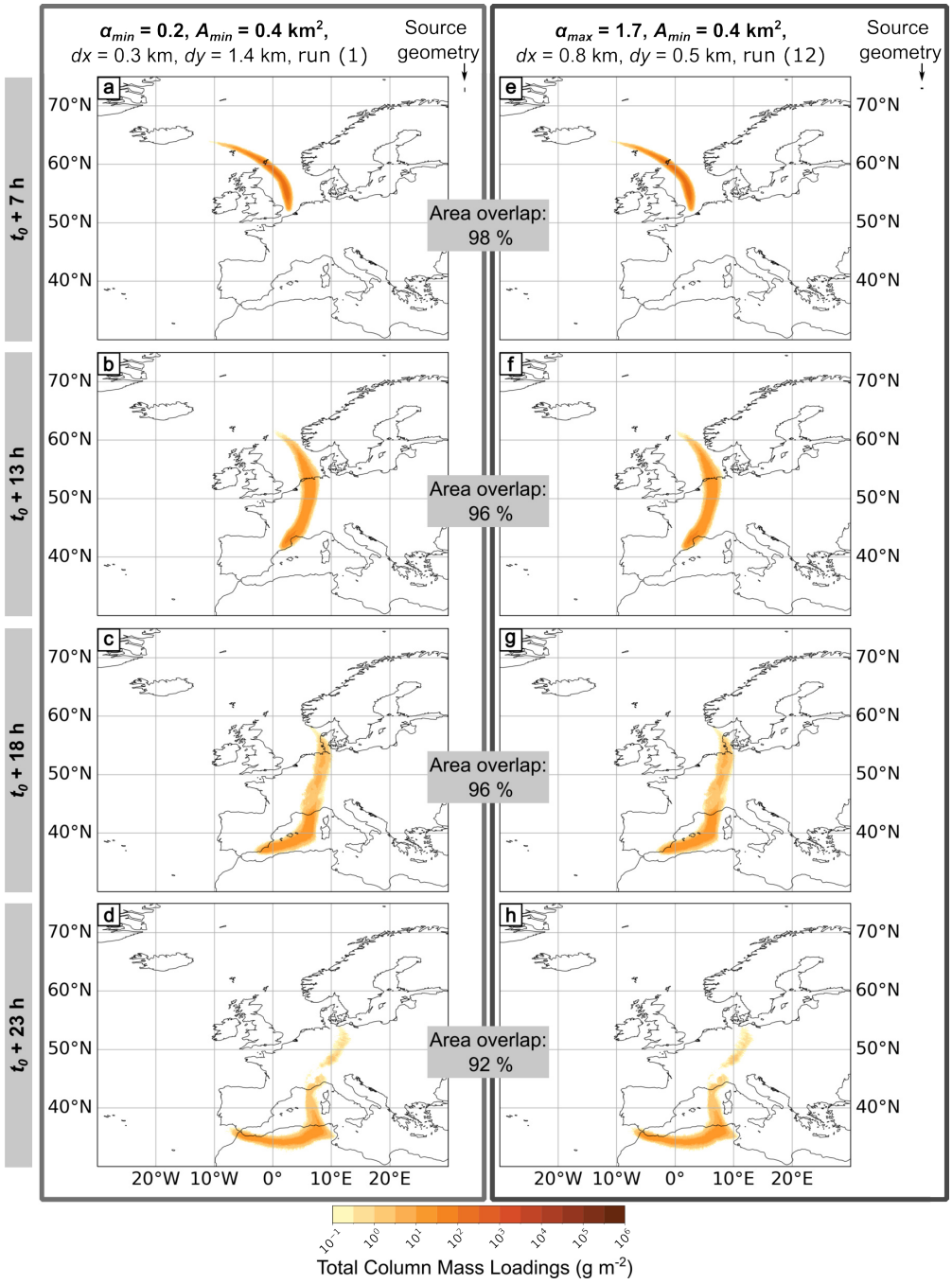

Figure A.3: NAME model outputs for numerical experiment 1, all using $A_{min} = 0.4\,\mathrm{km}^2$, a $1\,\mathrm{h}$ particle release, $z = 8.5\,\mathrm{km}$, $dz = 3\,\mathrm{km}$ and MER = $1.06 \times 10^{13}\,\mathrm{g\,h}^{-1}$. The left figure panels **(a-d)** show results from the minimum aspect ratio $\alpha_{min} = 0.2$, and the right panels **(e-h)** show the maximum aspect ratio $\alpha_{max} = 1.7$. The area and orientation of the two source geometries are compared in relation to each other next to the parameter list at the top of the figure. For each aspect ratio, four outputs at different times after eruption start t_0 are shown: **(a & e)** $7\,\mathrm{h}$, **(b & f)** $13\,\mathrm{h}$, **(c & g)** $18\,\mathrm{h}$, and **(d & h)** $23\,\mathrm{h}$. Total column mass loadings are averaged over the previous hour, and we applied a threshold of $0.2\,\mathrm{g\,m}^{-2}$.

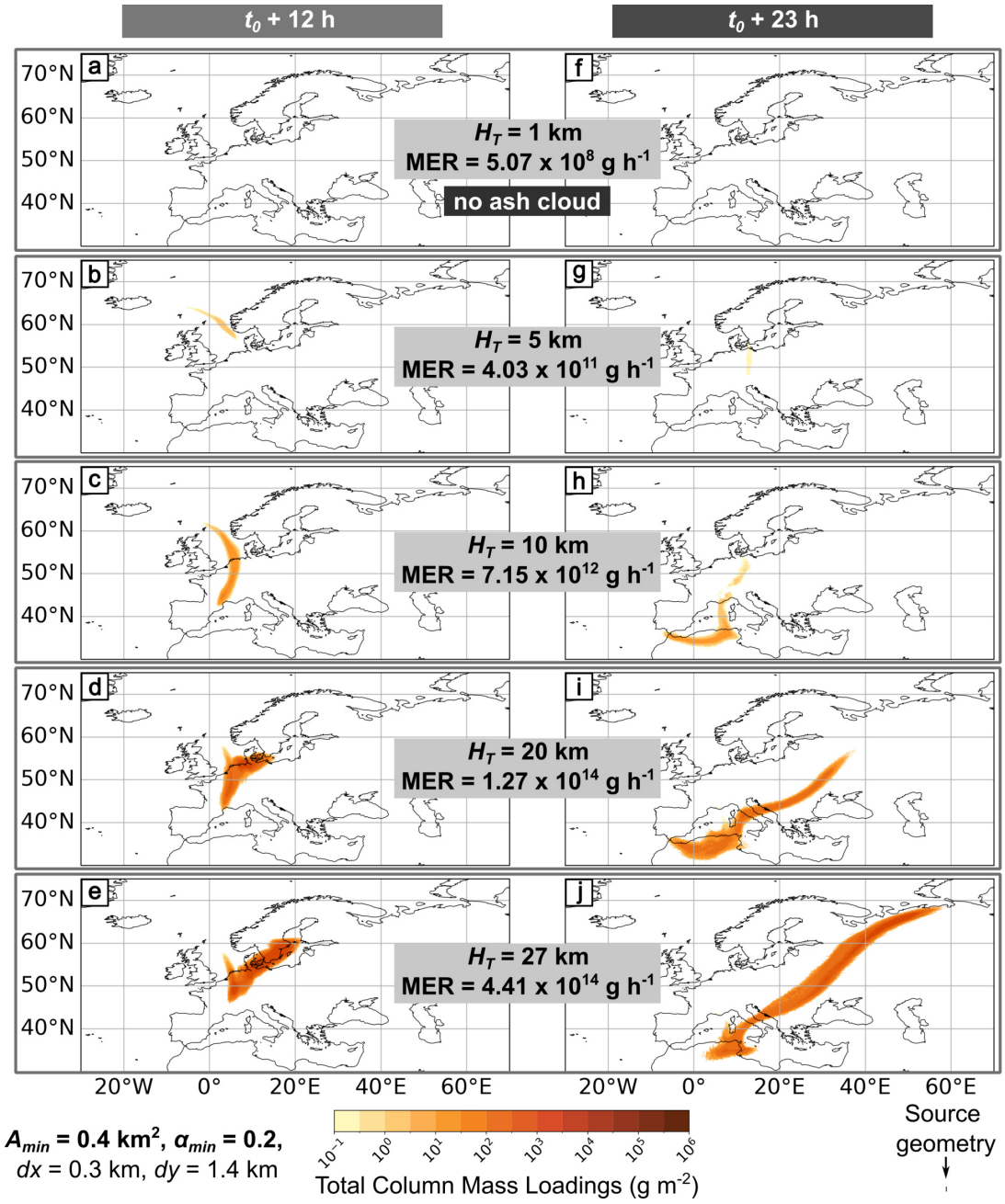

Figure A.4: NAME model outputs for experiment 2, all using a $1\,\mathrm{h}$ particle release with different H_T, MER, and *dz*. The figure panels on the left **(a-d)** are for $12\,\mathrm{h}$ after eruption start t_0, and the panels on the right **(e-h)** show $23\,\mathrm{h}$ after eruption start t_0. The outputs here are for $A_{min} = 0.4\,\mathrm{km}^2$ with $\alpha_{min} = 0.2$. With increasing H_T and *t* (h), the plume size grows. Total column mass loadings are averaged over the previous hour, and we applied a threshold of $0.2\,\mathrm{g\,m^{-2}}$. The subplots **(a & f)** show no ash cloud (i.e., mass loading $< 0.2\,\mathrm{g\,m^{-2}}$).

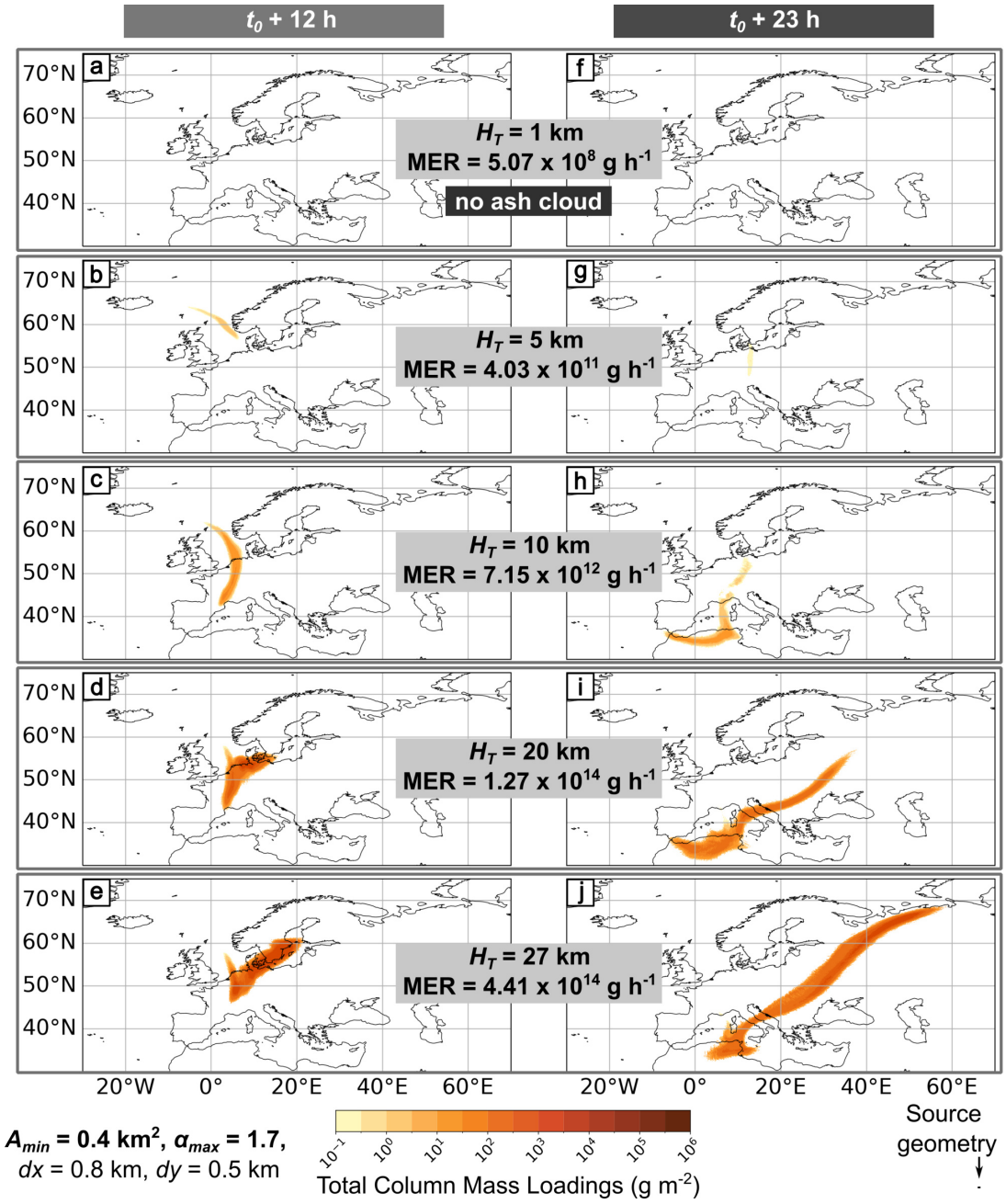

Figure A.5: NAME model outputs for experiment 2, all using a $1\,\mathrm{h}$ particle release with different H_T, MER, and *dz*. The figure panels on the left **(a-d)** are for $12\,\mathrm{h}$ after eruption start t_0, and the panels on the right **(e-h)** show $23\,\mathrm{h}$ after eruption start t_0. The outputs here are for $A_{min} = 0.4\,\mathrm{km}^2$ with $\alpha_{max} = 1.7$. With increasing H_T and *t* (h), the plume size grows. Total column mass loadings are averaged over the previous hour, and we applied a threshold of $0.2\,\mathrm{g\,m^{-2}}$. The subplots **(a & f)** show no ash cloud (i.e., mass loading $< 0.2\,\mathrm{g\,m^{-2}}$).

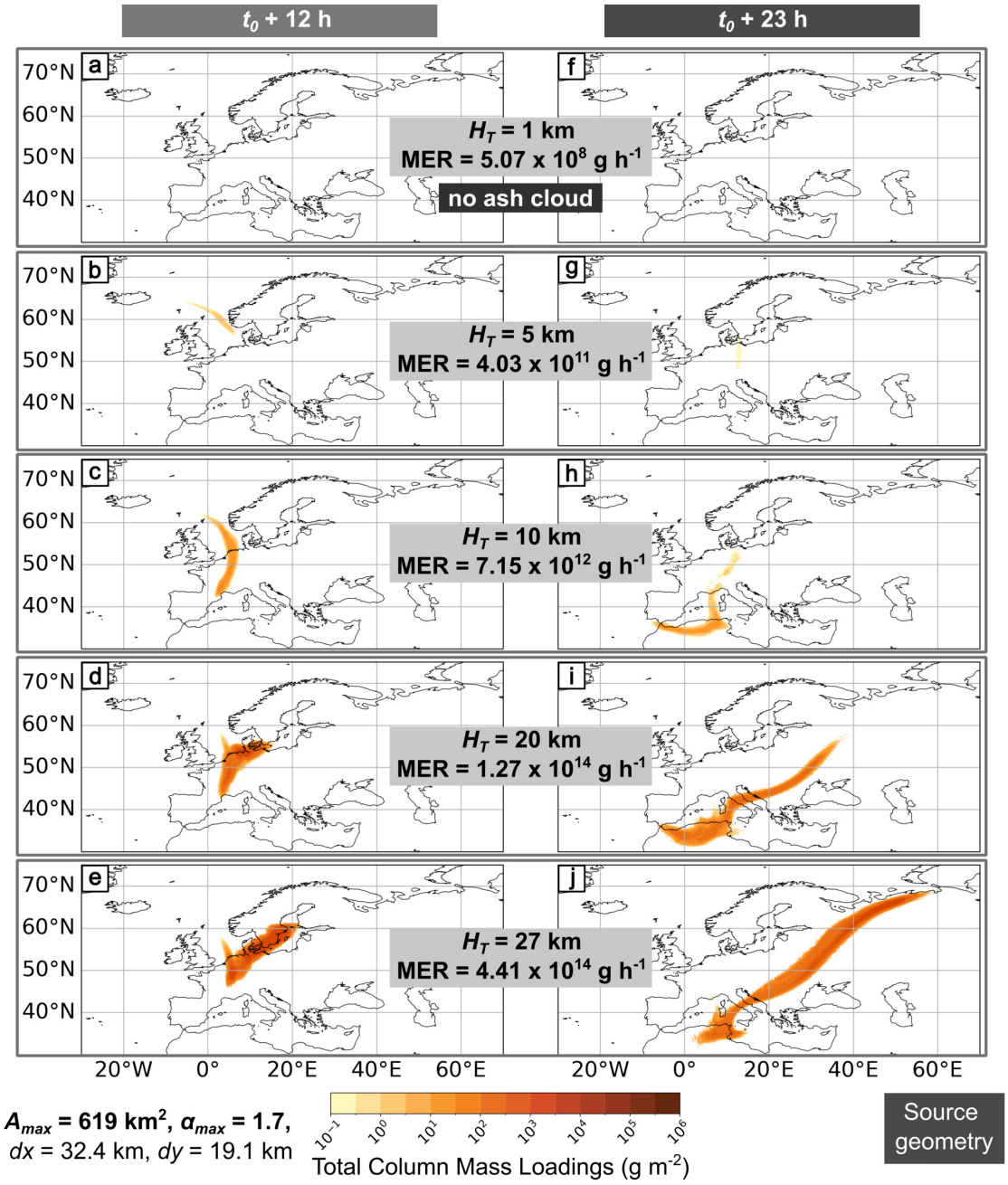

Figure A.6: NAME model outputs for experiment 2, all using a $1\,\mathrm{h}$ particle release with different H_T, MER, and *dz*. The figure panels on the left **(a-d)** are for $12\,\mathrm{h}$ after eruption start t_0, and the panels on the right **(e-h)** show $23\,\mathrm{h}$ after eruption start t_0. The outputs here are for $A_{max} = 619\,\mathrm{km}^2$ with $\alpha_{max} = 1.7$. With increasing H_T and *t* (h), the plume size grows. Total column mass loadings are averaged over the previous hour, and we applied a threshold of $0.2\,\mathrm{g\,m^{-2}}$. The subplots **(a & f)** show no ash cloud (i.e., mass loading $< 0.2\,\mathrm{g\,m^{-2}}$).

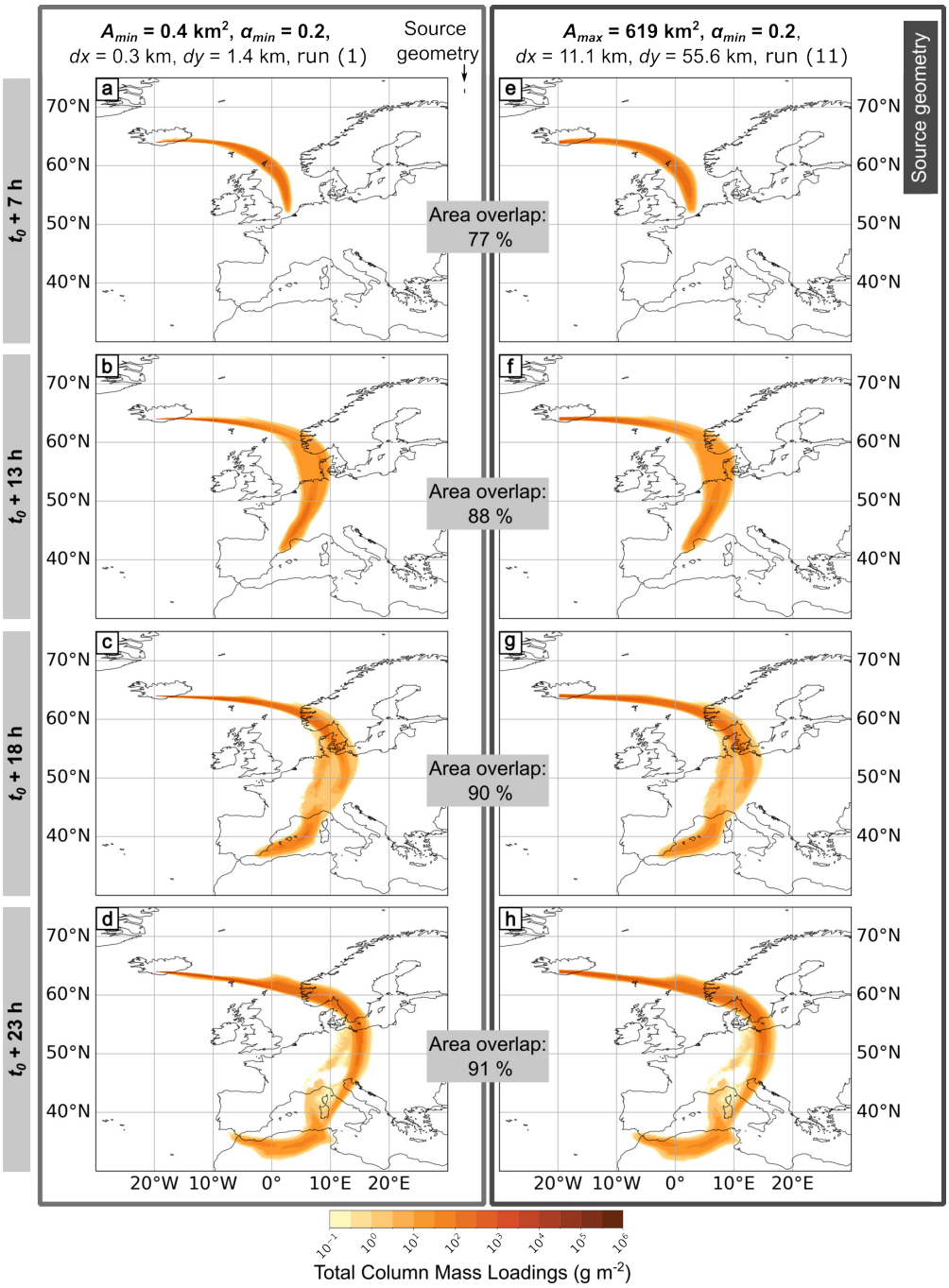

Figure A.7: NAME outputs for numerical experiment 1, all using $\alpha_{min} = 0.2$, a $24\,\mathrm{h}$ particle release, $z = 8.5\,\mathrm{km}$, $dz = 3\,\mathrm{km}$ and MER $= 1.06 \times 10^{13}\,\mathrm{g\,h^{-1}}$. The panels on the left are for the minimum source area, and the panels on the right are for the maximum. The area and orientation of the two source geometries are compared in relation to each other next to the parameter list at the top of the figure. For each area, four outputs are presented at different times after the eruption start t_0: **(a & e)** $7\,\mathrm{h}$, **(b & f)** $13\,\mathrm{h}$, **(c & g)** $18\,\mathrm{h}$, and **(d & h)** $23\,\mathrm{h}$. Total column mass loadings are averaged over the previous hour, and we applied a threshold of $0.2\,\mathrm{g\,m^{-2}}$.

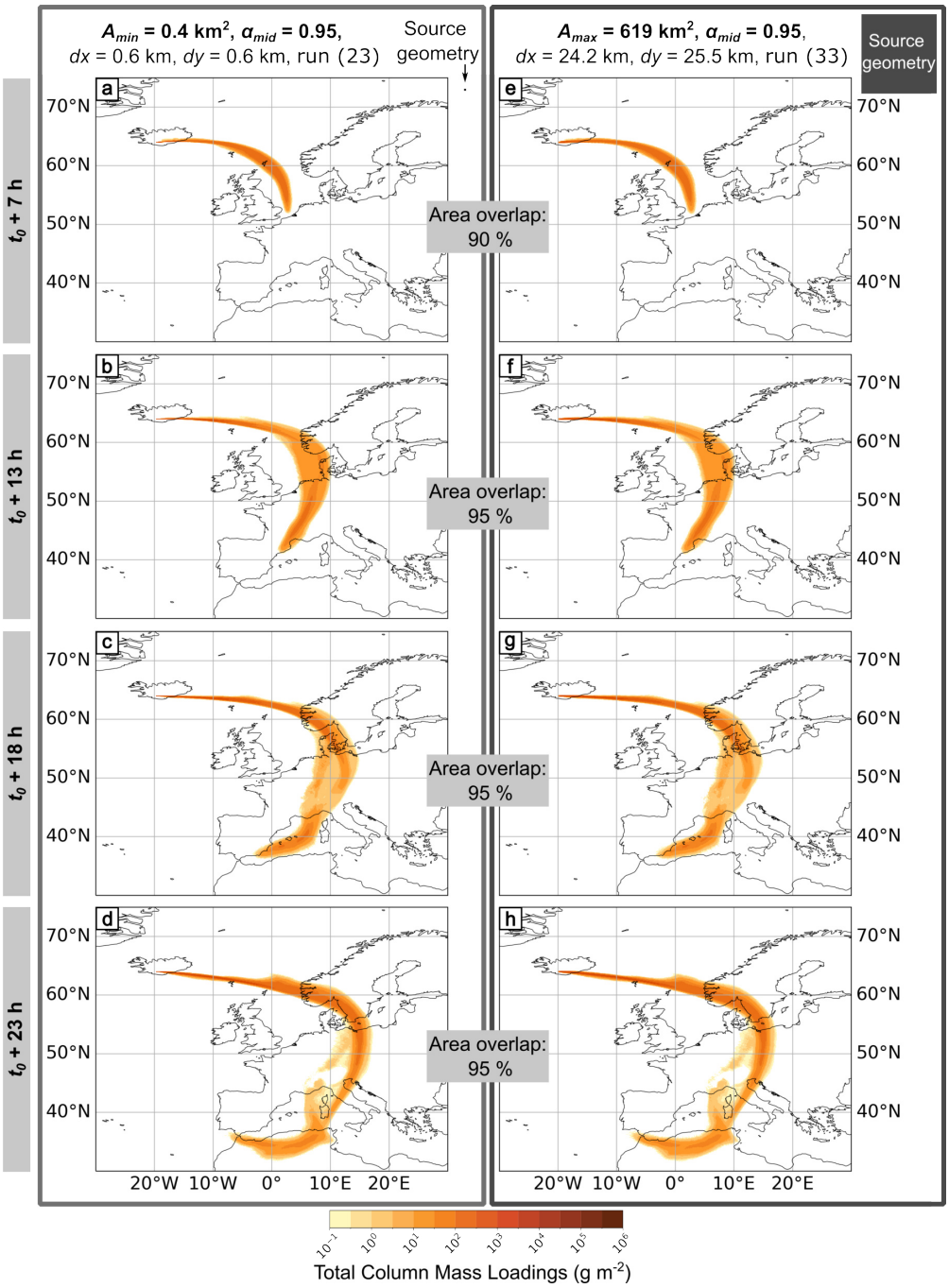

Figure A.8: NAME outputs for numerical experiment 1, all using $\alpha_{mid} = 0.95$, a $24\,\mathrm{h}$ particle release, $z = 8.5\,\mathrm{km}$, $dz = 3\,\mathrm{km}$ and MER $= 1.06 \times 10^{13}\,\mathrm{g\,h^{-1}}$. The panels on the left are for the minimum source area, and the panels on the right are for the maximum. The area and orientation of the two source geometries are compared in relation to each other next to the parameter list at the top of the figure. For each area, four outputs are presented at different times after the eruption start t_0: **(a & e)** $7\,\mathrm{h}$, **(b & f)** $13\,\mathrm{h}$, **(c & g)** $18\,\mathrm{h}$, and **(d & h)** $23\,\mathrm{h}$. Total column mass loadings are averaged over the previous hour, and we applied a threshold of $0.2\,\mathrm{g\,m^{-2}}$.

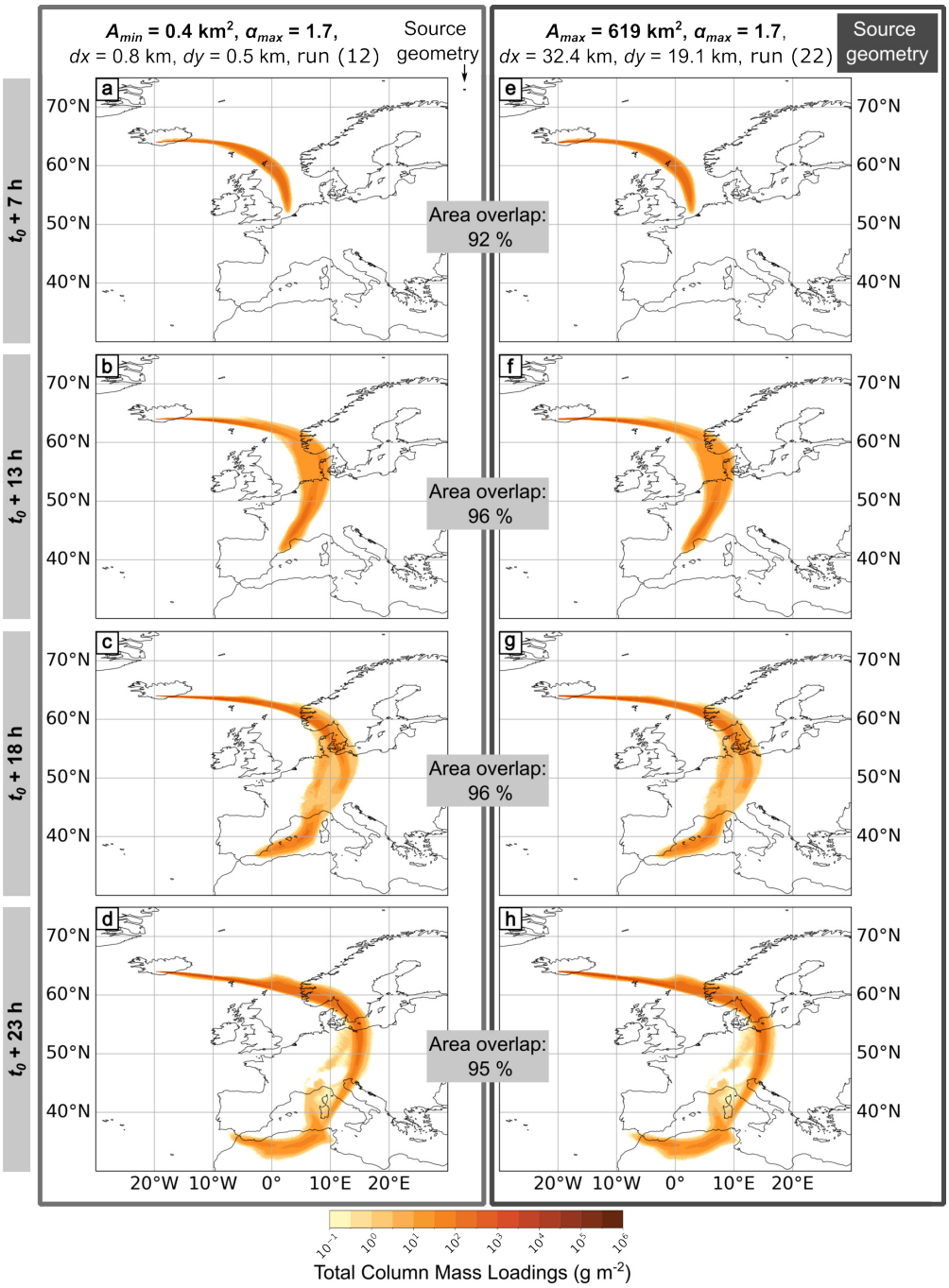

Figure A.9: NAME outputs for numerical experiment 1, all using $\alpha_{max} = 1.7$, a $24\,\mathrm{h}$ particle release, $z = 8.5\,\mathrm{km}$, $dz = 3\,\mathrm{km}$ and MER $= 1.06 \times 10^{13}\,\mathrm{g\,h^{-1}}$. The panels on the left are for the minimum source area, and the panels on the right are for the maximum. The area and orientation of the two source geometries are compared in relation to each other next to the parameter list at the top of the figure. For each area, four outputs are presented at different times after the eruption start t_0: **(a & e)** $7\,\mathrm{h}$, **(b & f)** $13\,\mathrm{h}$, **(c & g)** $18\,\mathrm{h}$, and **(d & h)** $23\,\mathrm{h}$. Total column mass loadings are averaged over the previous hour, and we applied a threshold of $0.2\,\mathrm{g\,m^{-2}}$.

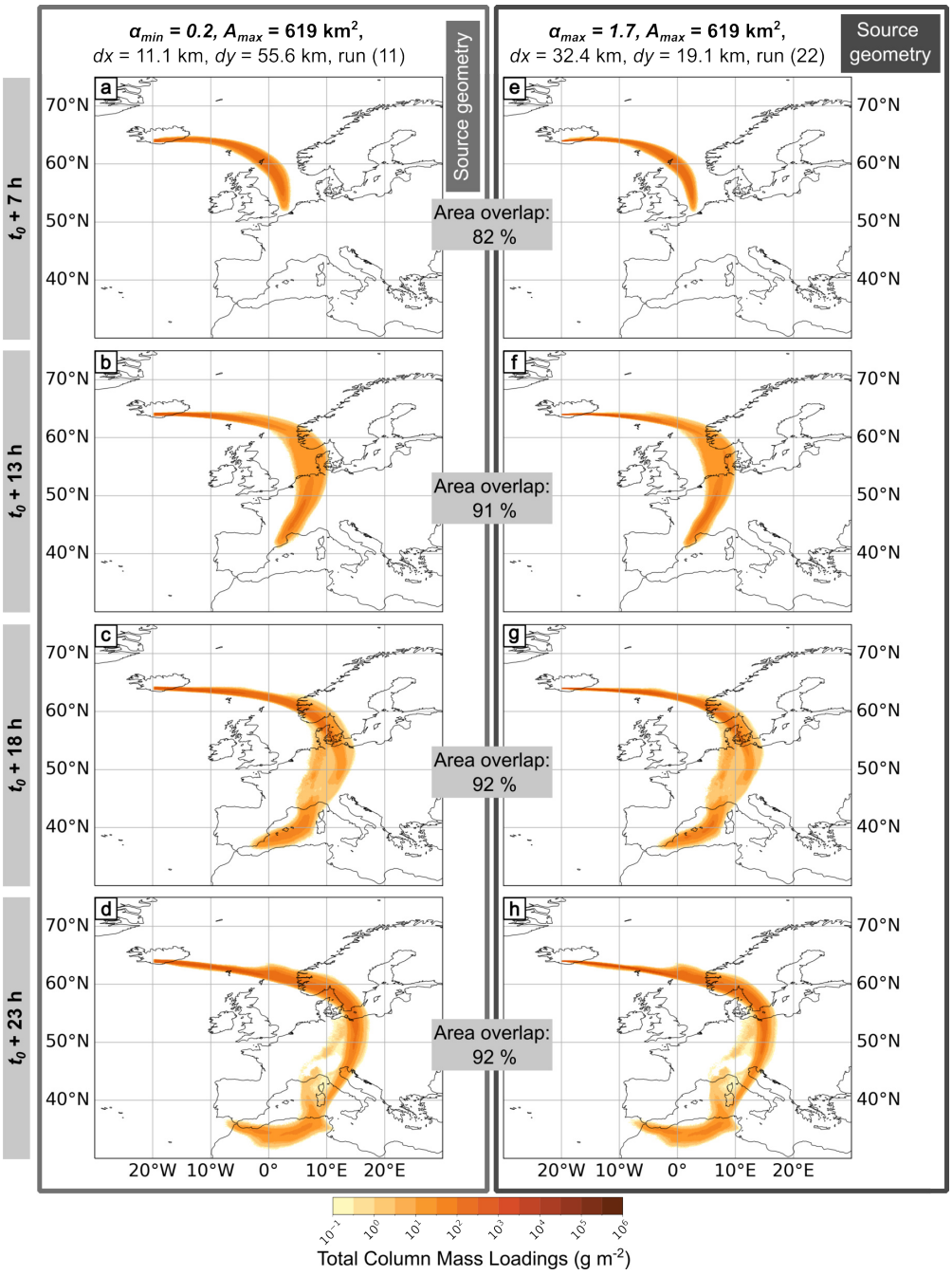

Figure A.10: NAME model outputs for numerical experiment 1, all using $A_{max} = 619\,\mathrm{km}^2$, a $24\,\mathrm{h}$ particle release, $z = 8.5\,\mathrm{km}$, $dz = 3\,\mathrm{km}$ and MER $= 1.06 \times 10^{13}\,\mathrm{g\,h^{-1}}$. The left figure panels **(a-d)** show results from the minimum aspect ratio $\alpha_{min} = 0.2$, and the right panels **(e-h)** show the maximum aspect ratio $\alpha_{max} = 1.7$. The area and orientation of the two source geometries are compared in relation to each other next to the parameter list at the top of the figure. For each aspect ratio, four outputs at different times after eruption start t_0 are shown: **(a & e)** $7\,\mathrm{h}$, **(b & f)** $13\,\mathrm{h}$, **(c & g)** $18\,\mathrm{h}$, and **(d & h)** $23\,\mathrm{h}$. Total column mass loadings are averaged over the previous hour, and we applied a threshold of $0.2\,\mathrm{g\,m^{-2}}$.

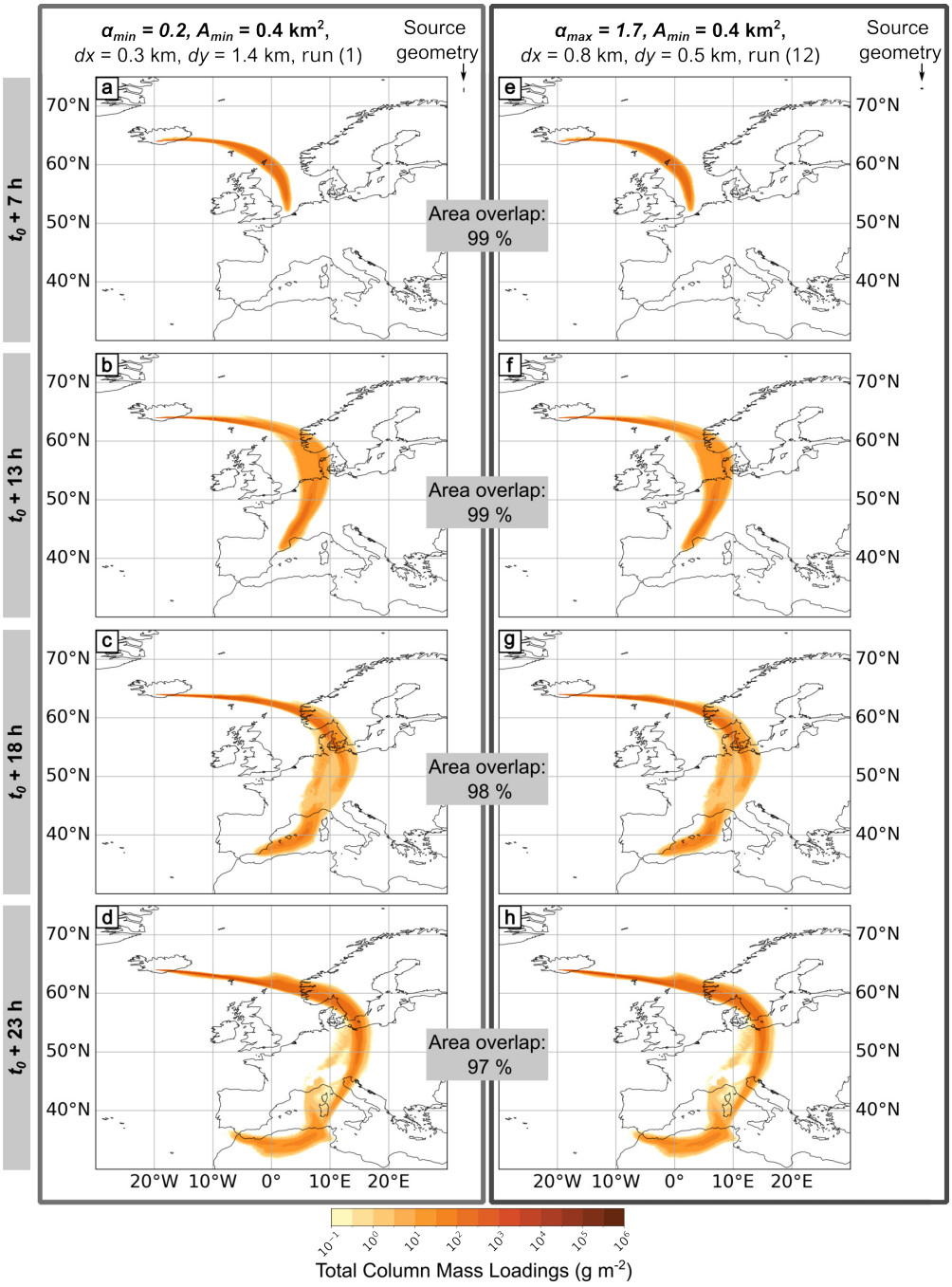

Figure A.11: NAME model outputs for numerical experiment 1, all using $A_{min} = 0.4\,\mathrm{km}^2$, a $24\,\mathrm{h}$ particle release, $z = 8.5\,\mathrm{km}$, $dz = 3\,\mathrm{km}$ and MER $= 1.06 \times 10^{13}\,\mathrm{g\,h^{-1}}$. The left figure panels **(a-d)** show results from the minimum aspect ratio $\alpha_{min} = 0.2$, and the right panels **(e-h)** show the maximum aspect ratio $\alpha_{max} = 1.7$. The area and orientation of the two source geometries are compared in relation to each other next to the parameter list at the top of the figure. For each aspect ratio, four outputs at different times after eruption start t_0 are shown: **(a & e)** $7\,\mathrm{h}$, **(b & f)** $13\,\mathrm{h}$, **(c & g)** $18\,\mathrm{h}$, and **(d & h)** $23\,\mathrm{h}$. Total column mass loadings are averaged over the previous hour, and we applied a threshold of $0.2\,\mathrm{g\,m^{-2}}$.

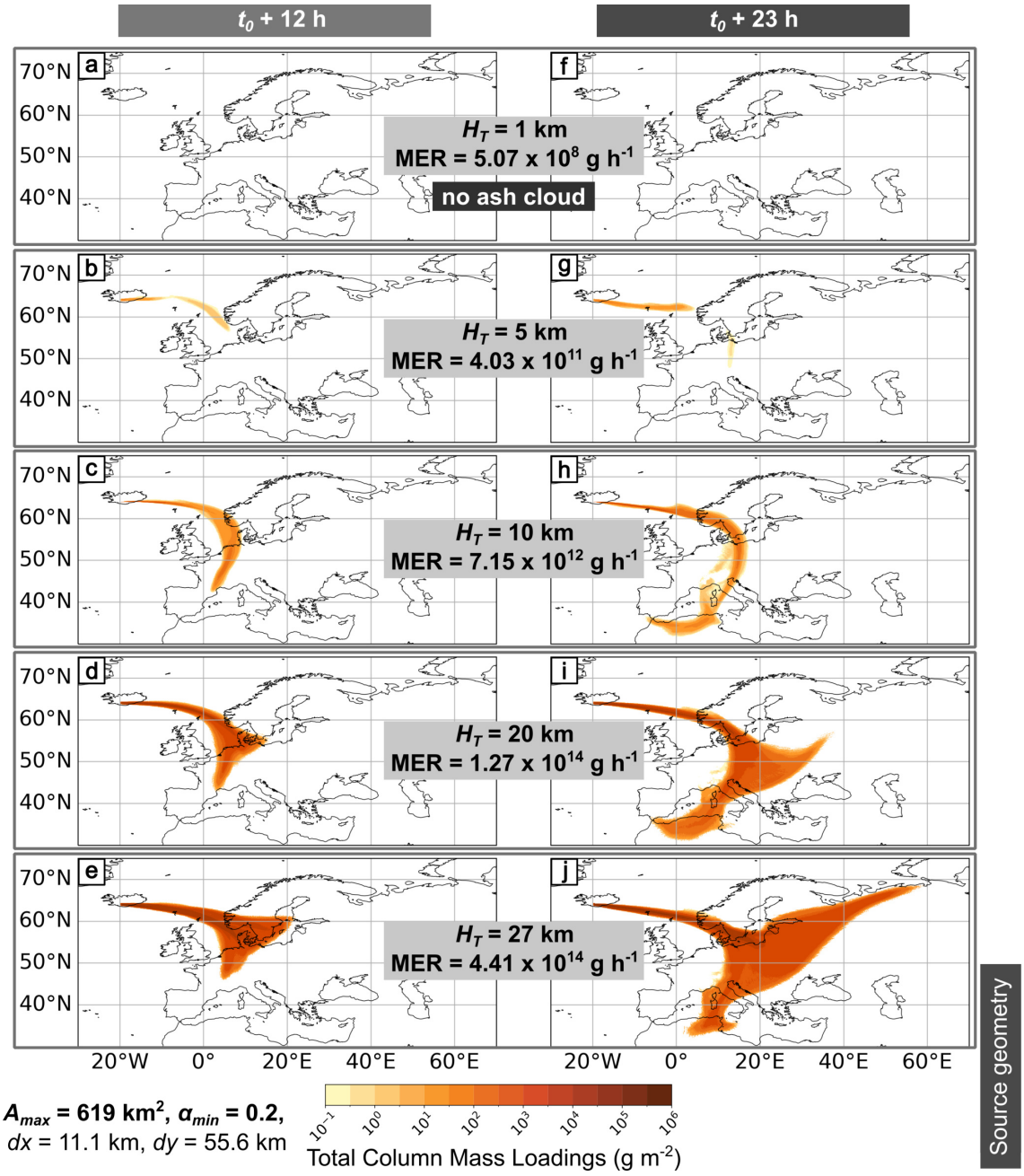

Figure A.12: NAME model outputs for experiment 2, all using a $24\,\mathrm{h}$ particle release with different H_T, MER, and *dz*. The figure panels on the left **(a-d)** are for $12\,\mathrm{h}$ after eruption start t_0, and the panels on the right **(e-h)** show $23\,\mathrm{h}$ after eruption start t_0. The outputs here are for $A_{max} = 619\,\mathrm{km}^2$ with $\alpha_{min} = 0.2$. With increasing H_T and *t* (h), the plume size grows. Total column mass loadings are averaged over the previous hour, and we applied a threshold of $0.2\,\mathrm{g\,m^{-2}}$. The subplots **(a & f)** show no ash cloud (i.e., mass loading $< 0.2\,\mathrm{g\,m^{-2}}$).

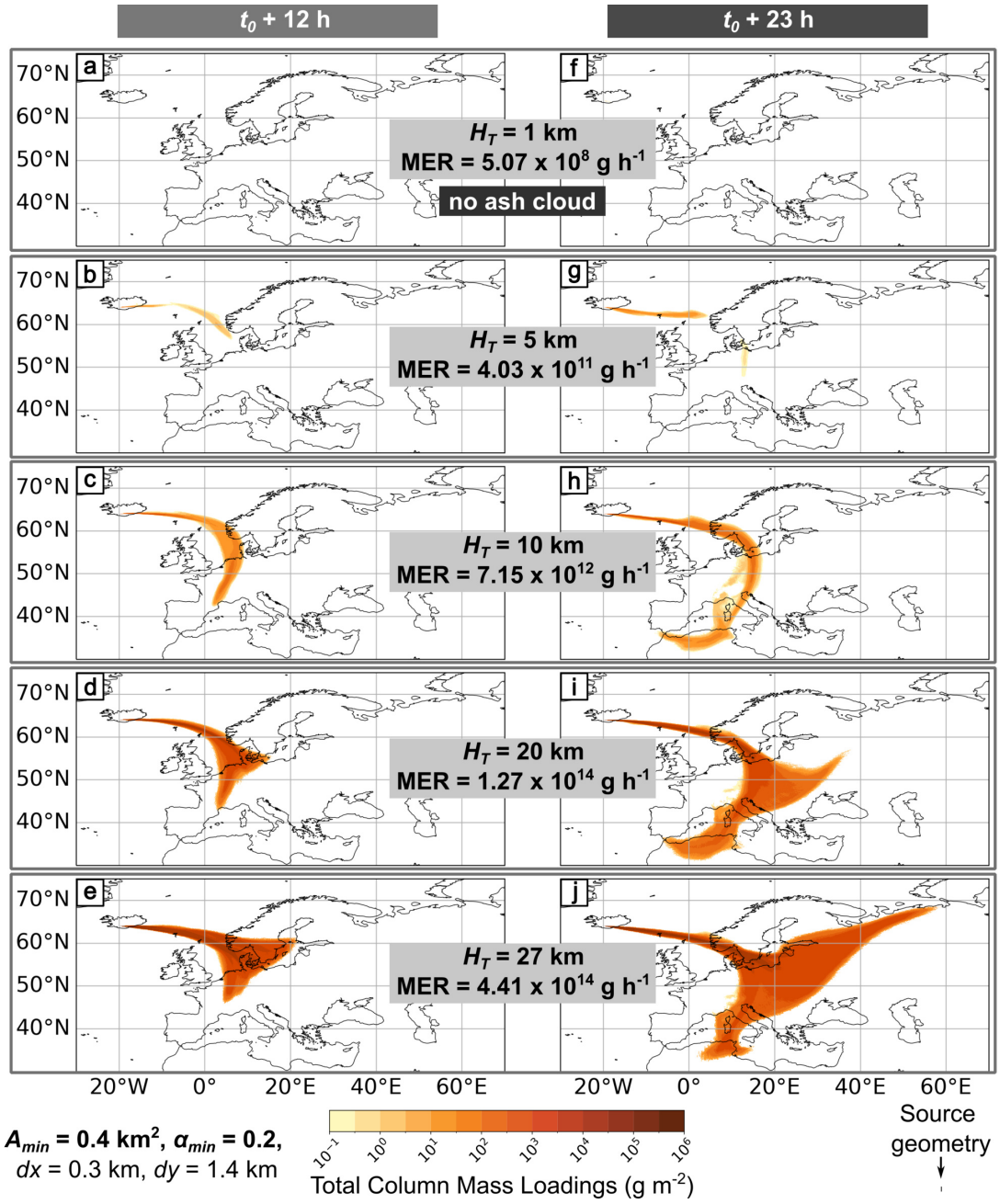

Figure A.13: NAME model outputs for experiment 2, all using a $24\,\mathrm{h}$ particle release different H_T, MER, and *dz*. The figure panels on the left **(a-d)** are for $12\,\mathrm{h}$ after eruption start t_0, and the panels on the right **(e-h)** show $23\,\mathrm{h}$ after eruption start t_0. The outputs here are for $A_{min} = 0.4\,\mathrm{km}^2$ with $\alpha_{min} = 0.2$. With increasing H_T and t (h), the plume size grows. Total column mass loadings are averaged over the previous hour, and we applied a threshold of $0.2\,\mathrm{g\,m^{-2}}$. The subplots **(a & f)** show no ash cloud (i.e., mass loading $< 0.2\,\mathrm{g\,m^{-2}}$).

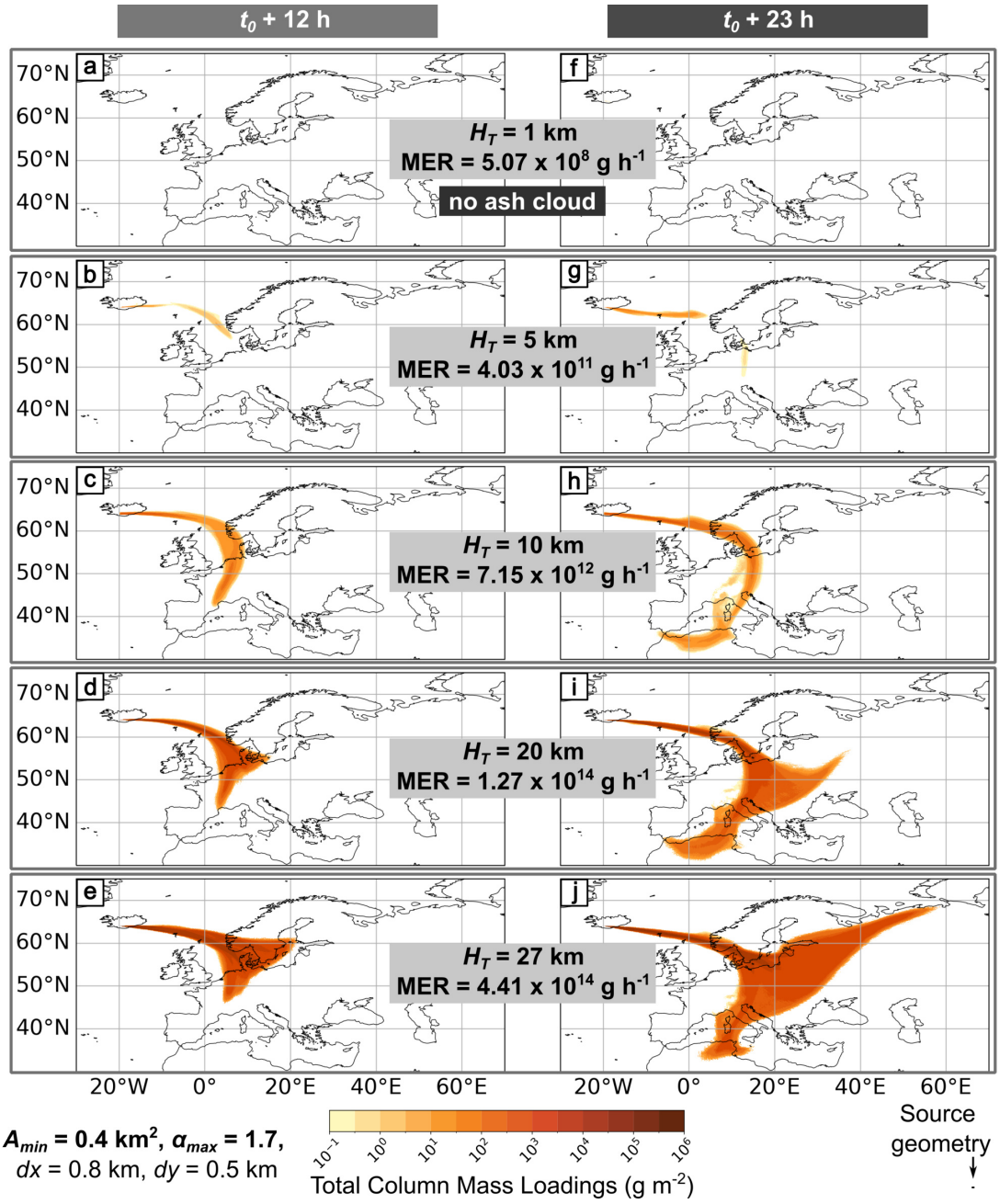

Figure A.14: NAME model outputs for experiment 2, all using a $24\,\mathrm{h}$ particle release different H_T, MER, and *dz*. The figure panels on the left **(a-d)** are for $12\,\mathrm{h}$ after eruption start t0, and the panels on the right **(e-h)** show $23\,\mathrm{h}$ after eruption start t_0. The outputs here are for $A_{min} = 0.4\,\mathrm{km}^2$ with $\alpha_{max} = 1.7$. With increasing H_T and t (h), the plume size grows. Total column mass loadings are averaged over the previous hour, and we applied a threshold of $0.2\,\mathrm{g\,m^{-2}}$. The subplots **(a & f)** show no ash cloud (i.e., mass loading $< 0.2\,\mathrm{g\,m^{-2}}$).

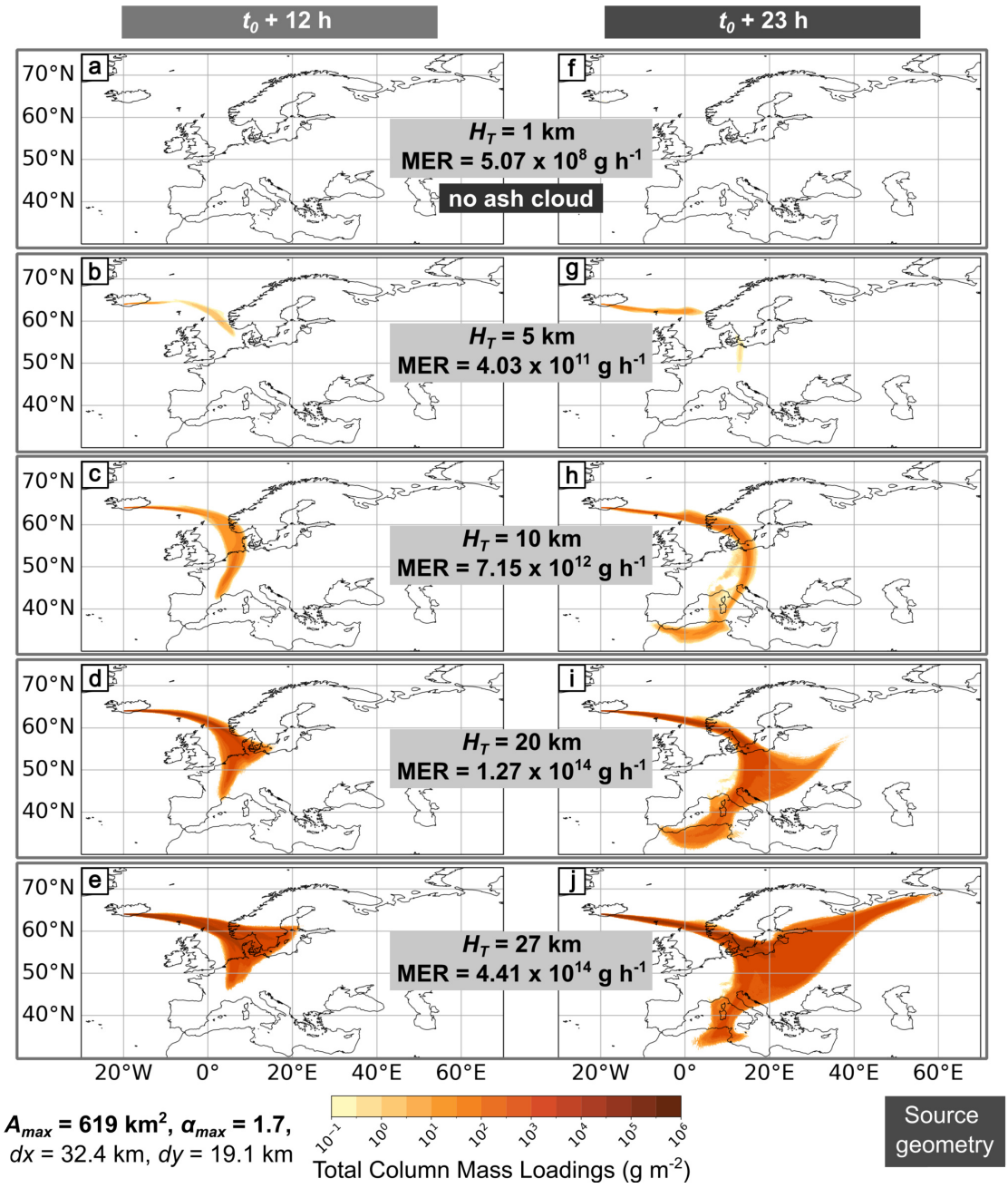

Figure A.15: NAME model outputs for experiment 2, all using a $24\,\mathrm{h}$ particle release different H_T, MER, and *dz*. The figure panels on the left **(a-d)** are for $12\,\mathrm{h}$ after eruption start t_0, and the panels on the right **(e-h)** show $23\,\mathrm{h}$ after eruption start t_0. The outputs here are for $A_{max} = 619\,\mathrm{km}^2$ with $\alpha_{max} = 1.7$. With increasing H_T and *t* (h), the plume size grows. Total column mass loadings are averaged over the previous hour, and we applied a threshold of $0.2\,\mathrm{g\,m^{-2}}$. The subplots **(a & f)** show no ash cloud (i.e., mass loading $< 0.2\,\mathrm{g\,m^{-2}}$).

B. The ash concentration of co-PDC clouds

Table B.1 provides an overview of the dates used per weather pattern within. Figure B.1 - Figure B.4 are for completeness to display the whole range of vertical extent of this study.

Table B.1: Dates manually chosen per weather pattern. Each weather pattern covers three different seasons and is chosen from the extent of *UMG_Mk10PT*.

Weather pattern	Day	Month	Year
1	28	2	2018
	9	5	2020
	25	12	2021
2	3	8	2017
	11	3	2019
	16	11	2020
3	11	12	2017
	25	5	2019
	31	1	2022
4	29	11	2018
	16	1	2020
	6	9	2021
5	27	6	2018
	18	11	2019
	16	4	2022
6	30	8	2018
	31	5	2019
	18	1	2021
7	13	6	2017
	22	7	2019
	6	10	2021
8	31	10	2017
	7	9	2020
	22	6	2021

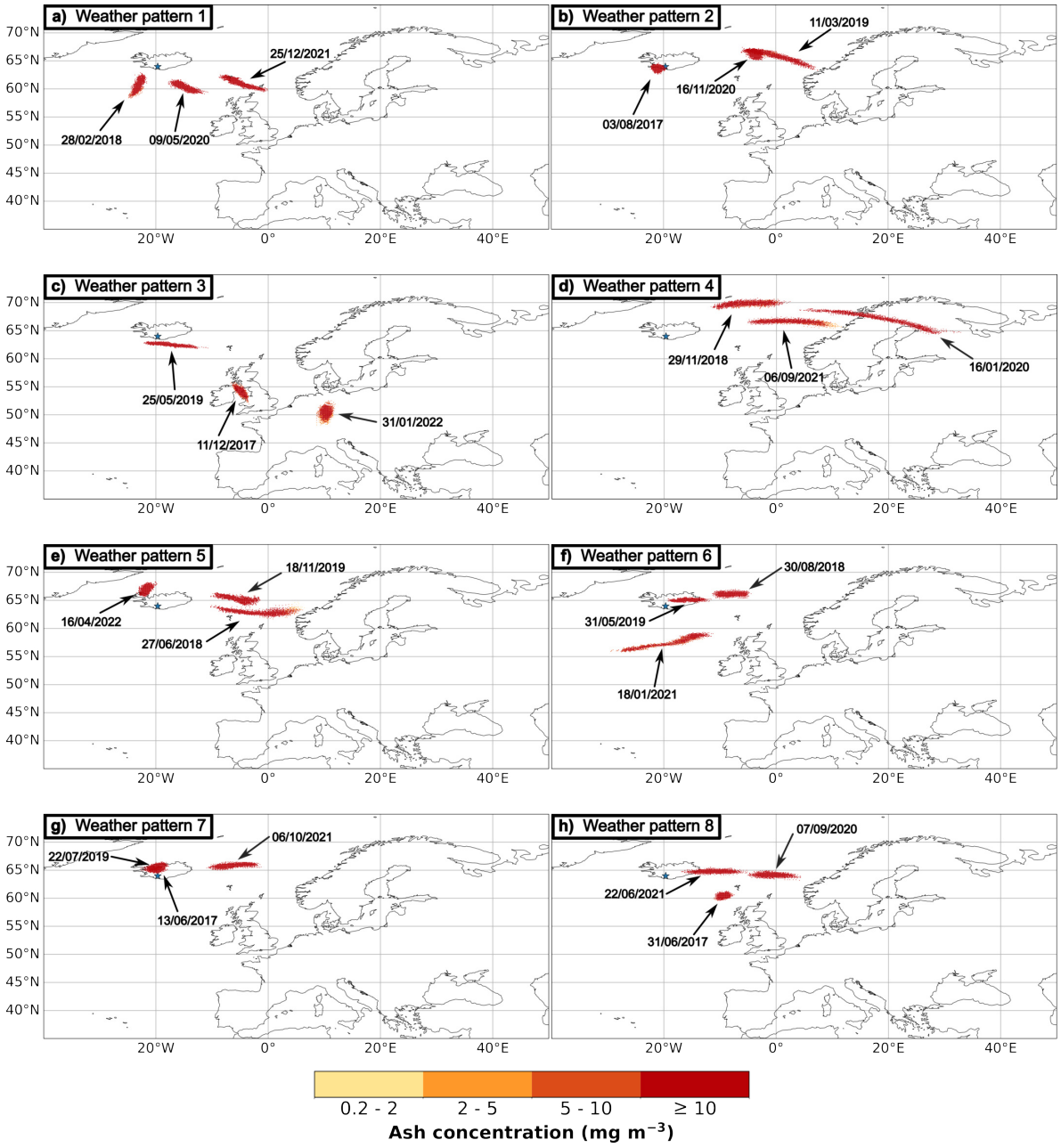

Figure B.1: Ash cloud location displayed for the eight weather patterns at $12\,\mathrm{h}$ after particle release at FL300 - FL350 (included in the commercial plane range). Each subfigure contains three NAME model outputs, and thus three different ash clouds generated for each weather pattern. Some of the ash clouds within a weather pattern slightly overlap in this figure. In all panels, a blue star indicates the release location. The data are given as ash concentration in $\mathrm{mg\,m^{-3}}$.

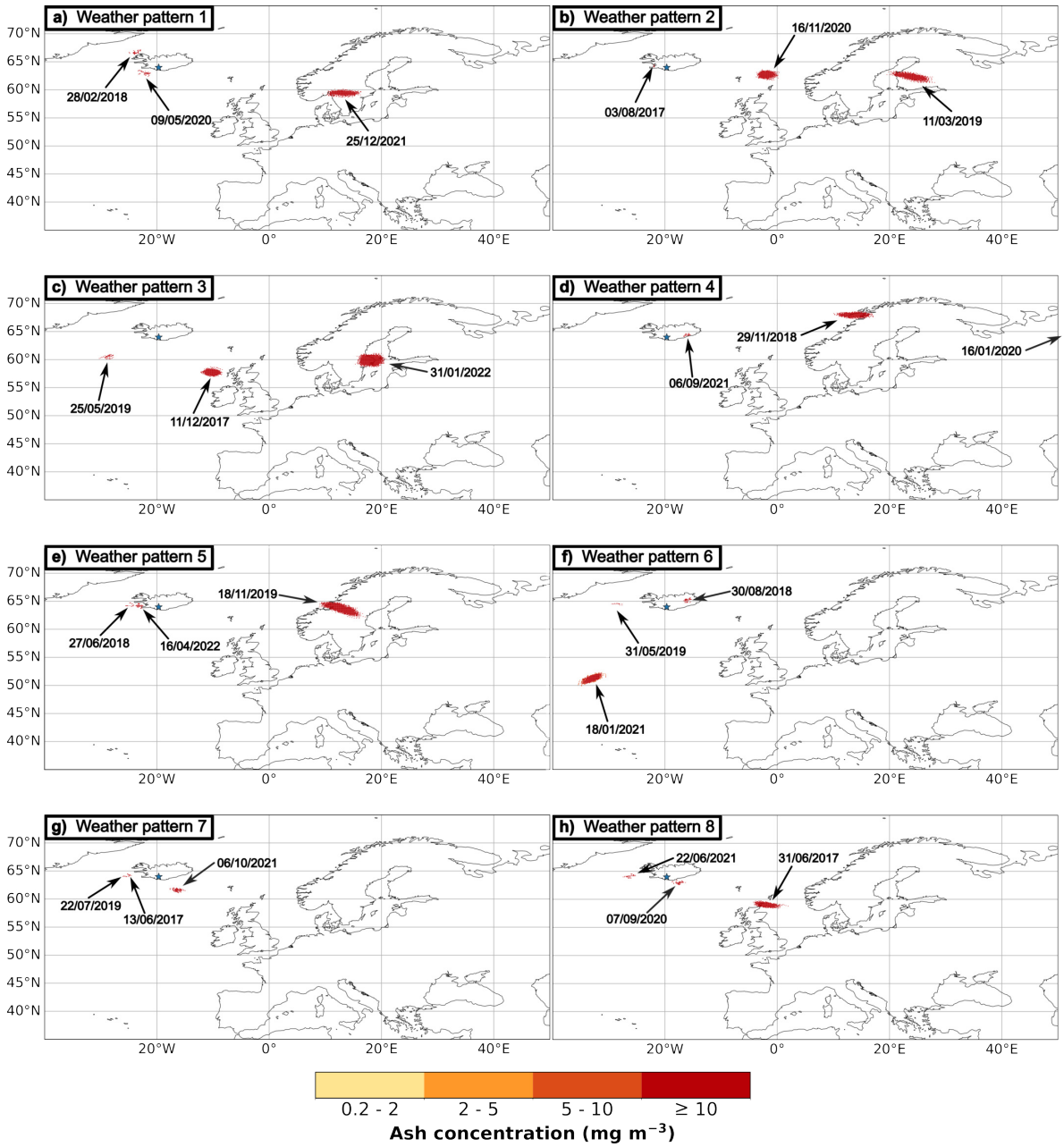

Figure B.2: Ash cloud location displayed for the eight weather patterns at $12\,\mathrm{h}$ after particle release at FL900 - FL950. Each subfigure contains three NAME model outputs, and thus three different ash clouds generated for each weather pattern. Some of the ash clouds within a weather pattern slightly overlap in this figure. In all panels, a blue star indicates the release location. The data are given as ash concentration in $\mathrm{mg\,m^{-3}}$.

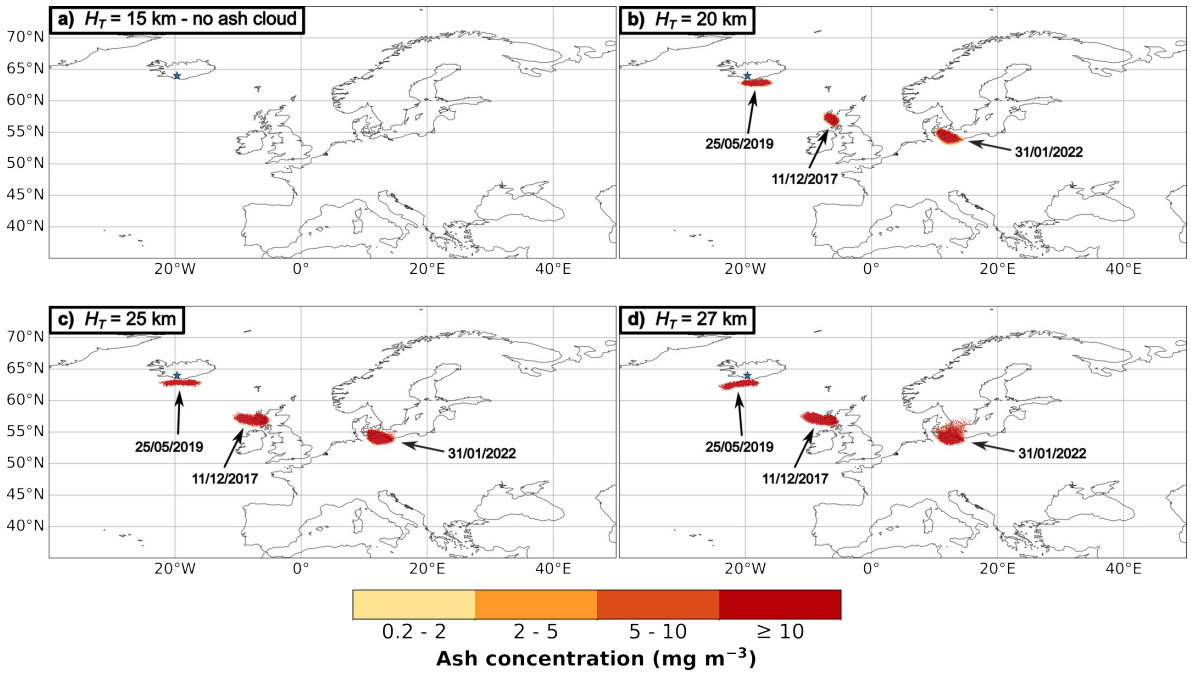

Figure B.3: Ash cloud locations at FL550- FL600 for particle release heights of **(a)** $H_T = 15\,\mathrm{km}$, **(b)** $H_T = 20\,\mathrm{km}$, **(c)** $H_T = 25\,\mathrm{km}$, and **(d)** $H_T = 27\,\mathrm{km}$ for the weather pattern number 3 at $12\,\mathrm{h}$ since start time. Subfigure **(a)** does not have an ash cloud as ash particles were not dispersed at this altitude. Each subfigure **(b - d)** shows three different model run outputs for different dates. In all panels, a blue star indicates the release location. The data are given as ash concentration in $\mathrm{mg\,m^{-3}}$.

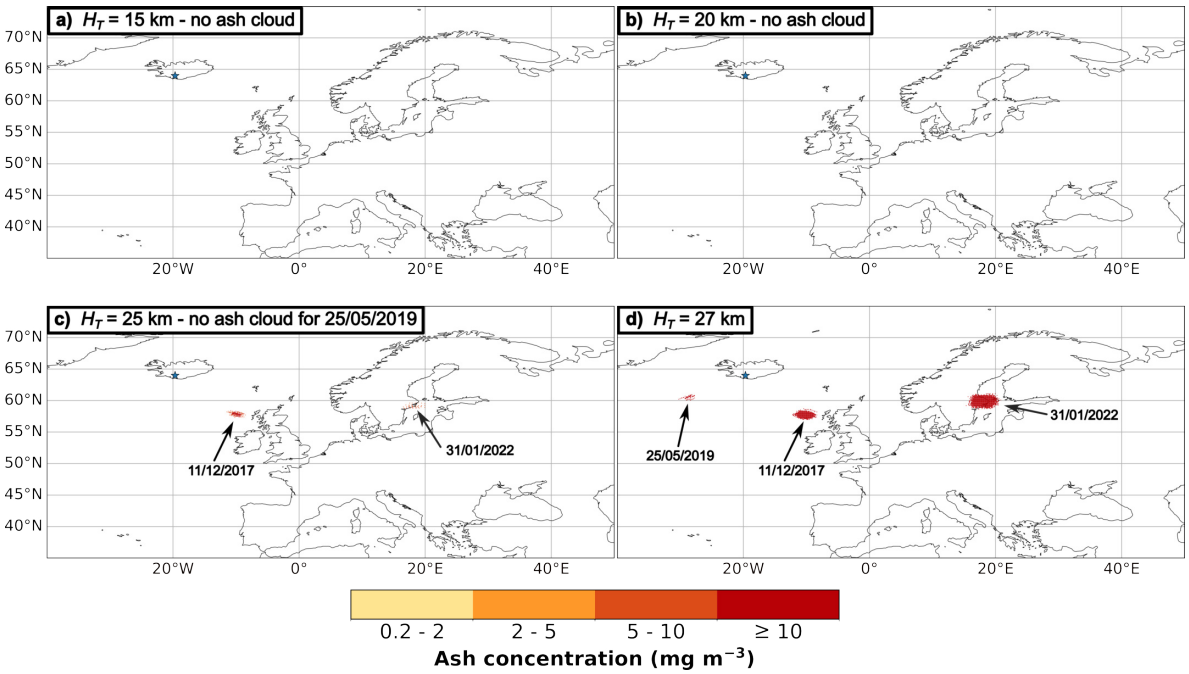

Figure B.4: Ash cloud locations at FL900 - FL950 for particle release heights **(a)** $H_T = 15\,\mathrm{km}$, **(b)** $H_T = 20\,\mathrm{km}$, **(c)** $H_T = 25\,\mathrm{km}$, and **(d)** $H_T = 27\,\mathrm{km}$ for the weather pattern number 3 at $12\,\mathrm{h}$ since start time. **(a & b)** have no ash cloud as ash particles were not dispersed at these altitudes. Each subfigure **(c & d)** shows three different model run outputs for different dates. In all panels, a blue star indicates the release location. The data are given as ash concentration in $\mathrm{mg\,m^{-3}}$.

References

Abdalla, S., Isaksen, L., Janssen, P., & Wedi, N. (2013). Effective spectral resolution of ECMWF atmospheric forecast models. *ECMWF Newsletter: Meteorology*, *137*, 19–22. https://doi.org/10.21957/rue4o7ac

Alexander, D. (2013). Volcanic ash in the atmosphere and risks for civil aviation: A study in European crisis management. *International Journal of Disaster Risk Science*, *4*(1), 9–19. https://doi.org/10.1007/s13753-013-0003-0

Andrews, B. J. (2014). Dispersal and air entrainment in unconfined dilute pyroclastic density currents. *Bulletin of Volcanology*, *76*(9), 852. https://doi.org/10.1007/s00445-014-0852-4

Andrews, B. J., & Manga, M. (2011). Effects of topography on pyroclastic density current runout and formation of coignimbrites. *Geology*, *39*(12), 1099–1102. https://doi.org/10.1130/G32226.1

Andrews, B. J., & Manga, M. (2012). Experimental study of turbulence, sedimentation, and coignimbrite mass partitioning in dilute pyroclastic density currents. *Journal of Volcanology and Geothermal Research*, *225-226*, 30–44. https://doi.org/10.1016/j.jvolgeores.2012.02.011

Aubry, T. J., Engwell, S. L., Bonadonna, C., Carazzo, G., Scollo, S., Van Eaton, A. R., Taylor, I. A., Jessop, D., Eychenne, J., Gouhier, M., Mastin, L. G., Wallace, K. L., Biass, S., Bursik, M., Grainger, R. G., Jellinek, A. M., & Schmidt, A. (2021). The Independent Volcanic Eruption Source Parameter Archive (IVESPA, version 1.0): A new observational database to support explosive eruptive column model validation and development. *Journal of Volcanology and Geothermal Research*, *417*, 107295. https://doi.org/10.1016/j.jvolgeores.2021.107295

Aubry, T. J., Engwell, S. L., Bonadonna, C., Mastin, L. G., Carazzo, G., Van Eaton, A. R., Jessop, D. E., Grainger, R. G., Scollo, S., Taylor, I. A., Jellinek, A. M., Schmidt, A., Biass, S., & Gouhier, M. (2023). New Insights Into the Relationship Between Mass Eruption Rate and Volcanic Column Height Based On the IVESPA Data Set.

Geophysical Research Letters, *50*(14), e2022GL102633. https://doi.org/10.1029/2022GL102633

Beckett, F. M., Bensimon, D., Crawford, A., Deslandes, M., Guidard, V., Hort, M., Jeoffrion, M., Kristiansen, N., Lucas, C., Nishijo, A., Osores, S., Renard, E., Servranckx, G., Snee, E., Trancoso, R., & Vazquez, E. (2024). VAAC Model Setup Tables 2023. https://doi.org/10.5281/zenodo.10671098

Beckett, F. M., Witham, C. S., Hort, M. C., Stevenson, J. A., Bonadonna, C., & Millington, S. C. (2015). Sensitivity of dispersion model forecasts of volcanic ash clouds to the physical characteristics of the particles. *Journal of Geophysical Research: Atmospheres*, *120*(22), 11, 636–11, 652. https://doi.org/10.1002/2015JD023609

Beckett, F. M., Witham, C. S., Leadbetter, S. J., Crocker, R., Webster, H. N., Hort, M. C., Jones, A. R., Devenish, B. J., & Thomson, D. J. (2020). Atmospheric Dispersion Modelling at the London VAAC: A Review of Developments since the 2010 Eyjafjallajökull Volcano Ash Cloud. *Atmosphere*, *11*(4), 352. https://doi.org/10.3390/atmos11040352

Bernard, A., & Rose, W. I. (1990). The injection of sulfuric acid aerosols in the stratosphere by the El Chichón volcano and its related hazards to the international air traffic. *Natural Hazards*, *3*(1), 59–67. https://doi.org/10.1007/BF00144974

Biass, S., Bonadonna, C., Connor, L., & Connor, C. (2016). TephraProb: a Matlab package for probabilistic hazard assessments of tephra fallout. *Journal of Applied Volcanology*, *5*(1), 10. https://doi.org/10.1186/s13617-016-0050-5

Bonadonna, C., Macedonio, G., & Sparks, R. S. J. (2002). Numerical modelling of tephra fallout associated with dome collapses and Vulcanian explosions: application to hazard assessment on Montserrat. *Geological Society, London, Memoirs*, *21*(1), 517–537. https://doi.org/10.1144/GSL.MEM.2002.021.01.23

Bonadonna, C., Mayberry, G. C., Calder, E. S., Sparks, R. S. J., Choux, C., Jackson, P., Lejeune, A. M., Loughlin, S. C., Norton, G. E., Rose, W. I., Ryan, G., & Young, S. R. (2002). Tephra fallout in the eruption of Soufrière Hills Volcano, Montserrat. In T. H. Druitt & B. P. Kokelaar (Eds.), *The eruption of soufrière hills volcano, montserrat from 1995 to 1999* (pp. 483–516, Vol. 21). Geological Society of London. https://doi.org/10.1144/GSL.MEM.2002.021.01.22

Bonadonna, C., & Phillips, J. C. (2003). Sedimentation from strong volcanic plumes. *Journal of Geophysical Research: Solid Earth*, *108*, 2340. https://doi.org/10.1029/2002JB002034

Brown, A., Milton, S., Cullen, M., Golding, B., Mitchell, J., & Shelly, A. (2012). Unified Modeling and Prediction of Weather and Climate: A 25-Year Journey. *Bulletin of*

the American Meteorological Society, *93*(12), 1865–1877. https://doi.org/10.1175/BAMS-D-12-00018.1

Brown, R. J., Bonadonna, C., & Durant, A. J. (2012). A review of volcanic ash aggregation. *Physics and Chemistry of the Earth, Parts A/B/C*, *45-46*, 65–78. https://doi.org/10.1016/j.pce.2011.11.001

Brown, R. J., & Andrews, G. D. M. (2015). Chapter 36 - Deposits of Pyroclastic Density Currents. In H. Sigurdsson (Ed.), *The encyclopedia of volcanoes (second edition)* (pp. 631–648). Academic Press. https://doi.org/10.1016/B978-0-12-385938-9.00036-5

Burgisser, A., Peccia, A., Plank, T., & Moussallam, Y. (2024). Numerical simulations of the latest caldera-forming eruption of Okmok volcano, Alaska. *Bulletin of Volcanology*, *86*(9), 77. https://doi.org/10.1007/s00445-024-01765-1

Bursik, M. (2001). Effect of wind on the rise height of volcanic plumes. *Geophysical Research Letters*, *28*(18), 3621–3624. https://doi.org/10.1029/2001GL013393

Bursik, M., & Woods, A. W. (1996). The dynamics and thermodynamics of large ash flows. *Bulletin of Volcanology*, *58*(2), 175–193. https://doi.org/10.1007/s004450050134

Calder, E. S., Sparks, R. S. J., & Woods, A. W. (1997). Dynamics of co-ignimbrite plumes generated from pyroclastic flows of Mount St. Helens (7 August 1980). *Bulletin of Volcanology*, *58*(6), 432–440. https://doi.org/10.1007/s004450050151

Carey, S. N., & Bursik, M. (2015). Chapter 32 - Volcanic Plumes. In H. Sigurdsson (Ed.), *The encyclopedia of volcanoes (second edition)* (pp. 571–585). Academic Press. https://doi.org/10.1016/B978-0-12-385938-9.00032-8

Carey, S. N., & Sparks, R. S. J. (1986). Quantitative models of the fallout and dispersal of tephra from volcanic eruption columns. *Bulletin of Volcanology*, *48*(2), 109–125. https://doi.org/10.1007/BF01046546

Casadevall, T. J. (1993). *Volcanic hazards and aviation safety: lessons of the past decade.* Flight safety foundation, flight safety digest. https://flightsafety.org/fsd/fsd_may93.pdf

Casadevall, T. J., Delos Reyes, P. J., & Schneider, D. J. (1999). *The 1991 Pinatubo Eruptions and Their Effects on Aircraft Operations*. United States Geological Survey. Retrieved April 30, 2025, from https://pubs.usgs.gov/pinatubo/casa/

Charbonnier, S. J., & Gertisser, R. (2008). Field observations and surface characteristics of pristine block-and-ash flow deposits from the 2006 eruption of Merapi Volcano, Java, Indonesia. *Journal of Volcanology and Geothermal Research*, *177*(4), 971–982. https://doi.org/10.1016/j.jvolgeores.2008.07.008

Chen, W. R., & Zhao, L. R. (2015). Review – Volcanic Ash and its Influence on Aircraft Engine Components. *Procedia Engineering*, *99*, 795–803. https://doi.org/10.1016/j.proeng.2014.12.604

Christmann, C., Nunes, R., Schmitt, A., & Guffanti, M. (2017). Flying into Volcanic Ash Clouds: An Evaluation of Hazard Potential. https://www.sto.nato.int/document/flying-into-volcanic-ash-clouds-an-evaluation-of-hazard-potential/

Clarkson, R. J., Majewicz, E. J., & Mack, P. (2016). A re-evaluation of the 2010 quantitative understanding of the effects volcanic ash has on gas turbine engines. *Proceedings of the Institution of Mechanical Engineers, Part G*, *230*(12), 2274–2291. https://doi.org/10.1177/0954410015623372

Constantinescu, R., Hopulele-Gligor, A., Connor, C. B., Bonadonna, C., Connor, L. J., Lindsay, J. M., Charbonnier, S., & Volentik, A. C. M. (2021). The radius of the umbrella cloud helps characterize large explosive volcanic eruptions. *Communications Earth & Environment*, *2*(1), 3. https://doi.org/10.1038/s43247-020-00078-3

Corradini, S., Montopoli, M., Guerrieri, L., Ricci, M., Scollo, S., Merucci, L., Marzano, F. S., Pugnaghi, S., Prestifilippo, M., Ventress, L. J., Grainger, R. G., Carboni, E., Vulpiani, G., & Coltelli, M. (2016). A Multi-Sensor Approach for Volcanic Ash Cloud Retrieval and Eruption Characterization: The 23 November 2013 Etna Lava Fountain. *Remote Sensing*, *8*(1), 58. https://doi.org/10.3390/rs8010058

Dacre, H. F., Grant, A. L. M., Harvey, N. J., Thomson, D. J., Webster, H. N., & Marenco, F. (2015). Volcanic ash layer depth: Processes and mechanisms. *Geophysical Research Letters*, *42*(2), 637–645. https://doi.org/10.1002/2014GL062454

Dacre, H. F., Grant, A. L. M., Hogan, R. J., Belcher, S. E., Thomson, D. J., Devenish, B. J., Marenco, F., Hort, M. C., Haywood, J. M., Ansmann, A., Mattis, I., & Clarisse, L. (2011). Evaluating the structure and magnitude of the ash plume during the initial phase of the 2010 Eyjafjallajökull eruption using lidar observations and NAME simulations. *Journal of Geophysical Research: Atmospheres*, *116*, D00U03. https://doi.org/10.1029/2011JD015608

Dai, A. (2023). The diurnal cycle from observations and ERA5 in surface pressure, temperature, humidity, and winds. *Climate Dynamics*, *61*(5), 2965–2990. https://doi.org/10.1007/s00382-023-06721-x

Dang, R., Yang, Y., Hu, X.-M., Wang, Z., & Zhang, S. (2019). A Review of Techniques for Diagnosing the Atmospheric Boundary Layer Height (ABLH) Using Aerosol Lidar Data. *Remote Sensing*, *11*(13), 1590. https://doi.org/10.3390/rs11131590

Davies, T., Cullen, M. J. P., Malcolm, A. J., Mawson, M. H., Staniforth, A., White, A. A., & Wood, N. (2005). A new dynamical core for the Met Office's global and regional

modelling of the atmosphere. *Quarterly Journal of the Royal Meteorological Society*, *131*(608), 1759–1782. https://doi.org/10.1256/qj.04.101

Del Bello, E., Taddeucci, J., Merrison, J. P., Rasmussen, K. R., Andronico, D., Ricci, T., Scarlato, P., & Iversen, J. J. (2021). Field-based measurements of volcanic ash resuspension by wind. *Earth and Planetary Science Letters*, *554*, 116684. https://doi.org/10.1016/j.epsl.2020.116684

Dellino, P., Dioguardi, F., Isaia, R., Sulpizio, R., & Mele, D. (2021). The impact of pyroclastic density currents duration on humans: the case of the AD 79 eruption of Vesuvius. *Scientific Reports*, *11*(1), 4959. https://doi.org/10.1038/s41598-021-84456-7

Devenish, B. J. (2013). Using simple plume models to refine the source mass flux of volcanic eruptions according to atmospheric conditions. *Journal of Volcanology and Geothermal Research*, *256*, 118–127. https://doi.org/10.1016/j.jvolgeores.2013.02.015

Devenish, B. J., Francis, P. N., Johnson, B. T., Sparks, R. S. J., & Thomson, D. J. (2012). Sensitivity analysis of dispersion modeling of volcanic ash from Eyjafjallajökull in May 2010. *Journal of Geophysical Research: Atmospheres*, *117*, D00U21. https://doi.org/10.1029/2011JD016782

Dioguardi, F., Beckett, F., Dürig, T., & Stevenson, J. A. (2020). The Impact of Eruption Source Parameter Uncertainties on Ash Dispersion Forecasts During Explosive Volcanic Eruptions. *Journal of Geophysical Research: Atmospheres*, *125*(17), e2020JD032717. https://doi.org/10.1029/2020JD032717

Đorđević, D., Vukmirović, Z., Tošić, I., & Unkašević, M. (2004). Contribution of dust transport and resuspension to particulate matter levels in the Mediterranean atmosphere. *Atmospheric Environment*, *38*(22), 3637–3645. https://doi.org/10.1016/j.atmosenv.2004.04.001

Druitt, T. H. (1998). Pyroclastic density currents. *Geological Society, London, Special Publications*, *145*(1), 145–182. https://doi.org/10.1144/GSL.SP.1996.145.01.08

Druitt, T. H., Young, S. R., Baptie, B., Bonadonna, C., Calder, E. S., Clarke, A. B., Cole, P. D., Harford, C. L., Herd, R. A., Luckett, R., Ryan, G., & Voight, B. (2002). Episodes of cyclic Vulcanian explosive activity with fountain collapse at Soufrière Hills Volcano, Montserrat. *Geological Society, London, Memoirs*, *21*(1), 281–306. https://doi.org/10.1144/GSL.MEM.2002.021.01.13

Dufek, J., Esposti Ongaro, T., & Roche, O. (2015). Chapter 35 - Pyroclastic Density Currents: Processes and Models. In H. Sigurdsson (Ed.), *The encyclopedia of volcanoes (second edition)* (pp. 617–629). Academic Press. https://doi.org/10.1016/B978-0-12-385938-9.00035-3

Durant, A. J., Bonadonna, C., & Horwell, C. J. (2010). Atmospheric and Environmental Impacts of Volcanic Particulates. *Elements*, *6*(4), 235–240. https://doi.org/10.2113/gselements.6.4.235

Durant, A. J., & Brown, R. J. (2016, January 1). Chapter 3 - Ash Aggregation in Volcanic Clouds. In S. Mackie, K. Cashman, H. Ricketts, A. Rust, & M. Watson (Eds.), *Volcanic ash* (pp. 53–65). Elsevier. https://doi.org/10.1016/B978-0-08-100405-0.00006-9

Dürig, T., Gudmundsson, M. T., Dioguardi, F., Woodhouse, M., Björnsson, H., Barsotti, S., Witt, T., & Walter, T. R. (2018). REFIR- A multi-parameter system for near real-time estimates of plume-height and mass eruption rate during explosive eruptions. *Journal of Volcanology and Geothermal Research*, *360*, 61–83. https://doi.org/10.1016/j.jvolgeores.2018.07.003

Engwell, S. L., de'Michieli Vitturi, M., Esposti Ongaro, T., & Neri, A. (2016). Insights into the formation and dynamics of coignimbrite plumes from one-dimensional models. *Journal of Geophysical Research: Solid Earth*, *121*(6), 4211–4231. https://doi.org/10.1002/2016JB012793

Engwell, S. L., & Eychenne, J. (2016). Chapter 4 - Contribution of Fine Ash to the Atmosphere From Plumes Associated With Pyroclastic Density Currents. In S. Mackie, K. Cashman, H. Ricketts, A. Rust, & M. Watson (Eds.), *Volcanic ash* (pp. 67–85). Elsevier. https://doi.org/10.1016/B978-0-08-100405-0.00007-0

Engwell, S. L., Mastin, L., Tupper, A., Kibler, J., Acethorp, P., Lord, G., & Filgueira, R. (2021). Near-real-time volcanic cloud monitoring: insights into global explosive volcanic eruptive activity through analysis of Volcanic Ash Advisories. *Bulletin of Volcanology*, *83*(2), 9. https://doi.org/10.1007/s00445-020-01419-y

Ernst, G. G. J., Sparks, R. S. J., Carey, S. N., & Bursik, M. I. (1996). Sedimentation from turbulent jets and plumes. *Journal of Geophysical Research: Solid Earth*, *101*, 5575–5589. https://doi.org/10.1029/95JB01900

Etyemezian, V., Gillies, J. A., Mastin, L. G., Crawford, A., Hasson, R., Van Eaton, A. R., & Nikolich, G. (2019). Laboratory Experiments of Volcanic Ash Resuspension by Wind. *Journal of Geophysical Research: Atmospheres*, *124*(16), 9534–9560. https://doi.org/10.1029/2018JD030076

Eychenne, J., Cashman, K., Rust, A., & Durant, A. (2015). Impact of the lateral blast on the spatial pattern and grain size characteristics of the 18 May 1980 Mount St. Helens fallout deposit. *Journal of Geophysical Research: Solid Earth*, *120*(9), 6018–6038. https://doi.org/10.1002/2015JB012116

Eychenne, J., & Engwell, S. L. (2022). The grainsize of volcanic fall deposits: Spatial trends and physical controls. *GSA Bulletin*, *135*(7), 1844–1858. https://doi.org/10.1130/B36275.1

Eychenne, J., Le Pennec, J.-L., Troncoso, L., Gouhier, M., & Nedelec, J.-M. (2012). Causes and consequences of bimodal grain-size distribution of tephra fall deposited during the August 2006 Tungurahua eruption (Ecuador). *Bulletin of Volcanology*, *74*(1), 187–205. https://doi.org/10.1007/s00445-011-0517-5

Fichter, C., Marquart, S., Sausen, R., & Lee, D. S. (2005). The impact of cruise altitude on contrails and related radiative forcing. *Meteorologische Zeitschrift*, *14*(4), 563–572. https://doi.org/10.1127/0941-2948/2005/0048

Fisher, R. V., Glicken, H. X., & Hoblitt, R. P. (1987). May 18, 1980, Mount St. Helens deposits in South Coldwater Creek, Washington. *Journal of Geophysical Research: Solid Earth*, *92*, 10267–10283. https://doi.org/10.1029/JB092iB10p10267

Folch, A., Costa, A., & Basart, S. (2012). Validation of the FALL3D ash dispersion model using observations of the 2010 Eyjafjallajökull volcanic ash clouds. *Atmospheric Environment*, *48*, 165–183. https://doi.org/10.1016/j.atmosenv.2011.06.072

Giordano, G., & Cas, R. A. F. (2021). Classification of ignimbrites and their eruptions. *Earth-Science Reviews*, *220*, 103697. https://doi.org/10.1016/j.earscirev.2021.103697

Global Volcanism Program. (2024). Volcanoes of the World. https://doi.org/10.5479/si.GVP.VOTW5-2024.5.2

Goblet, V., Fala, N., & Marais, K. (2015). Identifying Phases of Flight in General Aviation Operations. *15th AIAA Aviation Technology, Integration, and Operations Conference*. https://doi.org/10.2514/6.2015-2851

Grindle, T. J., & Burcham, F. W. (2003). *Engine Damage to a NASA DC-8-72 Airplane from a High-altitude Encounter with a Diffuse Volcanic Ash Cloud* (NASA/TM-2003-212030). NASA. https://ntrs.nasa.gov/api/citations/20030068344/downloads/20030068344.pdf

Guffanti, M., Casadevall, T., & Budding, K. (2011). Encounters of aircraft with volcanic ash clouds: A compilation of known incidents, 1953-2009. *U.S. Geol. Surv. Data Ser.*, *545*.

Hadley, D., Hufford, G. L., & Simpson, J. J. (2004). Resuspension of Relic Volcanic Ash and Dust from Katmai: Still an Aviation Hazard. *Weather and Forecasting*, *19*(5), 829–840. https://doi.org/10.1175/1520-0434(2004)019<0829:RORVAA>2.0.CO;2

Harrison, S. R., Pope, J. O., Neal, R. A., Garry, F. K., Kurashina, R., & Suri, D. (2022). Identifying Weather Patterns Associated with Increased Volcanic Ash Risk within

British Isles Airspace. *Weather and Forecasting*, *37*(7), 1157–1168. https://doi.org/10.1175/WAF-D-22-0023.1

Harvey, N. J., Huntley, N., Dacre, H. F., Goldstein, M., Thomson, D., & Webster, H. (2018). Multi-level emulation of a volcanic ash transport and dispersion model to quantify sensitivity to uncertain parameters. *Natural Hazards and Earth System Sciences*, *18*(1), 41–63. https://doi.org/10.5194/nhess-18-41-2018

Herzog, M., & Graf, H.-F. (2010). Applying the three-dimensional model ATHAM to volcanic plumes: Dynamic of large co-ignimbrite eruptions and associated injection heights for volcanic gases. *Geophysical Research Letters*, *37*(19), L19807. https://doi.org/10.1029/2010GL044986

Holasek, R. E., & Self, S. (1995). GOES weather satellite observations and measurements of the May 18, 1980, Mount St. Helens eruption. *Journal of Geophysical Research: Solid Earth*, *100*, 8469–8487. https://doi.org/10.1029/94JB03137

ICAO. (1956). *Terrain clearance and vertical separation of aircraft (altimeter setting)* (Circular 26-AN/23). International civil aviation organization. Montreal, Canada.

ICAO. (1993). *MANUAL OF THE ICAO STANDARD ATMOSPHERE extended to 80 kilometers (262 500 feet)* (Doc 7488/3, 3rd edition). International civil aviation organization. https://news.ncac.mn/uploads/bookSubject/2022-11/6369ec174ab34.pdf

ICAO. (2012). *FOURTH MEETING OF THE INTERNATIONAL VOLCANIC ASH TASK FORCE (IVATF/4)*. International civil aviation organization. Montréal, Canada. http://www.icao.int/safety/%20meteorology/ivatf/Meeting%20MetaData/IVATF-4.Final%20Report.%20pdf

ICAO Meteorology panel. (2023). *Quantitative Volcanic Ash (QVA) Concentration Information*. International civil aviation organization. Retrieved July 31, 2025, from https://www.aviation.govt.nz/assets/licensing-and-certification/meteorology/QVA_information_flyer_vs_First-edition.pdf

Jones, A., Thomson, D., Hort, M., & Devenish, B. (2007). The U.K. Met Office's Next-Generation Atmospheric Dispersion Model, NAME III. In C. Borrego & A.-L. Norman (Eds.), *Air pollution modeling and its application XVII* (pp. 580–589). Springer US.

Jones, T. J., Beckett, F., Bernard, B., Breard, E. C. P., Dioguardi, F., Dufek, J., Engwell, S., & Eychenne, J. (2023). Physical properties of pyroclastic density currents: Relevance, challenges and future directions. *Frontiers in Earth Science*, *11*. https://doi.org/10.3389/feart.2023.1218645

Jones, T. J., Shetty, A., Chalk, C., Dufek, J., & Gonnermann, H. M. (2024). Identifying rheological regimes within pyroclastic density currents. *Nature Communications*, *15*(1), 4401. https://doi.org/10.1038/s41467-024-48612-7

Kueppers, U., Cimarelli, C., Hess, K.-U., Taddeucci, J., Wadsworth, F. B., & Dingwell, D. B. (2014). The thermal stability of Eyjafjallajökull ash versus turbine ingestion test sands. *Journal of Applied Volcanology*, *3*(1), 4. https://doi.org/10.1186/2191-5040-3-4

Lacasse, C., Karlsdóttir, S., Larsen, G., Soosalu, H., Rose, W. I., & Ernst, G. G. J. (2004). Weather radar observations of the Hekla 2000 eruption cloud, Iceland. *Bulletin of Volcanology*, *66*(5), 457–473. https://doi.org/10.1007/s00445-003-0329-3

Leadbetter, S. J., Hort, M. C., von Löwis, S., Weber, K., & Witham, C. S. (2012). Modeling the resuspension of ash deposited during the eruption of Eyjafjallajökull in spring 2010. *Journal of Geophysical Research: Atmospheres*, *117*. https://doi.org/10.1029/2011JD016802

Lean, H. W., & Clark, P. A. (2003). The effects of changing resolution on mesocale modelling of line convection and slantwise circulations in FASTEX IOP16. *Quarterly Journal of the Royal Meteorological Society*, *129*(592), 2255–2278. https://doi.org/10.1256/qj.02.57

Lechner, P., Tupper, A., Guffanti, M., Loughlin, S., & Casadevall, T. (2018). Volcanic Ash and Aviation—The Challenges of Real-Time, Global Communication of a Natural Hazard. In C. J. Fearnley, D. K. Bird, K. Haynes, W. J. McGuire, & G. Jolly (Eds.), *Observing the volcano world: Volcano crisis communication* (pp. 51–64). Springer International Publishing. https://doi.org/10.1007/11157_2016_49

Liu, E. J., Cashman, K. V., Beckett, F. M., Witham, C. S., Leadbetter, S. J., Hort, M. C., & Guðmundsson, S. (2014). Ash mists and brown snow: Remobilization of volcanic ash from recent Icelandic eruptions. *Journal of Geophysical Research: Atmospheres*, *119*(15), 9463–9480. https://doi.org/10.1002/2014JD021598

Lube, G., Breard, E. C. P., Esposti-Ongaro, T., Dufek, J., & Brand, B. (2020). Multiphase flow behaviour and hazard prediction of pyroclastic density currents. *Nature Reviews Earth & Environment*, *1*(7), 348–365. https://doi.org/10.1038/s43017-020-0064-8

Marti, A., Folch, A., Costa, A., & Engwell, S. L. (2016). Reconstructing the plinian and co-ignimbrite sources of large volcanic eruptions: A novel approach for the Campanian Ignimbrite. *Scientific Reports*, *6*(1), 21220. https://doi.org/10.1038/srep21220

Mastin, L. G., Carey, S. N., Van Eaton, A. R., Eychenne, J., & Sparks, R. S. J. (2022). Understanding and modeling tephra transport: lessons learned from the 18 May 1980 eruption of Mount St. Helens. *Bulletin of Volcanology*, *85*(1), 4. https://doi.org/10.1007/s00445-022-01613-0

Mastin, L. G., Guffanti, M., Servranckx, R., Webley, P., Barsotti, S., Dean, K., Durant, A., Ewert, J., Neri, A., Rose, W., Schneider, D., Siebert, L., Stunder, B., Swanson, G., Tupper, A., Volentik, A., & Waythomas, C. (2009). A multidisciplinary effort to assign realistic source parameters to models of volcanic ash-cloud transport and dispersion during eruptions. *Journal of Volcanology and Geothermal Research*, *186*(1), 10–21. https://doi.org/10.1016/j.jvolgeores.2009.01.008

Mastin, L. G., Pavolonis, M., Engwell, S. L., Clarkson, R., Witham, C., Brock, G., Lisk, I., Guffanti, M., Tupper, A., Schneider, D., Beckett, F., Casadevall, T., & Rennie, G. (2022). Progress in protecting air travel from volcanic ash clouds. *Bulletin of Volcanology*, *84*(1), 9. https://doi.org/10.1007/s00445-021-01511-x

Mastin, L. G., & Van Eaton, A. R. (2020). Comparing Simulations of Umbrella-Cloud Growth and Ash Transport with Observations from Pinatubo, Kelud, and Calbuco Volcanoes. *Atmosphere*, *11*(10), 1038. https://doi.org/10.3390/atmos11101038

McLean, D., Horn, E. L., Aguiar, S., Barton, N., Brown, R., Carolin, S., Day, C., Kuhlmann, H., Kutterolf, S., Mitsunaga, B., O'Mara, N. A., Pacheco, J. M., Pimentel, A., Ramalho, R. S., Schindlbeck-Belo, J. C., Stoetzel, E., Styring, A., Uno, K. T., Vidyarthi, V., … Smith, V. C. (2024). Opportunities to synchronise and date archaeological and climate records in Northwest Africa using volcanic ash (tephra) layers. *Libyan Studies*, *55*, 48–68. https://doi.org/10.1017/lis.2024.18

Meteorological Office. (1991). *Meteorological glossary* (R. P. W. Lewis, Ed.; 6. ed). H.M.S.O.

Michol, K. A., Russell, J. K., & Andrews, G. D. M. (2008). Welded block and ash flow deposits from Mount Meager, British Columbia, Canada. *Journal of Volcanology and Geothermal Research*, *169*(3), 121–144. https://doi.org/10.1016/j.jvolgeores.2007.08.010

Middleton, N. J., & Goudie, A. S. (2001). Saharan dust: Sources and trajectories. *Transactions of the Institute of British Geographers*, *26*(2), 165–181. https://doi.org/10.1111/1475-5661.00013

Miller, T. P., & Casadevall, T. J. (1999). Volcanic Ash Hazards to Aviation. In H. Sigurdsson, B. Houghton, H. Rymer, J. Stix, & S. McNutt (Eds.), *Encyclopedia of volcanoes* (1st ed., pp. 915–930). Elsevier Science & Technology.

Mirza, A. K., Dacre, H. F., & Lo, C. H. B. (2024). A case study analysis of the impact of a new free tropospheric turbulence scheme on the dispersion of an atmospheric tracer. *Quarterly Journal of the Royal Meteorological Society*, *150*(761), 1907–1925. https://doi.org/10.1002/qj.4681

Morton, B. R., Taylor, G. I., & Turner, J. S. (1956). Turbulent gravitational convection from maintained and instantaneous sources. *Proceedings of the Royal Society of*

London. Series A. Mathematical and Physical Sciences, *234*(1196), 1–23. https://doi.org/10.1098/rspa.1956.0011

Neal, R., Fereday, D., Crocker, R., & Comer, R. E. (2016). A flexible approach to defining weather patterns and their application in weather forecasting over Europe. *Meteorological Applications*, *23*(3), 389–400. https://doi.org/10.1002/met.1563

Neri, A., Di Muro, A., & Rosi, M. (2002). Mass partition during collapsing and transitional columns by using numerical simulations. *Journal of Volcanology and Geothermal Research*, *115*(1), 1–18. https://doi.org/10.1016/S0377-0273(01)00304-3

Neri, A., Esposti Ongaro, T., Macedonio, G., & Gidaspow, D. (2003). Multiparticle simulation of collapsing volcanic columns and pyroclastic flow. *Journal of Geophysical Research: Solid Earth*, *108*, 2202. https://doi.org/10.1029/2001JB000508

Newhall, C. G., & Self, S. (1982). The volcanic explosivity index (VEI) an estimate of explosive magnitude for historical volcanism. *Journal of Geophysical Research: Oceans*, *87*, 1231–1238. https://doi.org/10.1029/JC087iC02p01231

Oberhuber, J. M., Herzog, M., Graf, H.-F., & Schwanke, K. (1998). Volcanic plume simulation on large scales. *Journal of Volcanology and Geothermal Research*, *87*(1), 29–53. https://doi.org/10.1016/S0377-0273(98)00099-7

Pardini, F., Barsotti, S., Bonadonna, C., de'Michieli Vitturi, M., Folch, A., Mastin, L., Osores, S., & Prata, A. T. (2024). Dynamics, Monitoring, and Forecasting of Tephra in the Atmosphere. *Reviews of Geophysics*, *62*(4), e2023RG000808. https://doi.org/10.1029/2023RG000808

Pioli, L., Bonadonna, C., & Pistolesi, M. (2019). Reliability of Total Grain-Size Distribution of Tephra Deposits. *Scientific Reports*, *9*(1), 10006. https://doi.org/10.1038/s41598-019-46125-8

Pioli, L., & Harris, A. J. L. (2019). Real-Time Geophysical Monitoring of Particle Size Distribution During Volcanic Explosions at Stromboli Volcano (Italy). *Frontiers in Earth Science*, *7*. https://doi.org/10.3389/feart.2019.00052

Pistolesi, M., Albert, P. G., Ponce, A. A., Engwell, S., Kueppers, U., Pardini, F., Tsunematsu, K., & Eaton, A. R. V. (2025). Tephra fallout and associated deposits. Retrieved September 9, 2025, from https://eartharxiv.org/repository/view/9680/

Prata, A. J. (2009). Satellite detection of hazardous volcanic clouds and the risk to global air traffic. *Natural Hazards*, *51*(2), 303–324. https://doi.org/10.1007/s11069-008-9273-z

Prata, A. J., & Prata, A. T. (2012). Eyjafjallajökull volcanic ash concentrations determined using Spin Enhanced Visible and Infrared Imager measurements. *Journal of Geophysical Research: Atmospheres*, *117*. https://doi.org/10.1029/2011JD016800

Prata, F., Prata, A. T., Tanner, R., Grainger, R. G., Borgas, M., & Aubry, T. J. (2025). The radial spreading of volcanic umbrella clouds deduced from satellite measurements. *Volcanica*, *8*(1), 1–29. https://doi.org/10.30909/vol.08.01.0129

Prata, F., & Rose, B. (2015). Chapter 52 - Volcanic Ash Hazards to Aviation. In H. Sigurdsson (Ed.), *The encyclopedia of volcanoes (second edition)* (pp. 911–934). Academic Press. https://doi.org/10.1016/B978-0-12-385938-9.00052-3

Rolph, G. D., Ngan, F., & Draxler, R. R. (2014). Modeling the fallout from stabilized nuclear clouds using the HYSPLIT atmospheric dispersion model. *Journal of Environmental Radioactivity*, *136*, 41–55. https://doi.org/10.1016/j.jenvrad.2014.05.006

Rose, W. I., Bluth, G. J. S., & Ernst, G. G. J. (2000). Integrating retrievals of volcanic cloud characteristics from satellite remote sensors: A summary (P. Francis, J. Neuberg, & R. S. J. Sparks, Eds.). *Philosophical Transactions of the Royal Society of London. Series A: Mathematical, Physical and Engineering Sciences*, *358*(1770), 1585–1606. https://doi.org/10.1098/rsta.2000.0605

Rosi, M., Bertagnini, A., Harris, A. J. L., Pioli, L., Pistolesi, M., & Ripepe, M. (2006). A case history of paroxysmal explosion at Stromboli: Timing and dynamics of the April 5, 2003 event. *Earth and Planetary Science Letters*, *243*(3), 594–606. https://doi.org/10.1016/j.epsl.2006.01.035

Saint, C., Beckett, F. M., Dioguardi, F., Kristiansen, N., & Tubbs, R. N. (2024). Using Simulated Radiances to Understand the Limitations of Satellite-Retrieved Volcanic Ash Data and the Implications for Volcanic Ash Cloud Forecasting. *Journal of Geophysical Research: Atmospheres*, *129*(23), e2024JD041112. https://doi.org/10.1029/2024JD041112

Saxby, J., Beckett, F., Cashman, K., Rust, A., & Tennant, E. (2018). The impact of particle shape on fall velocity: Implications for volcanic ash dispersion modelling. *Journal of Volcanology and Geothermal Research*, *362*, 32–48. https://doi.org/10.1016/j.jvolgeores.2018.08.006

Scollo, S., Prestifilippo, M., Pecora, E., Corradini, S., Merucci, L., Spata, G., & Coltelli, M. (2014). Eruption column height estimation of the 2011-2013 Etna lava fountains. *Annals of Geophysics*, *57*(2), S0214. https://doi.org/10.4401/ag-6396

Sigurdsson, H., & Carey, S. N. (1989). Plinian and co-ignimbrite tephra fall from the 1815 eruption of Tambora volcano. *Bulletin of Volcanology*, *51*(4), 243–270. https://doi.org/10.1007/BF01073515

Simionato, R., Jarvis, P. A., Rossi, E., Fries, A., Pistolesi, M., Aguilar, R., & Bonadonna, C. (2024). Combining Visible- and Infrared-Wavelength Observations With Numerical Modeling to Describe Vulcanian Eruption Plumes at Sabancaya, Peru. *Journal of*

Geophysical Research: Solid Earth, *129*(12), e2024JB029326. https://doi.org/10.1029/2024JB029326

Simpson, J. J., Berg, J. S., Hufford, G. L., Bauer, C., Pieri, D., & Servranckx, R. (2002). The February 2001 Eruption of Mount Cleveland, Alaska: Case Study of an Aviation Hazard. *Weather and Forecasting*, *17*(4), 691–704. https://doi.org/10.1175/1520-0434(2002)017<0691:TFEOMC>2.0.CO;2

Sparks, R. S. J. (1986). The dimensions and dynamics of volcanic eruption columns. *Bulletin of Volcanology*, *48*(1), 3–15. https://doi.org/10.1007/BF01073509

Sparks, R. S. J., Bursik, M. I., Carey, S. N., Gilbert, J. S., Glaze, L. S., Sigurdsson, H., & Woods, A. W. (1997). *Volcanic plumes*. Wiley.

Sparks, R. S. J., Moore, J. G., & Rice, C. J. (1986). The initial giant umbrella cloud of the May 18th, 1980, explosive eruption of Mount St. Helens. *Journal of Volcanology and Geothermal Research*, *28*(3), 257–274. https://doi.org/10.1016/0377-0273(86)90026-0

Sulpizio, R., Capra, L., Sarocchi, D., Saucedo, R., Gavilanes-Ruiz, J. C., & Varley, N. R. (2010). Predicting the block-and-ash flow inundation areas at Volcán de Colima (Colima, Mexico) based on the present day (February 2010) status. *Journal of Volcanology and Geothermal Research*, *193*(1), 49–66. https://doi.org/10.1016/j.jvolgeores.2010.03.007

Thorsteinsson, T., Jóhannsson, T., Stohl, A., & Kristiansen, N. I. (2012). High levels of particulate matter in Iceland due to direct ash emissions by the Eyjafjallajökull eruption and resuspension of deposited ash. *Journal of Geophysical Research: Solid Earth*, *117, B00C05*. https://doi.org/10.1029/2011JB008756

Tupper, A., Textor, C., Herzog, M., Graf, H.-F., & Richards, M. S. (2009). Tall clouds from small eruptions: The sensitivity of eruption height and fine ash content to tropospheric instability. *Natural Hazards*, *51*(2), 375–401. https://doi.org/10.1007/s11069-009-9433-9

Ui, T., Matsuwo, N., Sumita, M., & Fujinawa, A. (1999). Generation of block and ash flows during the 1990–1995 eruption of Unzen Volcano, Japan. *Journal of Volcanology and Geothermal Research*, *89*(1), 123–137. https://doi.org/10.1016/S0377-0273(98)00128-0

Van Eaton, A. R., Amigo, Á., Bertin, D., Mastin, L. G., Giacosa, R. E., González, J., Valderrama, O., Fontijn, K., & Behnke, S. A. (2016). Volcanic lightning and plume behavior reveal evolving hazards during the April 2015 eruption of Calbuco volcano, Chile. *Geophysical Research Letters*, *43*(7), 3563–3571. https://doi.org/10.1002/2016GL068076

Vukmirović, Z., Unkašević, M., Lazić, L., Tošić, I., Rajsic, S., & Tasic, M. (2004). Analysis of the Saharan dust regional transport. *Meteorology and Atmospheric Physics*, *85*, 265–273. https://doi.org/10.1007/s00703-003-0010-6

Walters, D., Baran, A. J., Boutle, I., Brooks, M., Earnshaw, P., Edwards, J., Furtado, K., Hill, P., Lock, A., Manners, J., Morcrette, C., Mulcahy, J., Sanchez, C., Smith, C., Stratton, R., Tennant, W., Tomassini, L., Van Weverberg, K., Vosper, S., … Zerroukat, M. (2019). The Met Office Unified Model Global Atmosphere 7.0/7.1 and JULES Global Land 7.0 configurations. *Geoscientific Model Development*, *12*(5), 1909–1963. https://doi.org/10.5194/gmd-12-1909-2019

Warner, S., Platt, N., & Heagy, J. F. (2004). User-Oriented Two-Dimensional Measure of Effectiveness for the Evaluation of Transport and Dispersion Models. *Journal of Applied Meteorology*, *43*(1), 58–73. https://doi.org/10.1175/1520-0450(2004)043<0058:UTMOEF>2.0.CO;2

Watanabe, K., Ono, K., Sakaguchi, K., Takada, A., & Hoshizumi, H. (1999). Co-ignimbrite ash-fall deposits of the 1991 eruptions of Fugen-dake, Unzen Volcano, Japan. *Journal of Volcanology and Geothermal Research*, *89*(1), 95–112. https://doi.org/10.1016/S0377-0273(98)00126-7

Webster, H. N., Devenish, B. J., Mastin, L. G., Thomson, D. J., & Van Eaton, A. R. (2020). Operational Modelling of Umbrella Cloud Growth in a Lagrangian Volcanic Ash Transport and Dispersion Model. *Atmosphere*, *11*(2), 200. https://doi.org/10.3390/atmos11020200

Webster, H. N., Thomson, D. J., Johnson, B. T., Heard, I. P. C., Turnbull, K., Marenco, F., Kristiansen, N. I., Dorsey, J., Minikin, A., Weinzierl, B., Schumann, U., Sparks, R. S. J., Loughlin, S. C., Hort, M. C., Leadbetter, S. J., Devenish, B. J., Manning, A. J., Witham, C. S., Haywood, J. M., & Golding, B. W. (2012). Operational prediction of ash concentrations in the distal volcanic cloud from the 2010 Eyjafjallajökull eruption. *Journal of Geophysical Research: Atmospheres*, *117*. https://doi.org/10.1029/2011JD016790

Webster, H. N., Whitehead, T., & Thomson, D. J. (2018). Parameterizing Unresolved Mesoscale Motions in Atmospheric Dispersion Models. *Journal of Applied Meteorology and Climatology*, *57*(3), 645–657. https://doi.org/10.1175/JAMC-D-17-0075.1

Webster, H., & Thomson, D. (2011). Dry deposition modelling in a Lagrangian dispersion model. *International Journal of Environment and Pollution*, *47*(1), 1. https://doi.org/10.1504/IJEP.2011.047322

Wiegner, M., Gasteiger, J., Groß, S., Schnell, F., Freudenthaler, V., & Forkel, R. (2012). Characterization of the Eyjafjallajökull ash-plume: Potential of lidar remote sensing.

Physics and Chemistry of the Earth, Parts A/B/C, *45-46*, 79–86. https://doi.org/10.1016/j.pce.2011.01.006

Wilson, L., Sparks, R. S. J., Huang, T. C., & Watkins, N. D. (1978). The control of volcanic column heights by eruption energetics and dynamics. *Journal of Geophysical Research: Solid Earth*, *83*, 1829–1836. https://doi.org/10.1029/JB083iB04p01829

Wilson, T. M., Jenkins, S., & Stewart, C. (2015). Chapter 3 - Impacts from Volcanic Ash Fall. In J. F. Shroder & P. Papale (Eds.), *Volcanic hazards, risks and disasters* (pp. 47–86). Elsevier. https://doi.org/10.1016/B978-0-12-396453-3.00003-4

Witham, C., Webster, H., Hort, M., Jones, A., & Thomson, D. (2012). Modelling concentrations of volcanic ash encountered by aircraft in past eruptions. *Atmospheric Environment*, *48*, 219–229. https://doi.org/10.1016/j.atmosenv.2011.06.073

Woods, A. W., & Kienle, J. (1994). The dynamics and thermodynamics of volcanic clouds: Theory and observations from the april 15 and april 21, 1990 eruptions of redoubt volcano, Alaska. *Journal of Volcanology and Geothermal Research*, *62*(1), 273–299. https://doi.org/10.1016/0377-0273(94)90037-X

Woods, A. W., & Wohletz, K. (1991). Dimensions and dynamics of co-ignimbrite eruption columns. *Nature*, *350*(6315), 225–227. https://doi.org/10.1038/350225a0

Zidikheri, M. J., Lucas, C., & Potts, R. J. (2017). Estimation of optimal dispersion model source parameters using satellite detections of volcanic ash. *Journal of Geophysical Research: Atmospheres*, *122*(15), 8207–8232. https://doi.org/10.1002/2017JD026676